Remote Sensing of Environment 338 (2026) 115320

Contents lists available at ScienceDirect

Remote Sensing of Environment

journal homepage: www.elsevier.com/locate/rse

Deformation, strains and velocities for the Alpine Himalayan Belt from trans-continental Sentinel-1 InSAR & GNSS

J.R. Elliott[a,*], J. Fang[a,*], M. Lazecký[a], Y. Maghsoudi[b], Q. Ou[c], J.A. Payne[a], C. Rollins[d], D. Wang[a], A. Hooper[a], T. J. Wright[a]

[a] COMET, School of Earth & Environment, University of Leeds, Woodhouse Lane, Leeds, LS2 9JT, West Yorkshire, UK
[b] Centre for Environmental Mathematics, University of Exeter, Penryn Campus, Nr Falmouth, TR10 9FE, Cornwall, UK
[c] School of GeoSciences, University of Edinburgh, Drummond Street, Edinburgh, EH8 9XP, West Lothian, UK
[d] Earthquake Physics and Statistics, GNS Science, 1 Fairway Drive, Avalon, 5011, Lower Hutt, New Zealand

HIGHLIGHTS

- First 3D velocity field of Alpine-Himalayan Belt derived from Sentinel-1 InSAR & GNSS.
- Strain localised on major faults with diffuse deformation extensive across continents.
- Horizontal motion is dominated by tectonics; vertical from aquifer-driven subsidence.

GRAPHICAL ABSTRACT

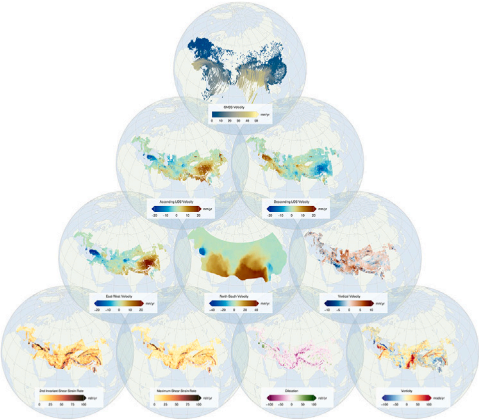

ARTICLE INFO

Edited by Dr Jing M. Chen

Keywords:
Radar remote sensing
GNSS
Sentinel-1
InSAR
Active tectonics
Continental deformation
Faulting
Strain
Seismic hazard
Earthquakes

ABSTRACT

Surface velocities and strain rates from satellite geodesy have become essential tools for understanding the distribution of tectonic deformation, faulting and seismic hazard. However, across large regions of distributed continental deformation, such as the Alpine-Himalayan Belt, data are only sparsely available. While previous studies have mainly used spatially sparse GNSS to measure deformation at such large scales, these approaches cannot characterize shorter wavelength features of deformation in many places. We use Sentinel-1 radar images acquired during 2016–2024 to provide trans-national average surface velocities and time series at 1 km spatial resolution stretching a distance of over 11,000 km from south-western Europe to eastern China, covering an area more than 20 million square kilometres. We produce the velocity field by combining data from over 222,000 Sentinel-1 SAR images with a new belt-wide compilation of GNSS velocities, all combined in a consistent Eurasian reference frame. Horizontal strain rates are derived from gradients of the velocity field, yielding near-continuous spatial deformation information over the entirety of the largest deforming region on the planet. The horizontal velocities and strains are dominated by tectonic deformation, which has a bimodal behaviour – focused on major faults but distributed elsewhere. Shorter-wavelength vertical velocities are dominated by non-tectonic processes, in particular the widespread over-exploitation of groundwater. Our new velocity and strain rates are foundational data sets that reveal the details of how the continents deform for the first time at trans-continental scale.

---

* Corresponding authors.
Email addresses: j.elliott@leeds.ac.uk (J.R. Elliott), j.fang@leeds.ac.uk (J. Fang).

https://doi.org/10.1016/j.rse.2026.115320
Received 27 May 2025; Received in revised form 15 December 2025; Accepted 14 February 2026

Available online 5 March 2026
0034-4257/© 2026 The Authors. Published by Elsevier Inc. This is an open access article under the CC BY-NC license (http://creativecommons.org/licenses/by-nc/4.0/).

1. Introduction

The collision of the African, Arabian, and Indian plates with Eurasia has created the Alpine Himalayan Belt (AHB), a vast region of thickened crust and mountain ranges spanning the southern margin of the Eurasian continent (Fig. 1) and reaching ~2000 km into its interior in places. This major orogeny creates, supports and shapes the highest mountains in the world and has been a long-standing focus of research on the deformation of the continents (Molnar and Tapponnier, 1978; England and Jackson, 1989). The region is marked by numerous active seismogenic faults (Styron and Pagani, 2020), generating some of the largest, and often most fatal, earthquakes (Bilham, 2019) – 75 % of earthquakes that have killed more than 10,000 people since 1900 have occurred here (England and Jackson, 2011). Understanding the kinematics of this range is important for constraining the style of tectonics of the continents (Jackson and McKenzie, 1984; Yin, 2010), which in turn act as first-order constraints on dynamical models of deformation (England and Molnar, 1997; Vergnolle et al., 2007) and how the continents and margins might evolve through time (McKenzie, 2025). Increasingly, deformation data are important inputs for seismic hazard assessments, providing independent constraints on slip rates of major faults and spatial maps of moment accumulation rates (Bird et al., 2015; Field et al., 2015; Stevens and Avouac, 2021).

The recent explosion in the availability of remotely-sensed data from satellite platforms, particularly in this past decade by the European Space Agency's Sentinel-1 radar mission (Salvi et al., 2012; Potin et al., 2016), has enabled a step change in the scale of Interferometric Synthetic Aperture Radar (InSAR) measurements of surface deformation (Gabriel et al., 1989). The open Sentinel-1 archive and advances in big data processing (e.g., Lazecký et al., 2020) have enabled us to produce the first transcontinental, decadal time series of surface velocities at a resolution of 1 km. This allows us to resolve details of tectonic processes at scale. From the Sentinel-1 data, and our new compilation of Global Navigation Satellite System (GNSS) data, we derive three-component average surface velocities in a consistent Eurasian reference frame, and estimates of horizontal surface strain rates. The results show the contrast in tectonic deformation between regions of high strain localisation and those with more distributed deformation, as well as highlighting non-tectonic processes, particularly those associated with exploitation of groundwater. We make these new time series, velocities and strain rates freely available in an open repository for further analysis and modelling by the wider community.

1.1. Motivation: understanding the deformation of the continents

Understanding present-day deformation of the continents is important for assessing the distribution of seismic hazard through the calculation of strain rates (Ward, 1998; Bird et al., 2010), and for constraining crustal tectonic kinematics to allow testing and assessment of continental deformation dynamics (e.g., Flesch et al., 2001; Wang and Barbot, 2023; Fang et al., 2024a).

It has long been recognised that plate tectonics operates differently in the continents than oceans (McKenzie, 1972; Molnar and Tapponnier, 1975; McKenzie, 2025), but understanding how continents deform has been hampered by the lack of observations with the spatial resolution required to resolve tectonic processes. Understanding where and why contrasting styles of deformation are observed remain key questions in active tectonics (Thatcher, 2007). For example, why does seismicity and strain in some regions appear largely focused on large block-bounding faults such as the North Anatolian Fault (Weiss et al., 2020), similar to the behaviour seen in oceanic lithosphere, whereas other regions appear more diffuse (Watson et al., 2024)? Establishing this is useful for calculating the distribution of hazard (Liu and Stein, 2016), and determining the degree to which continents experience on-fault versus off-fault deformation (Zeng and Shen, 2016). We want to be able to determine the seismic moment accumulation rate as this sets the budget for future earthquakes; geodetic strain-rate observations allow us to estimate this (Guns et al., 2024). At a crustal scale, a long-standing argument has been determining the most parsimonious way of describing the kinematic behaviour of the continental crust in terms of block-like behaviour (Thatcher, 2007), continuum behaviour (Houseman and England, 1986), or a mixture of both (Wang and Barbot, 2023; Fang et al., 2024a,b).

To address these questions, we require the current rates of surface deformation and the degree of localisation of strain, as these provide key inputs for constraining future models and act as secular rates to compare against when exploring time-varying behaviour of crustal deformation. Previous studies made significant progress using sparser GNSS data (Reilinger et al., 2006; Thatcher, 2009; Stamps and Kreemer, 2024), or local and regional InSAR based studies (Elliott et al., 2016). The widespread availability of Sentinel-1 data (Torres et al., 2012) is a timely opportunity to produce an internally referenced and consistent continent-wide InSAR-derived velocity field. This is particularly important for areas that, unlike Europe (Piña-Valdés et al., 2022) and the Western U.S. (Herring et al., 2016), lack (and are unlikely to readily achieve) dense GNSS coverage.

Here we introduce previous regional scale deformation studies, before presenting the two principal datasets of GNSS and InSAR. We describe our compilation of previously-published GNSS velocities and how we align them to create a consistently referenced set of data. We then provide our methodological and systematic approach to generating and correcting the InSAR time series before illustrating how we integrate this with the GNSS constraints to generate velocity and strain rate fields at a transcontinental scale. We show the resulting components of velocity and measures of strain across the Alpine Himalayan Belt as a whole, before focusing on a few key deforming tectonic areas. We discuss the sources of these signals and the limitations of measuring strain in the presence of the remaining noise in our time series. We finish by discussing the potential implications for our broader understanding of continental deformation and the outlook for improvements expected with data from future satellite missions.

2. Background

The AHB has long been recognised as a wide collisional zone (Argand, 1922) and exhibits a range of deformation styles running from west-to-east (Jackson and McKenzie, 1984). There are three major sections of the collisional zone that predominantly align with the three converging plates to the south of Eurasia (Fig. 1) the tectonics of which are discussed further in the Supplementary Information (Section 2).

2.1. Remotely sensed data and technological advances

Our ability to determine the deformation of the continents has been greatly advanced in the past two decades by space-based technologies and data sets (Elliott et al., 2016; Stamps and Kreemer, 2024). Initial progress was made through regional GNSS studies (Feigl et al., 1993; Abdrakhmatov et al., 1996; Reilinger et al., 1997; Wang et al., 2001; Calais et al., 2003; Nocquet and Calais, 2003), before the global strain rate model (GSRM-1) provided horizontal velocities and low-resolution strain rates for most of the deforming plate boundary zones from over 3000 GNSS sites globally (Kreemer et al., 2003). This was advanced in version 2.1 of GSRM (Kreemer et al., 2014) by incorporating over 22,000 velocities in the model. The most recent Europe Velocity model for 2022 (EuVeM2022) is constrained by data from 2549 GNSS sites with an output resolution of 0.1° (Steffen et al., 2025) and covers Europe and Anatolia.

Distributed measurements of surface velocities from InSAR over deforming regions, when suitably referenced with GNSS data, can advance our understanding of continental deformation by increasing the resolution of velocity fields (and the strain rates calculated from them) where GNSS coverage is sparse. There has been a transition from the earliest studies with InSAR on deforming regions which solely focused on single tracks of data less than 100 km in extent (Peltzer et al., 2001;

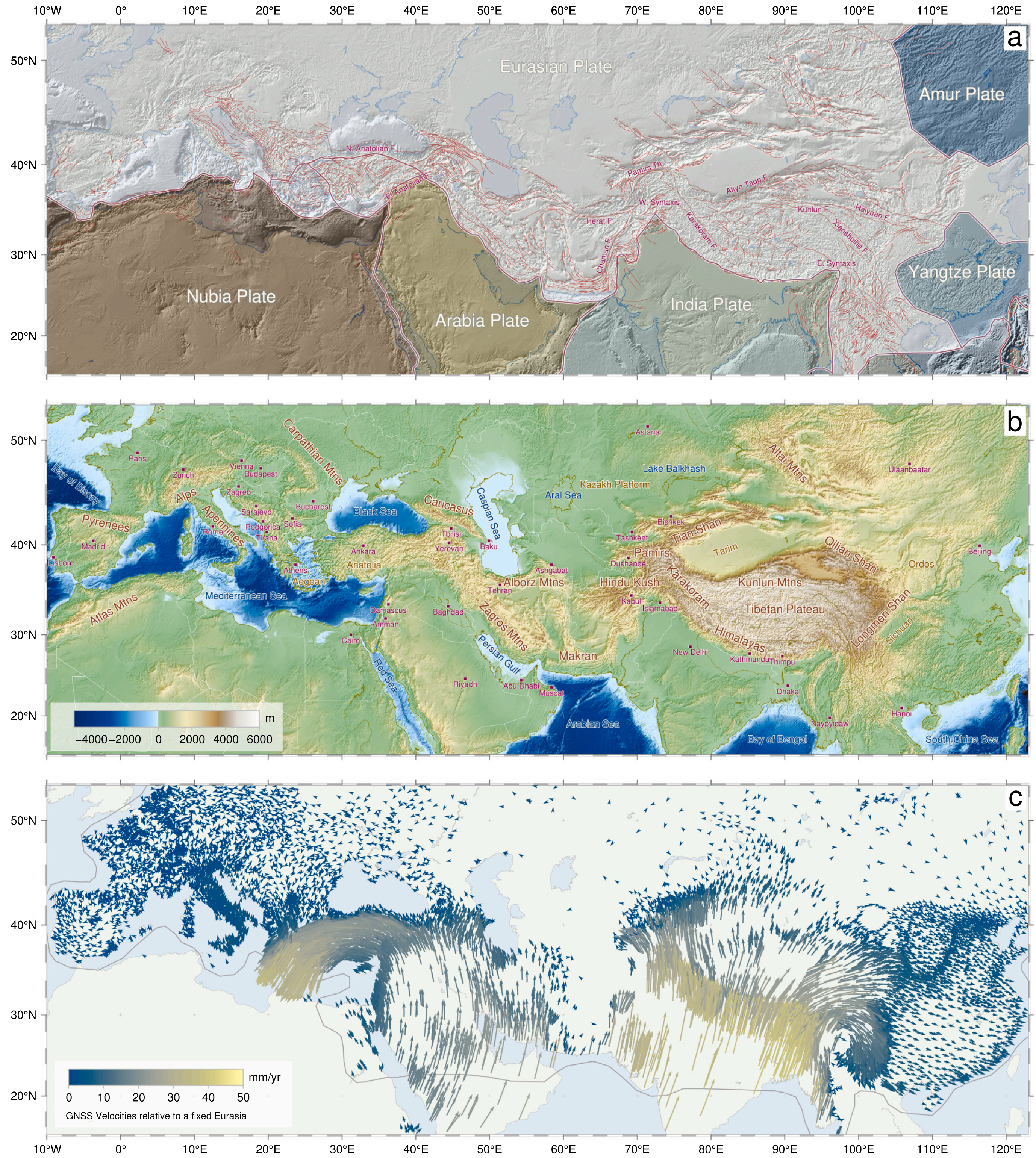

Fig. 1. (a) Major active faults of the Alpine Himalayan orogeny (Styron and Pagani, 2020) with the tectonic plates of the region outlined from Bird (2003) and the major faults (F.) named in the text marked. (b) Topographic map of the belt with major mountain zones marked in brown and capital cities denoted by squares. (c) Compiled and aligned GNSS locations used in this study (Tables SA1–SA2) with velocities shown with respect to a fixed Eurasia reference frame (velocities with respect to the ITRF14 are shown in Figure SB1). The combined InSAR-GNSS velocity field coverage is denoted by the dark grey polygon. (For interpretation of the references to colour in this figure legend, the reader is referred to the web version of this article.)

Wright et al., 2001), largely with ERS-1/2 data (Bürgmann et al., 2000), to entire fault systems (Tong et al., 2013; Hussain et al., 2018) predominately with ENVISAT data, and more recently using Sentinel-1 SAR to capture deformation over large tectonically deforming regions (Xu et al., 2021; Lemrabet et al., 2023; Fang et al., 2024a) and whole country scales (Dehls et al., 2019; Drouin and Sigmundsson, 2019; Weiss et al., 2020; Festa et al., 2022; Zhang et al., 2024), and now large fractions of continents (Costantini et al., 2021).

In addition to technical advancements in SAR instrumentation, typified by the changes from ERS-1/2 (Attema et al., 1998) through ENVISAT-ASAR (Desnos et al., 2000) to Sentinel-1A/B (Torres et al., 2017) enabling more systematic acquisitions and observations suitable for interferometry, there have been improvements in processing SAR (Goldstein and Werner, 1998; Rosen et al., 2012; Sandwell et al., 2011), mitigating atmospheric noise (Lohman and Simons, 2005; Li et al., 2005; Jolivet et al., 2014; Bekaert et al., 2015) and enhancing time series analysis (Hooper et al., 2004; Hetland et al., 2012). This has enabled imaging of ever smaller displacement rate signals (mm/yr) over larger spatial scales of many hundreds of kilometres. Improvements accounting for tropospheric variability in delay using weather models (Jolivet et al., 2011; Murray et al., 2019) and the ionosphere (Liang et al., 2019) using global ionospheric maps, enables smaller signals over longer wavelengths to be increasingly discernible.

Large data volumes have necessitated changes in approach (input data alone is PetaByte scale), with automation of processing of Big Data needed in pipelines on High Performance Computing (HPC), as used here (Lazecký et al., 2020). Various groups have initiatives for covering areas or providing on-demand processing to derive analysis-ready data, enabling wider adoption by the broader community without need for large computing power. ForM@Ter Large-scale multi-Temporal Sentinel-1 InterferoMetry (FLATSIM, Doin et al., 2011) is an initiative providing processed products over broad regions for research. The Alaska SAR Facility (ASF) archives the SLC data from ESA and provides processing capability (Meyer et al., 2025). They also host the Jet Propulsion Laboratory (JPL) geocoded and unwrapped interferograms (Bekaert et al., 2023) and velocities for North America. The European Ground Motion Service is available for (most of) Europe (Costantini et al., 2021) with high-resolution velocities available. The German Aerospace Centre (DLR) has a pipeline for processing all major deforming regions (Gomba et al., 2024). Efforts to make InSAR data easier to use are progressing in the form of Analysis Ready Data (Wang et al., 2022b).

2.2. Challenges and approach taken here

A number of challenges exist in generating continental-scale velocity and strain rate fields given the large spatial scale (tens of millions of square kilometres) and fine sensitivity sought (mm/yr velocities and strain rates of tens of nanostrain per year). The data volumes and their ongoing acquisition, whilst very welcome for science, present constant data handling and processing challenges. Whilst Sentinel-1 SLC (Single Look Complex) data has pixel spacings of ∼4 m in ground range and 14 m in azimuth, it has been necessary to multilook the interferometric images to 50 m and downsample further to 110 m as a compromise to facilitate processing and storage. With the time series analysis and velocity field generation, further downsampling to 1 km has been necessary to make processing tractable.

Stratified layered noise introduced from water vapour and pressure path delay differences in the troposphere between acquisitions can be significantly reduced by applying weather model corrections (Bekaert et al., 2015; Murray et al., 2019). However, this correction is less accurate in regions of steep topography with large gradients in water vapour or in regions with complex and highly convective weather patterns and fronts, as weather reanalysis models do not capture short-wavelength turbulent weather conditions. The assessment of long-wavelength ionospheric corrections is still developing, as the total electron content variability, which advances the phase of the signal, depends on latitude and time of acquisition (Liang et al., 2019). Being C-band, Sentinel-1 is less susceptible to ionospheric phase variability than L-band satellites, but the signal is still significant. The 11-year solar cycle (Hathaway, 2015) has a large impact on the ionosphere (Roma-Dollase et al., 2018); the solar cycle 24 high occurred around the launch of Sentinel-1A in early 2014, and solar activity was therefore decreasing for the early part of our time series (starting early 2016), but it has been increasing and was more elevated than expected by our end date in early 2024.

Whilst shorter wavelength C-band is better in terms of ionospheric noise, it is less effective in terms of phase coherence than L-band, leading to a loss of data coverage in some areas, in particular those that are more vegetated and cultivated, where surface properties change rapidly (Kellndorfer et al., 2022). This affects the AHB most markedly in the west (Europe to Anatolia) and in the south-east (around the Himalayas and Eastern Tibet). This is in part mitigated by the short revisit time of Sentinel-1, which was particularly good when S1A and S1B were both in operation, until the loss of the SAR antenna power supply unit on S1B on 23rd December 2021. Issues of coherence were further compounded when there were large acquisition gaps (sometimes year-long gaps) over certain regions due to limitations of the duty cycle. Additionally, data was not acquired in Eastern China (Figure SB2). High mountain areas with steep relief such as the Caucasus and Himalayas (Grandin et al., 2012) lead to further gaps in data coverage and large phase unwrapping errors due to the loss of connected coherence across our scenes.

Interferometric coherence with Sentinel-1 has been better maintained, when compared to ENVISAT and ERS-1/2, by improved orbital control. The orbital tube originally targeted was ∼ 100 m (Prats-Iraola et al., 2015), keeping it well within the critical baseline for interferometry. However, recent reduced orbital inclination control on S1A, from partial failure of the thruster for out-of-plane manoeuvres in February 2024, has led to increasingly large perpendicular baselines (Pinheiro, 2024) that are likely to have a detrimental impact on interferometric performance and capabilities.

InSAR data, when used alone, is severely hampered by providing a single line-of-sight and only relative deformation (Hu et al., 2014). Even when two look directions are combined, polar-orbiting satellites that look to one side only, are largely insensitive to north–south motion (Wright et al., 2004b). North–south information can be extracted from burst overlap areas of Sentinel-1 (Li et al., 2021a), but the coverage is poor. Due to this lack of 3-component information and the need to reference the InSAR data, we also use GNSS data. There are significant numbers of GNSS sites in Europe and Eastern China, but there is a low density of sites in the centre of the AHB around Afghanistan and Pakistan (Figure SB1). This presents challenges when trying to reference the InSAR data and interpret long-wavelength deformation patterns.

Our aim is to measure surface displacements and calculate velocities that are representative of tectonic processes due to deep-seated deformation sources of stress causing strain over long wavelengths. However, near-surface processes such as land subsidence (Haghshenas Haghighi and Motagh, 2024; Wu et al., 2022) and permafrost (Chen et al., 2022; Fan et al., 2025) mask deeper-seated tectonic strains, in particular in regions where we would want to measure uplift rates reliably, and therefore these areas must be interpreted carefully.

We derive decadal surface velocity fields from which we calculate crustal horizontal strain rates. Our aim is to capture the long-term, interseismic part of the earthquake cycle (Wright, 2002) in these measurements. However, the velocity field is calculated over a finite duration and incorporates the coseismic offsets of recent earthquakes, which we need to remove from our time series as they otherwise manifest as large strains due to the elastic release of strain accumulation. Furthermore, the stress from the earthquakes themselves results in postseismic deformation that can be attributed to a number of causes (Hearn, 2003; Feigl and Thatcher, 2006; Wright et al., 2013) and lasts for many years and potentially decades. Given that the Earth behaves viscoelastically, and faults can slip aseismically, it is not straightforward to attribute interseismic strain accumulation to fault slip potential (Hussain et al., 2018), depending on the rheology of the fault zone and crust (Hilley et al., 2009) and when within the earthquake cycle the deformation is measured (Savage and Prescott, 1978; Wang et al., 2021). A knowledge of historical earthquake locations enables us to test to what degree the elevated strains we are measuring today result from the postseismic deformation of past seismicity.

Sentinel-1 presents relatively moderate resolution SAR data at the 5–20 m scale. However, it is necessary to work with multi-looked data for increased spatial correlation, producing pixels of equal dimensions and reducing data volumes in the Small Baseline Subset (SBAS) process. However, the process of multi-looking of interferograms results in misclosure of the phase loops because the filtering effect is non-conservative for some land cover types (De Zan et al., 2015). This is attributed to the vegetation and soil water content (De Zan et al., 2014; De Zan and Gomba, 2018). In regions of agriculture, careful interpretation of the apparent ground deformation is required (Jiang and Lohman, 2021) as these regions result in large signals varying in space and time if cultivated. Soil moisture effects phase closure in arid regions (Lohman and Bürgi, 2023). This issue is exacerbated for short-period, multi-looked interferograms such as used here that result in a fading bias (Ansari et al., 2021), a situation now prevalent with the shorter revisit time of 1–2 weeks offered by Sentinel-1 when compared to ENVISAT and ERS-1/2 acquisitions (typically spanning more than a month). There are empirical mitigation approaches that may be possible to apply at scale in future (Maghsoudi et al., 2022).

Some of these challenges have been addressed here with our processing strategies and this study provides an important historical record of recent deformation and a baseline for change detection in upcoming decades. However, future missions should also provide improvements in these areas. The recently launched Sentinel-1 C/D satellites, NISAR (Kellogg et al., 2020) and planned missions such as Harmony (Kääb et al., 2024), ROSE-L (Davidson and Furnell, 2021), and Sentinel NG (Torres et al., 2024) will be discussed later in this context.

2.2.1. Aims and objectives

We aim to produce a dataset useful for informing ideas of continental deformation and improving seismic hazard assessment. Our objectives are to produce a compilation of GNSS velocities for the AHB and use these with InSAR data to create a geodetically constrained displacement time series and average velocity fields of use to the wider community. Our approach builds on areas in the Belt where we previously produced velocity fields using Sentinel-1 from Türkiye (Weiss et al., 2020) through Iran (Watson et al., 2024), the Tian Shan and onto the Tibetan Plateau (Ou et al., 2022; Wright et al., 2026; Shen et al., 2024a; Wang et al., 2024; Fang et al., 2024a). We have updated these, and greatly expanded the spatial coverage to unify them into a single velocity field, by performing near-uniform interferometric processing with common time spans where possible. This is then tied to the new compilation of GNSS velocities we generate here for the Eurasian plate to provide a fully referenced dataset.

3. Data

Our velocity field is derived by compiling and combining two key geodetic data types that image the present-day motion of the Earth's surface: 1) GNSS and other point velocities, which provide a comparatively sparse but accurate picture of surface motion in an internally consistent reference system; and 2) InSAR time series of distributed surface displacements, which provide dense estimates of relative velocity across broad areas, but which need to be suitably referenced to be reliably interpreted over longer wavelengths.

3.1. GNSS and other point velocities

To align and reference the InSAR velocities, we compile 73,335 point velocities of surface motion across the Alpine-Himalayan Belt (Figure SB3) from 171 studies and datasets (Tables SA1–SA3). These include 63,120 GNSS velocities (of which 27,401 are 3D, 31,576 are horizontal-only and 4143 are vertical-only), 10,074 levelling rates, and 24 DORIS, 83 SLR and 34 VLBI velocities. Some of the 171 sources themselves include velocities from preceding publications; for example, the Global Strain Rate Model 2.1 (GSRM) dataset (Kreemer et al., 2014) includes velocities from 109 older studies in our study area. We aim to prioritise velocities that are at least partially based on measurements from the Sentinel-1 era, for consistency with the InSAR data; so most of the 171 main sources are from 2014 or later (Tables SA1–SA3). Section 4.1 describes the eight-step procedure we use to combine these velocities into an underpinning 3D point-velocity field (including removing many superseded older velocities in favor of newer high-quality velocities).

3.2. SAR

We use Single Look Complex (SLC) data from the Sentinel-1 C-band SAR instrument (centre frequency 5.405 GHz) with Vertical Transmit–Vertical Receive (VV) polarisation acquired by the European Space Agency (ESA). We use these data to derive surface displacement measurements across the Alpine Himalayan Belt using differential interferometry (Section 4.2). The Sentinel-1 mission provides systematic near-global radar imaging (Torres et al., 2012; Potin et al., 2016), enabling precise monitoring of long-term ground deformation at a continental scale. Most of the tectonic belts are imaged with both ascending and descending orbits (Figure SB2), providing two independent viewing geometries that enable us to separate east-west and vertical deformation.

We source the data from both the Alaska SAR Facility (Meyer et al., 2025) and also through the Near Line Archive at UK's data analysis facility for environmental science (JASMIN). The data we select typically span from early 2016 (beginning of March) to early 2024 (end of February, see Supplementary Material Appendix C for exact dates) except when we choose to initiate the time series late or finish it early to mitigate the effects of earthquakes (Section 4.4). The satellite constellation comprises both Sentinel-1A and its near identical pair Sentinel-1B (Miranda et al., 2017) during much of this time. The AHB from southern Europe to eastern China is captured by 62 partially-overlapping, 250-km-wide orbital tracks in each of the ascending and descending directions (Figure SB2). At lower latitudinal areas in our study (25°N), the tracks overlap by about two-thirds of a subswath (~50 km), and at the highest latitude (50°N) by over one subswath (~100 km). This yields complete spatial coverage and some redundancy in each direction, except at the edges of the polygon shown on Fig. 1(c), and which we use for velocity uncertainty analysis (Section 4.7). Data are typically available in both look directions, enabling us to resolve east-west and vertical components of motion with the use of GNSS to constrain north–south motions (e.g., Wright et al., 2004b; Weiss et al., 2020). An exception is the easternmost part where there is a gap in descending data between the Eastern Tibetan Plateau and Beijing around the Ordos Plateau (Fig. 1 & SB2).

We divide the entire AHB into 928 LiCSAR (Looking inside the Continents from Space) frames (Lazecký et al., 2020), consisting of 469 ascending and 459 descending frames (Figure SB2). Each frame comprises multiple bursts (typically 13 in each of the 3 subswaths) acquired in Interferometric Wide Swath (IW) mode (Geudtner et al., 2014) using Terrain Observation by Progressive Scans (TOPS) (Yagüe-Martínez et al., 2016). The total dataset includes 221,319 Sentinel-1 epochs, providing a dense spatio-temporal sampling of surface displacement across the region. From 2016 to 2021, the region from southern Europe to eastern Türkiye was covered by 6-day repeat-pass acquisitions, benefiting from the combined operation of Sentinel-1A and Sentinel-1B. However, following the failure of Sentinel-1B in December 2021, the acquisition frequency for this region was reduced to 12 days. For the rest of the study area, including the central and eastern portions of the AHB, the 12-day repeat cycle was used throughout the observation period where possible, although some tracks experience longer revisit times and temporal data gaps.

3.3. Ancillary data

In addition to the SAR datasets themselves, a number of ancillary datasets are needed in the processing chain (Fig. 2), in particular to apply corrections to the interferograms for phase changes resulting from

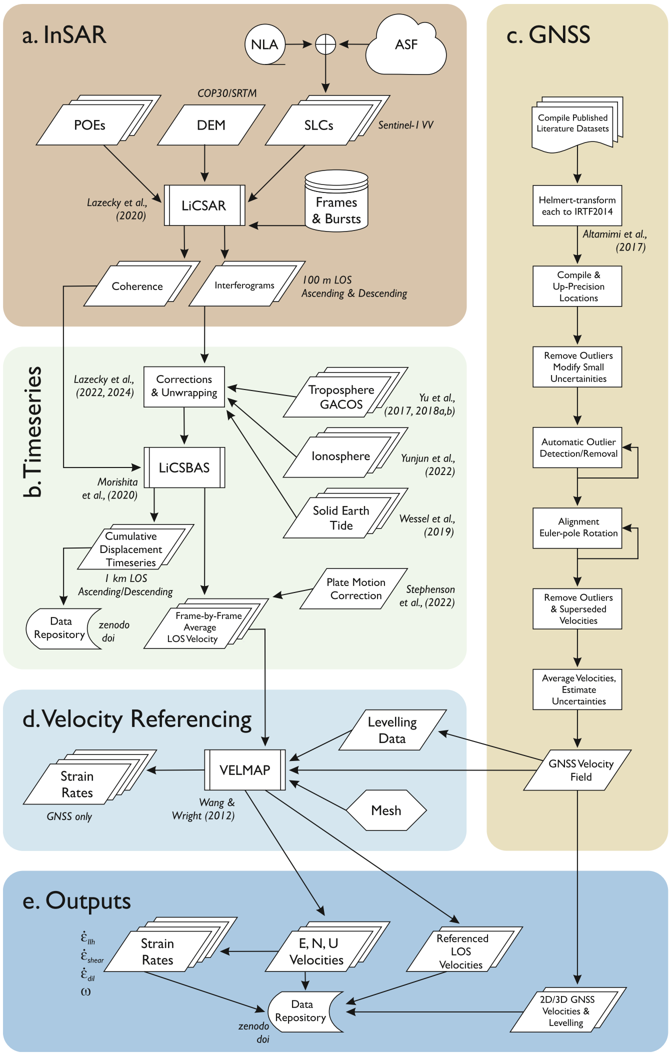

Fig. 2. Workflow for (a) InSAR processing chain and (b) correction and time series calculation, (c) GNSS compilation, quality control and alignment, (d) unified velocity generation and (e) final strain rate field calculations and outputs. InSAR - Interferometric Synthetic Aperture Radar, NLA - Near-Line Archive, ASF - Alaska SAR Facility, POE - Precise Orbital Ephemerides, DEM - Digital Elevation Model, COP30 - Copernicus 30 m, SRTM - Shuttle Radar Topography Mission, SLC - Single Look Complex, VV - Vertical Transmit–Vertical Receive Single Polarisation, LiCSAR - Looking inside the Continents from Space SAR, LOS - Line-of-Sight, LiCSBAS - Looking inside the Continents from Space Small Baseline Subset, GACOS - Generic Atmospheric Correction Online Service, GNSS - Global Navigation Satellite System, ITRF2014 - International Terrestrial Reference Frame, E, N, U - East North, Up. $\dot{\epsilon}_{II_h}$ = second invariant of strain rate, $\dot{\epsilon}_{shear}$ = maximum shear strain rate, $\dot{\epsilon}_{dil}$ = horizontal dilatation rate, ω = vorticity, (Savage et al., 2001).

the changing atmosphere (Section 4.3), including phase delays through the troposphere (Yu et al., 2018b), and phase advances through the ionosphere (Yunjun et al., 2022).

We also require precise orbital ephemerides (POE) data for satellite positions to facilitate the coregistration steps between SLCs, provided by ESA (Fernández et al., 2024). In the InSAR processing, it is also necessary to account for topography in the simulated phase. Additionally, a geographic dataset is required to reference the interferograms from radar to the geographic coordinate system. To address these two requirements, we use either the SRTM (Farr et al., 2007) or Copernicus GLO-30 (Rizzoli et al., 2017) Digital Elevation Models (DEMs) (as recorded in the metadata for each frame).

4. Methodology

Our approach starts with combining published GNSS and point velocities into an underpinning (lower-resolution) 3D velocity field across the Alpine-Himalayan Belt (Fig. 1). We then create line-of-sight velocities and time series from ESA Sentinel-1 satellite radar data through interferometric processing. The InSAR velocities are combined with the aligned GNSS velocities to create surface velocities in a Eurasia-fixed reference frame and strain rates as output datasets for further interpretation (Fig. 2).

4.1. GNSS: generating a reference frame

We use an eight-step procedure to combine the GNSS and point-velocity datasets into a unified velocity field (Fig. 2(c)). In step 1, we transform each individual dataset's velocity field into the ITRF2014 no-net-rotation (NNR) reference frame (Altamimi et al., 2017) using *itrstrafo* (Wasmeier, 2025). Because individual studies used different reference velocities and methods to get into their original reference frames, some systematic differences will remain between these rotated velocity fields; we handle these in step 5.

In step 2, we "up-precision" the GNSS station locations by grouping collocated velocities and using the most precise available location for each station as the single location for all velocities at that station. Because the original compiled station locations are not identical (usually due to studies' varying rounding practices), we define that two velocities are collocated if (1) they have the same station code and their locations are no more than 1.6 km from each other (equivalent to a 0.01° difference in both longitude and latitude, to allow for the case of one study truncating 0.005°E, 0.005°N as 0.00°E, 0.00°N while another study rounds it to 0.01°E, 0.01°N), or (2) their locations (regardless of station codes) are within 0.16 km of each other (a 0.001° difference in longitude and latitude). We use a larger threshold distance in case (1) for a few studies that round locations to the nearest 0.1° or contain numerous location errors. We then rotate all of the velocities into the ITRF2014 Eurasia-fixed reference frame (Altamimi et al., 2017) for easier visual inspection (Figure SB3).

In step 3, we begin filtering the velocity field. We first remove 1469 velocities that (1) have implausibly large horizontal components (> 100 mm/yr) in either the ITRF2014 NNR or ITRF2014 Eurasia-fixed frame, (2) have uplift or subsidence rates of > 40 mm/yr (indicating likely contamination by non-tectonic processes such as subsidence from water extraction), (3) are based on < 1.5 years of data, (4) have relatively large uncertainties of > 5 mm/yr in the east or north component or > 8 mm/yr in the vertical component, (5) have uncertainties that are unspecified or are given as zero and cannot be re-estimated from station metadata, (6) are indicated to be problematic by their contributing studies or subsequent studies, or (7) are otherwise clearly problematic but are not flagged by the automatic outlier-removal algorithm we use subsequently (usually due to having too few velocities nearby). These threshold values were all set based on testing and/or external considerations: for example, we use a duration cutoff of 1.5 yr rather than the commonly used 2.5 yr (Blewitt and Lavallée, 2002) in order to retain some of the only available velocities in Afghanistan.

There are 102 other velocities for which the uncertainties are unspecified or given as zero but can be re-estimated using the indicated data timespans and numbers of occupations at each station. We use these metadata to re-estimate these 102 uncertainties using a model of combined random-walk, white and flicker noise, with noise coefficients taken from Castro-Perdomo et al. (2022); Williams et al. (2004); Wang et al. (2012) and equations from Beavan et al. (2016); Williams (2003); Bos et al. (2008). We also change very small nonzero GNSS velocity uncertainties to "minimum reasonable" values, which we estimate from the lower ends of the distributions of velocity uncertainties in Steffen et al. (2025); Piña-Valdés et al. (2022); Socquet and Janex (2019); Serpelloni et al. (2022). We take the 0.135th-percentile uncertainty value from each of these studies (which would be the -3σ value in a normal distribution) and compute the geometric mean of these values (separately for horizontal and vertical components), yielding “minimum reasonable” uncertainties of 0.042 mm/yr for horizontal components and 0.15 mm/yr for verticals. Nonzero uncertainties smaller than these values are changed to them.

In step 4, we filter the velocity field further by using an iterative procedure to automatically identify and remove anomalous velocities. For each velocity V_A, we compare each component V_{Ai} of that velocity to the distribution of that component of velocity at nearby stations, $[V_{Bi}, \ldots, V_{Ni}]$. “Nearby” is formally within a maximum distance from V_A. Through trial and error, we set this maximum distance to 175 km, just less than the widths of most of the Red Sea and Persian Gulf and of the central parts of the Black and Caspian Seas (in order to avoid mixing velocities across them). As implemented, if V_{Ai} differs from both the median and mean of $[V_{Bi}, \ldots, V_{Ni}]$ by more than ∼3–4 times the mean absolute deviations (MADs) of $[V_{Bi}, \ldots, V_{Ni}]$ about those central values, then V_A is flagged as an outlier. In order to flag the largest outliers first and remove them from subsequent evaluations of other velocities, we implement that “∼3–4” factor above formally as a gradually decreasing scalar multiple C of the MADs, with more and more outliers progressively flagged and removed over many iterations as C is decreased towards a minimum value. Through trial and error, we choose a minimum value of 3.25 for C. For robustness, we require that a V_{Ai} cannot be evaluated as a possible outlier unless there are at least 5 uniquely located velocities within 175 km of it (with component i); and to increase spatial adaptiveness, if there are more than 25 uniquely located velocities with component i within 175 km of V_A (the case for most sites in Europe), we only use velocities from the nearest 25 locations. These parameter values were set through extensive testing, and versions of the algorithm without one or more of these constraints yielded less satisfactory results. As implemented, this algorithm flags and removes 6799 outliers, leaving 65,066 velocities (Figure SB4).

In step 5, we align the velocity datasets (minimise the remaining systematic differences between them) using an iterative approach. For each study S_A, we tabulate the differences in horizontal velocities between it and all other studies $[S_B, \ldots, S_Z]$ at sites $i, j \ldots$ that S_A shares with each. This velocity differences vector is here called $[D_{AiBi}, D_{AjBj}, \ldots, D_{AgZg}, D_{AhZh}]$, and we also compute the formal uncertainty on each velocity difference. The idea is to fit $[D_{AiBi}, D_{AjBj}, \ldots, D_{AgZg}, D_{AhZh}]$ to a rotation about an Euler pole, R_A, using least squares (Ader et al., 2012); R_A would then be subtracted from S_A to reduce its systematic velocity differences from other studies. If S_A is systematically misaligned with other overlapping datasets, R_A should be a coherent rotational adjustment, while if S_A is well aligned with others, the velocity differences should be incoherent and R_A should have effectively zero magnitude. In estimating R_A, we implement several measures to guard against model overfitting. First, we do not include velocity differences between S_A and S_B if they share < 3 sites (Rui and Stamps, 2019) or only share sites over a very small total area. Second, rather than fitting $[D_{AiBi}, D_{AjBj}, \ldots, D_{AgZg}, D_{AhZh}]$ to a single Euler-pole model, we take 1000 random-length subsamples of that difference vector and add random noise to each subsample (normally distributed random noise scaled by the formal uncertainties on the velocity differences included). We then fit each “noised” subsample to an Euler-pole rotation model and compute the model-predicted velocity adjustments at all sites in S_A. If these predicted adjustments vary in azimuth by ≥90° across S_A, we infer that the model is overfit and discard the solution. If more than 900 solutions out of 1000 are discarded, we replace the Euler-pole rotation with a model of a uniform shift in eastward and northward motion and recompute all 1000 models. In either case, we take the median of the non-discarded model predictions as the adjustment to be applied to S_A.

The iterative approach we use is to estimate these adjustments for each of the 171 datasets simultaneously, apply 5 % of each adjustment to its study, recompute all the adjustments, apply 5 % of each new adjustment, and so on for N iterations. (Applying 5 % at a time yielded better convergence than any larger fraction.) To choose the number of iterations N, we note that progressively subtracting 5 % of a number (e.g., a velocity difference) N times leaves 0.95^N of the original number, and 135 is the lowest N for which $0.95^N < 0.001$, so we use $N = 135$ iterations.

The final issue is how to treat studies that include previous studies' velocities and have already aligned these within their own combinations (e.g., Kreemer et al., 2014; Khorrami et al., 2019; Wang and Shen, 2020). Here we refer to these as compilations for brevity (although they are not purely compilations as they usually include their own processed velocities as well). In principle these compilations could be treated as single unified datasets, although on inspection we do observe some systematic (generally small) differences between how different compilations align and handle older velocities. Therefore, we first run 135 alignment iterations in which we treat compilations as single datasets, then run a second 135 iterations in which we split compilations out into their constituent parts and treat those as independent datasets (approximately 315 in total). (The one exception is that we split out (Kreemer et al., 2014) into its constituent parts from the beginning.) The aligned velocity field after these 270 total iterations is shown in Figure SB5.

In step 6, we rerun the automatic outlier detector on the aligned velocities and remove 62 additional velocities that now qualify as outliers.

In step 7, we filter out duplicate and superseded velocities in favour of velocities from studies with relatively few outliers. First, we separate the 171 studies into those that provide 3D velocities, horizontal-only velocities (2D), a mix of 3D and horizontal-only (“2.5D”), and vertical-only. We define a threshold fraction, T that is incrementally decreased from 1.0 to a minimum of 0.1. For each value of T, we find any study, S_A, that has a fraction larger than T of its original velocities flagged as outliers and removed. If there is an overlapping study S_B that (1) has an outlier fraction less than T and (2) has a dimensionality at least as large as S_A (e.g., S_A provides horizontal velocities and S_B provides 3D, 2.5D or 2D velocities), then all of S_A's velocities at sites also covered by S_B are removed. (The one exception to the dimensionality rule is that studies with vertical-only velocities cannot be superseded by studies that are horizontal-only or 2.5D.) This procedure removes 21,436 velocities, leaving 43,568 remaining (Figure SB6). Most of the velocities based wholly on pre-2014 (pre-Sentinel) data are removed in this step: many of those were contributed by the compilations of Kreemer et al. (2014) as well as by Palano et al. (2018); Serpelloni et al. (2013), and those studies have relatively low outlier fractions of 0.12, 0.14 and 0.17, but nevertheless retain only 18 %, 9 % and 7 % of their velocities after this step (respectively) due to mostly overlapping with studies with even lower outlier fractions such as Wang and Shen (2020) (outlier fraction 0.015), Khorrami et al. (2019) (0.018), Pintori et al. (2022) (0.018), Piña-Valdés et al. (2022) (0.042), Steffen et al. (2025) (0.049) and others. A few studies completely overlap with another study with a lower outlier fraction (and at least the same dimensionality) and so have no velocities retained (Tables SA1–SA3).

Finally, in step 8, we combine velocities that are collocated (here defined as within 1.6 km of each other). At locations with multiple velocities, we take the combined velocity in each component (east, north and up) to be halfway between the mean and the median of the available velocities in that component. To estimate the uncertainty on this combination, we represent each of the available velocities by a Gaussian PDF (with sigma equal to its velocity uncertainty) and combine these into a single PDF. We compute two uncertainty metrics for the mean - the standard deviation of the combined PDF, and the MAD of the combined PDF about the mean multiplied by 1.2533 (Geary, 1935) - and likewise for the median, yielding four possible pairings with which to formally represent the uncertainty on the average of the mean and median. We compute the sum of squares of each pair (halving the individual uncertainties, as we are estimating the overall uncertainty on half the mean plus half the median) and average these as the preferred uncertainty estimate for each component of velocity. At locations with only one velocity, we simply use it and its uncertainty as the final values.

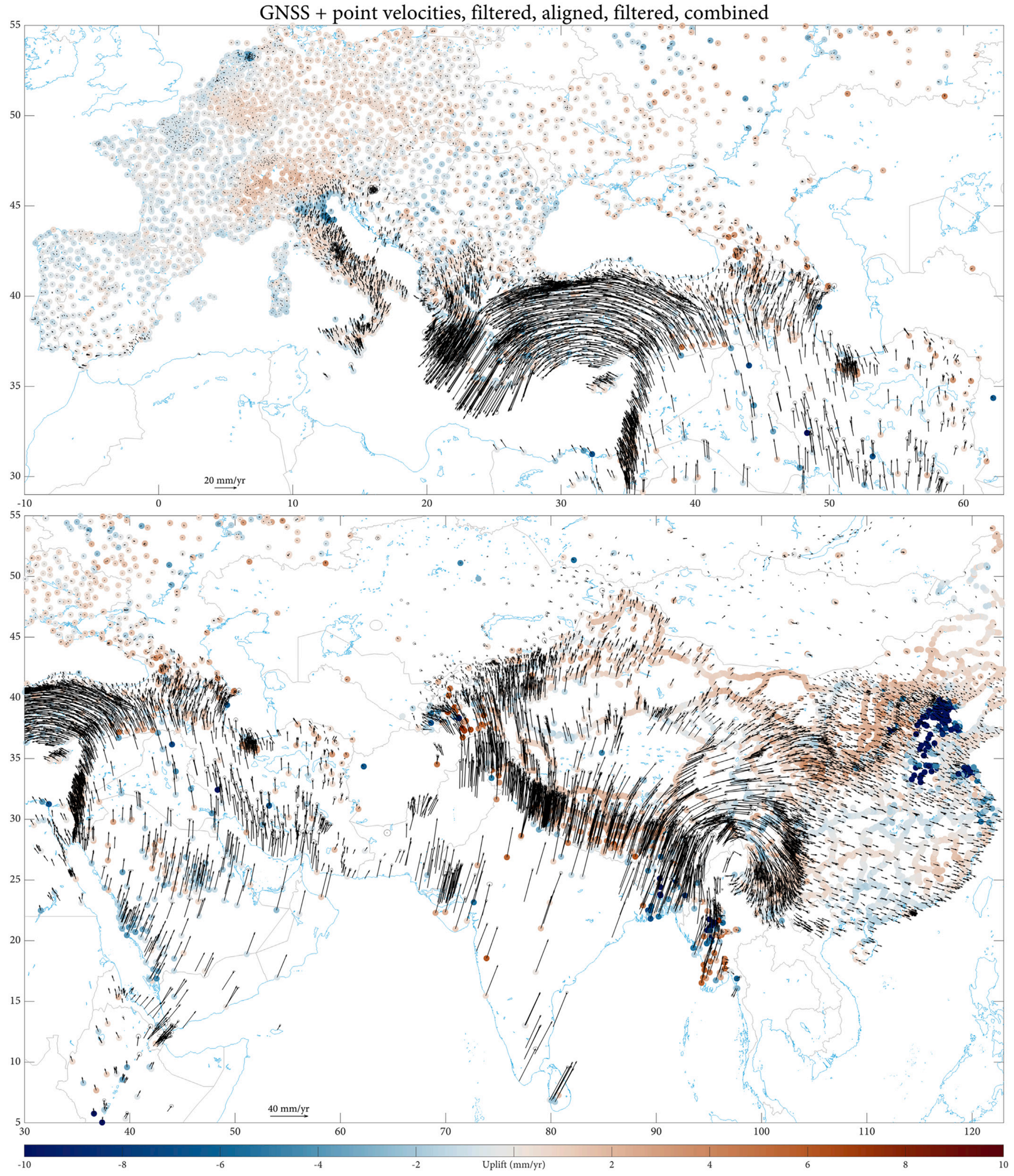

Fig. 3. The prepared 3D combination of GNSS and point velocities used to reference and align the InSAR data, in the western AHB (top) and central/eastern AHB (bottom). Arrows show horizontal motions with respect to the ITRF2014 Eurasia-fixed reference frame (Altamimi et al., 2017); coloured circles show vertical motion rates.

At the end of this combination of steps (Fig. 2(c)), there are 21,476 point velocities spanning the Alpine-Himalayan Belt, including 6668 3D velocities, 5384 horizontal velocities and 9424 vertical rates (Fig. 3). In total, 12,052 velocities provide constraints on horizontal surface motion (i.e., are 2D or 3D) and 16,092 constrain vertical motion (are 3D or pure vertical).

4.2. LiCSAR: from SAR to InSAR

We adapt the methodology outlined in Lazecký et al. (2020), starting from Level-1 Single Look Complex data from Sentinel-1A/B (Fig. 2) to generate a redundant network of over 1,200,000 interferograms over the Alpine-Himalayan Belt. The interferograms are multilooked and geocoded to grids of 0.001 degrees (approx. 110 m) resolution in the WGS-84 reference system. The good orbital control of the Sentinel-1 constellation results in a relatively tight orbital tube with perpendicular baselines typically within ±200 m that enables us to more easily generate coherent interferograms without applying baseline thresholds. As well as the standard four consecutive interferometric connections (forwards and backwards) per temporal epoch (same for both 6 or 12 days revisit time), we densify the network by forming additional combinations that cover longer time periods of up to 12 months for some regions such as the Tian Shan. Including long-span interferograms in such networks helps overcome limitations such as data gaps due to decorrelation resulting from the presence of seasonal snow and a fading phase bias that can affect short-span interferograms (Maghsoudi et al., 2022).

To ensure data consistency and avoid errors from the early time-series, we select the time period from March 2016 up to March 2024, and perform an updated phase unwrapping routine (Lazecky et al., 2022). The phase unwrapping utilizes an up-to-date version of SNAPHU at its core (Chen and Zebker, 2002) and is performed on the original LiCSAR geocoded unfiltered interferograms that are further multilooked by a factor of 10 in both latitude and longitude, yielding the final resolution of 0.01×0.01 degree (approximately 1×1 km), and corrected for some of the non-tectonic signals (Section 4.3), where line-of-sight correction maps were generated per epoch and combined to form simulated correction interferograms. Removal of these terms improves the quality of the unwrapping procedure as observed in LiCSBAS (Looking Inside the Continents from Space Small Baseline Subset) quality metrics (Morishita et al., 2020) described later. For a portion of frames, the unwrapped data with coherence (Figure SB9) estimated below 0.15 were masked prior to the time series inversion, effectively avoiding the propagation of errors due to noise into the inversion. The processing parameters were optimised for each individual frame, with parameters listed in Supplementary Materials Appendix C.

4.3. Corrections of atmospheric and tidal signals in interferograms

A number of corrections are made on an epoch-by-epoch basis to reduce the noise (Fig. 2). This includes phase delays/advances from both the troposphere and ionosphere and non-tectonic surface deformation from solid earth tides, which we can model and remove. An analysis of average correction gradients shows that the effect of the troposphere is an order of magnitude higher than the other terms (Figures SB7 and SB8). The velocities inverted from ionosphere corrections also display significant quasi-planar ramps (Fig. 4) for ascending frames (acquired at ~6 p.m. local time).

4.3.1. Troposphere

We use the tropospheric corrections derived by the Generic Atmospheric Correction Online Service for InSAR (GACOS, Yu et al. (2018b,a)), which generates zenith total delay maps (combined wet and hydrostatic delays) from the High Resolution ECMWF weather model at 0.1-degree spatial and 6-hour temporal resolutions. We convert them to slant range delays using the incidence angle for each pixel based on our East, North, Up unit vector files for each frame for the line-of-sight pointing vector from the satellite to the ground (Figure SB10).

4.3.2. Ionosphere

We follow the method of Yunjun et al. (2022) and extract total electron content (TEC) values from GNSS-based global ionospheric maps (GIMs) produced by the Centre for Orbit Determination in Europe

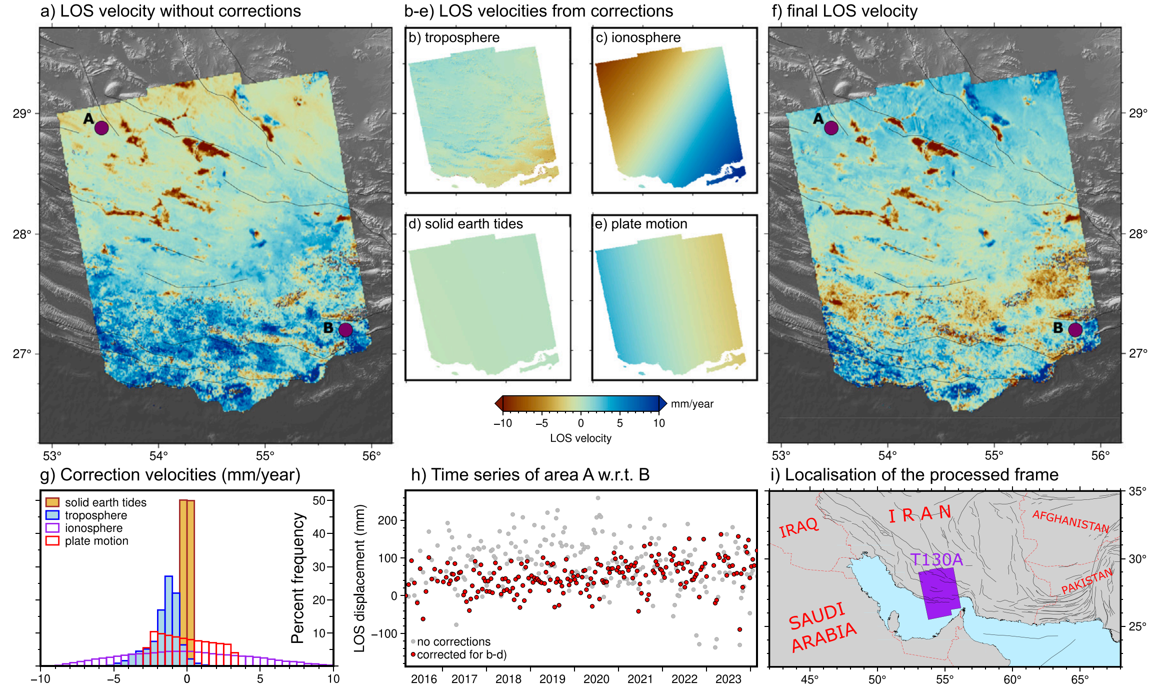

Fig. 4. Application of corrections on example frame 130A_06248_212118 over the Zagros mountains of southern Iran: a) LOS average velocity from original time series of uncorrected interferograms; b–d) velocity inverted from time series corrections on troposphere, ionosphere and solid earth tides, respectively; e) plate motion velocity correction (Figure SB14); f) final LOS velocity with all corrections applied; g) normalized frequency histogram of the b–e correction velocities; h) relative LOS displacement time series between locations A and B (reference), locations shown in subpanels a,f, from both datasets before and after b–d corrections. i) Inset map of Iran with location of frame coverage extents denoted in purple. (For interpretation of the references to colour in this figure legend, the reader is referred to the web version of this article.)

(CODE) to infer the ionospheric phase advance. We interpolate TEC values with rotation and extract them at the ionospheric piercing points, assumed to be at an altitude of 450 km, with 20 km sampling. We assume that 85 % of the GIM TEC is below the satellite (Sentinel-1 orbits at $\sim$ 700 km), as suggested by an analysis using the IRI2016 model (Bilitza et al., 2017; Lazecký et al., 2023), although this ratio will vary by time of day, season and latitude. We then calculate the slant range ionospheric phase advance (Yunjun et al., 2022) and upsample it using bilinear interpolation to provide the correction (Figure SB11).

4.3.3. Solid earth tides

The long-wavelength signal from the tides due to lunisolar gravitational forces on the solid Earth has a regular periodicity and can be modelled with high accuracy, allowing correction of InSAR results to prevent temporal aliasing (Xu and Sandwell, 2020). We use the standard model, as implemented in the *earthtide* tool of Generic Mapping Tools (GMT) (Wessel et al., 2019), to calculate vectors of tidal displacements, which we transform to slant range direction and use for correction (Figure SB12).

Corrections for ocean tide loading (periodic water mass redistribution from Earth-Moon interaction (DiCaprio and Simons, 2008) can also be made. However, this is more important for regions with large tidal ranges, such as NW Europe. However, the impact on mean velocities for long time series averaged over many years, as in this study, is below 1 mm/year (Wu et al., 2024) and we do not apply the correction here.

4.4. LiCSBAS: time series inversion and corrections

We perform time series inversion of the input networks of unwrapped corrected interferograms with $0.01° \times 0.01°$ resolution using a Small Baselines Subset (SBAS) method that allows for high spatial coverage in regions with reasonable interferometric coherence (Li et al., 2022). Specifically, we use an updated version of the LiCSBAS algorithm (Morishita et al., 2020; Morishita, 2021) that implements a method that retains some data points that were previously masked due to transient noise or incoherence, on the assumption of a constant velocity. We initially use the full network of interferograms generated with temporal and perpendicular baselines as described in Section 4.2.

Prior to the time series inversion, we identify and exclude coseismic interferograms over significant earthquakes (Section 4.4.1), introducing data gaps in the input network. Those gaps are spanned during the later inversion on the assumption of a constant velocity. We identify relatively stable reference areas based on spatio-temporal statistics of the interferometric network and generate interferometric phase loop closure triplets $I_{ABC} = I_{AB} + I_{BC} - I_{AC}$ for all possible combinations of interferograms I from acquisition dates A, B, C. We assume that residuals in triplets formed from correctly unwrapped interferograms should be smaller than π radians. As our interferometric network is highly redundant, we use the phase loop closure information to identify and drop pixels with unwrapping errors (Shen et al., 2024b; Lazecký et al., 2024). We also allow for possible overall shifts of up to ± 2 phase cycles due to an inconsistent reference area. Additionally, we calculate the mean of the absolute wrapped phase loop error per pixel, as an indicator of potential phase bias (Figure SB13). This is later used as one of the quality measures for the masking of noisy pixels.

Using weights derived from individual coherence maps (Morishita et al., 2020), we perform weighted least squares inversion of the interferometric network into temporal increments that, after cumulating in time, form displacement time series. We store the root mean square error (RMSE) of residuals from this inversion and use its average value per interferogram to identify and drop noisy input interferograms from the network for some frames, then repeat the inversion. This is done exceptionally for whole interferograms where the average loop closure phase is extremely high (over 10 radians). Typically, though, we apply a pixelwise nullification approach (Shen et al., 2024b) that reduces the inversion RMSE by removing only erroneous pixels within individual interferograms rather than whole interferogram. As interferograms not forming loop closures remain in the dataset, the RMSE of residuals can still remain high in case of unwrapping errors. Thus we additionally use this measure for masking noisy pixels (with a default value of 12 mm for most frames) amongst other quality measures (Supplementary Information Appendix C).

After masking noisy pixels using the phase bias indicator, residuals RMSE, and several other quality measures (Morishita et al., 2020), we perform spatio-temporal filtering of the cumulative time series to estimate residual atmosphere that is correlated spatially but not temporally on short time scales (Hooper et al., 2007). This is achieved by high-pass filtering in time (using a Gaussian window of width of usually 36 or 72 days, which is three times the average interval between epochs) and low-pass spatial filtering (using a Gaussian window of 2 km width at 1σ truncated at 8σ to yield a 17×17 pixel kernel, given the 1 km pixel spacing). After subtracting the estimated atmosphere, we estimate the mean velocity using unweighted least squares. We use the original unfiltered time series to estimate the velocity standard deviation using bootstrapping (Efron and Tibshirani, 1986), which we further flatten based on a semivariogram analysis to remove the influence of distance from the reference area (Ou et al., 2022) and provide a measure of the velocity uncertainty (Figure SB15). Finally, we estimate and subtract Eurasian plate motion for all frames (Figure SB14), including those outside Eurasia, by calculating velocities of rotation around the Eurasian plate Euler pole (Stephenson et al., 2022). Some of the key processing parameters are listed in Supplementary Information Appendix C per frame, as they vary by frame, particularly in individual masking thresholds.

4.4.1. Earthquakes

InSAR is good at capturing the deformation associated with shallow crustal earthquakes of moderate to large magnitude (Funning and Garcia, 2019). However, the presence of coseismic displacements results in errors when estimating the long-term velocities associated with interseismic strain accumulation from the time series of interferogram displacements. Therefore, a mitigation strategy is employed to remove the primary effect of the earthquake coseismic deformation field itself. In order to solve for coseismic offsets or truncate the time series to mitigate against such effects, we extract a list of significant earthquakes with locations and depths from the USGS seismic catalogue. We limit ourselves to moderately sized earthquakes with magnitudes $M_w > 6.0$ which are also sufficiently shallow (< 35 km) to potentially produce a displacement signal at the surface (29 events, excluding aftershocks, Table SA4 and Figure SB16). We then manually review each event to ascertain the number of frames affected and decide whether to truncate the time series by starting it after the earthquake (if near the beginning of our time series in 2016) or stopping it before the event (if it occurs towards 2024), or, as in most cases, allowing for an offset in the time series to be solved for across the earthquake date (Table SA4). This greatly reduces the impact of the earthquake on the velocity estimation, although the impacts of any long-term postseismic signals associated with these events will still be present.

4.5. VELMAP

Following the completion of LiCSAR/LiCSBAS processing (Fig. 2), each frame is independently referenced for line-of-sight (LOS) velocity estimation (Figure SB17). To construct a unified velocity field in a Eurasia-fixed reference frame, we integrate these LOS velocities with compiled GNSS data (Fig. 3) using the approach coded from Wang and Wright (2012) called VELMAP (Wang and Wright, 2025).

We first define the outline of the triangular mesh by applying a 75 km buffer along the outermost frame boundaries, ensuring adequate GNSS and levelling coverage near the mesh edges (Figure SB18). To enhance computational efficiency and memory management, we generate the mesh with vertices spaced at approximately 40 km.

The inversion simultaneously estimates velocities at each triangular mesh node, reference frame adjustment parameters, a linear atmospheric correction term based on elevation, and a long-wavelength quadratic ramp for each frame (Wang and Wright, 2012). Three-dimensional (3D) velocities at InSAR and GNSS observation points are interpolated from the triangular mesh nodes. Before the VELMAP inversion, InSAR LOS rates are downsampled to a resolution of ∼10 km. As part of the regularisation, we apply Laplacian smoothing in the inversion, adjusting the relative strength of the smoothing term to achieve a balance between solution roughness and misfit. The combined geodetic solution is then used to generate mosaics of ascending and descending LOS velocities in a Eurasia-fixed reference frame (Fig. 6) at the original resolution of 0.01° (∼1 km).

Uncertainties in the line-of-sight velocities are propagated to uncertainties in 3D velocity model using the standard equations (Wright et al., 2004b). We construct an initial covariance matrix for the GNSS data using their formal uncertainties (Fig. 3), and for the InSAR data using the rescaled line-of-sight uncertainties estimated by LiCSBAS (Figure SB15). We then iteratively update the GNSS and InSAR covariance matrices using a variance component estimation method until their relative ratio approaches unity (Grafarend, 1984). We extract variances and covariances from the variance-covariance matrix of the estimated model parameters (3D velocity at each vertex of the triangular mesh).

4.6. 3D velocity and strain rate generation

With ascending and descending referenced line-of-sight (LOS) velocities (Figure SB17), we only have two independent components of the 3D velocity field (Wright et al., 2004b). To decompose these into the more readily interpretable eastward and vertical velocities, we follow the approach of Hussain et al. (2018) and Weiss et al. (2020) — we apply a pixel-by-pixel inversion at ∼1 km resolution, with the northward velocity constrained to be equal to the coarse resolution velocity field obtained from the VELMAP inversion (Fig. 7(a)).

We then compute the strain rate fields by taking the gradients of the median-filtered InSAR eastward velocities (Figure SB19) and the smoothed GNSS northward velocities (Fig. 7). The horizontal strain-rate tensor, $\dot{\varepsilon}_h$, represents the symmetric component of the velocity gradient tensor. We derive the second invariant ($\dot{\varepsilon}_{II_h}$), maximum shear ($\dot{\varepsilon}_{shear}$), and dilatation ($\dot{\varepsilon}_{dil}$) of the horizontal strain-rate tensor. The second invariant of the strain rate tensor represents the overall magnitude of strain and provides a scalar measure of strain rate that is independent of coordinate orientation. The maximum shear component characterises the peak shearing deformation. Horizontal dilatation corresponds to the trace of the strain rate tensor and indicates areal extension or contraction. These are defined, including the spherical correction terms, where θ is the colatitude of each pixel and r is the Earth's radius ($r = 6378$ km), as follows (Savage et al., 2001; Kreemer et al., 2014; Sandwell and Wessel, 2016; Wang and Shen, 2020):

$$\dot{\varepsilon}_h = \begin{bmatrix} \dot{\varepsilon}_{xx} & \dot{\varepsilon}_{xy} \\ \dot{\varepsilon}_{yx} & \dot{\varepsilon}_{yy} \end{bmatrix} = \begin{bmatrix} \dfrac{\partial V_E}{\partial x} - \dfrac{V_N \cos\theta}{r \sin\theta} & -\dfrac{1}{2}\left(\dfrac{\partial V_E}{\partial y} + \dfrac{\partial V_N}{\partial x} + \dfrac{V_E \cos\theta}{r \sin\theta}\right) \\ -\dfrac{1}{2}\left(\dfrac{\partial V_N}{\partial x} + \dfrac{\partial V_E}{\partial y} + \dfrac{V_E \cos\theta}{r \sin\theta}\right) & \dfrac{\partial V_N}{\partial y} \end{bmatrix} \tag{1}$$

$$\dot{\varepsilon}_{II_h} = \sqrt{\dot{\varepsilon}_{xx}^2 + 2\dot{\varepsilon}_{xy}^2 + \dot{\varepsilon}_{yy}^2} \tag{2}$$

$$\dot{\varepsilon}_{shear} = \sqrt{\dot{\varepsilon}_{xy}^2 + \frac{(\dot{\varepsilon}_{xx} - \dot{\varepsilon}_{yy})^2}{4}} \tag{3}$$

$$\dot{\varepsilon}_{dil} = \dot{\varepsilon}_{xx} + \dot{\varepsilon}_{yy} \tag{4}$$

The rotation rate tensor is the antisymmetric part of the velocity gradient tensor. The vorticity vector, ω, is twice the rotation rate tensor (Liu et al., 2018).

$$\omega = \frac{\partial V_N}{\partial x} - \frac{\partial V_E}{\partial y} \tag{5}$$

We have masked out regions where the absolute magnitude of the vertical velocities exceeds 20 mm/yr (Fig. 7(c)), as these values are unlikely to represent tectonic signals. These regions are prevalent across Iran, and there are also large areas in China (east of the Tian Shan and south of Beijing). We have applied the same mask to the eastward velocities to ensure that these anomalous regions do not influence the overall strain analysis. To mitigate short-wavelength noise in the InSAR eastward velocities, a median filter is applied to non-NaN pixels to derive the preferred strain rate fields using a window size of ∼150 km. Although this filtering approach reduces noise, it also damps down any real short-wavelength strain signals visible in the data, for example, due to fault creep (Section 5.3.1).

4.7. LOS uncertainty analysis

The mosaics of the two InSAR line-of-sight (LOS) velocities in a common reference frame, as well as the VELMAP north velocities from GNSS, allow us to evaluate the uncertainties of our LOS velocities at track overlaps, where we have a redundancy of one LOS velocity measurement in ascending or descending (Fig. 5). Following Wright et al. (2026), we first divided the LOS velocity tracks into four groups, A1, A2, D1, and D2, each containing alternate tracks in the ascending (A) or descending (D) geometry. Instead of using all four groups of LOS velocities and the VELMAP north velocities to derive east and vertical velocities for the entire coverage, we can perform the same operation using a subset of three of the groups (e.g., A2, D1 and D2) to produce a version of the east and vertical velocities that partially overlaps with the group left out (e.g., A1). Using east and vertical velocities derived without group A1, we can independently reconstruct the estimated LOS velocities at pixels overlapping with group A1 using the observation geometries of group A1. The root-mean-square (RMS) differences between the actual observed and independently reconstructed LOS velocities are 2.7 mm/yr and 2.6 mm/yr for the ascending and descending geometries, respectively (Fig. 5(c)–(f)). The largest differences we observe typically occur in areas with snow or vegetation cover, such as the Himalayan front and northern India, central Europe, and the Caucasus (Fig. 5(a),(b)).

The above-reported values are RMS of LOS differences between 1 and 99 percentiles, corresponding to ∼-12 mm/yr and ∼12 mm/yr, respectively. With all pixels included, the RMS differences would have been 4.0 mm/yr and 4.4 mm/yr for ascending and descending geometries, respectively, which are inconsistent with the narrower histogram peaks observed in Fig. 5(d),(f) than in Fig. 5(c),(e). To avoid bias from extreme values in the lowest and highest percentiles, we therefore evaluate uncertainties based on differences between 1 and 99 percentiles for subsequent analysis.

The differences between the observed and reconstructed LOS velocities do not result from equal contributions of errors within the two datasets, as the reconstructed LOS is itself estimated from east and vertical velocities derived from three other LOS velocities, as well as the north velocities constrained by GNSS and the mesh. We first estimate the uncertainties of east and vertical velocities by calculating the differences between two independent estimates of east and vertical velocities in the diamond-shaped areas ($\sim 70 \times 300$ km, varying by latitude) that result when the land surface is overlapped by observations in all four geometries (A1 + D1 versus A2 + D2 and A1 + D2 versus A2 + D1). The RMS of 1–99 % of the differences in these independently decomposed east and vertical velocities are 2.9–3.1 mm/yr and 2.4–2.5 mm/yr, respectively (Figure SB20). Split equally between the two independent estimates, the uncertainties of east and vertical velocities derived from one ascending geometry and one descending geometry are 2.1 mm/yr and 1.7 mm/yr, respectively.

The uncertainty of the reconstructed LOS velocities can then be estimated by projecting these uncertainties of east (2.1 mm/yr) and vertical

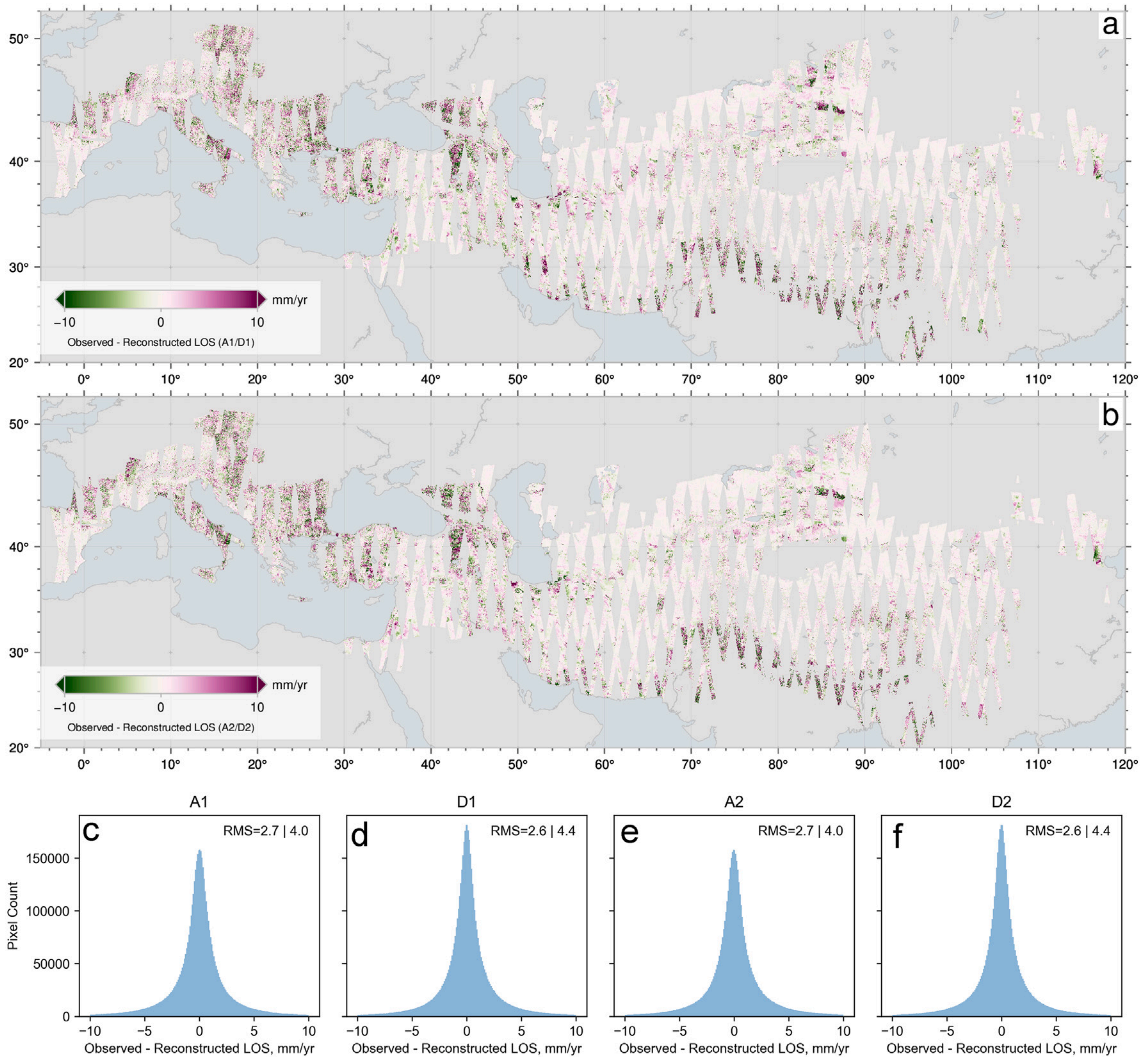

Fig. 5. LOS uncertainty analysis through the differences between observed and reconstructed LOS velocities at track overlaps. The observed LOS velocities in Fig. 6 are split into four non-overlapping groups of ascending and descending tracks, A1, A2, D1, and D2. (a–b) A1 represents the differences between the observed LOS velocities in A1 and the reconstructed LOS velocities at A1's pixel locations using LOS velocities in A2, D1, and D2. The same applies to D1, A2, and D2, respectively. (c–f) Residual and Root-mean-square (RMS) differences between the corresponding observed and reconstructed LOS velocities. The differences are reported first as RMS of 1–99 percentiles, and then of all pixels.

(1.7 mm/yr) velocities, and a conservative estimate of 3 mm/yr for the north velocity uncertainty (Figure SB21a) into the satellite's LOS (Wright et al., 2026). Taking the resulting 1.9 mm/yr uncertainty of the reconstructed LOS (which is typically dominated most by the vertical and least by the northern uncertainty due to the viewing geometry), out of the 2.7 mm/yr and 2.6 mm/yr differences between observed and reconstructed ascending and descending LOS velocities yields an estimated 1.9 mm/yr and 1.8 mm/yr uncertainties of the observed ascending and descending LOS velocities respectively.

The slightly lower uncertainty of the descending LOS velocities compared to that of the ascending LOS velocities is expected as the interferograms created from data acquired along descending tracks contain lower levels of tropospheric and ionospheric noise, being acquired at dawn rather than dusk (Figures SB7, SB8, SB10 and SB11). This is a time when the troposphere experiences less convective turbulence than at the end of the day and also, a period when the ionosphere is only beginning to increase in ionisation and generate its extra sublayers in the daytime.

We then propagate the LOS uncertainties through the decomposition equation to derive pixel-wise uncertainties of east and vertical velocities (Figure SB22). The RMS of the pixel-wise uncertainties are 1.9 mm/yr for east velocities and 1.5 mm/yr for vertical velocities, lower than before because of constraints from all geometries.

These uncertainties compare well with the 2.4 mm/yr differences between InSAR and GNSS east velocities, 3.1 mm/yr differences between InSAR and GNSS vertical velocities, and 1.8 mm/yr differences between InSAR and levelling vertical velocities (Figure SB23). These results are consistent with our expectations of InSAR east velocities being less accurate than GNSS east velocities, and InSAR vertical velocities being more accurate than GNSS vertical velocities (due to InSAR's incidence angles between 30–45°), but less accurate than levelling-derived vertical velocities.

5. Results

We first describe the line of sight velocity fields that result from combining all the individual frames, before moving on to the 3 components of velocity from the combined decomposition of InSAR and GNSS data. We then show our results for the strain rate calculations for the whole AHB. A zoomed in discussion of the details of the velocity

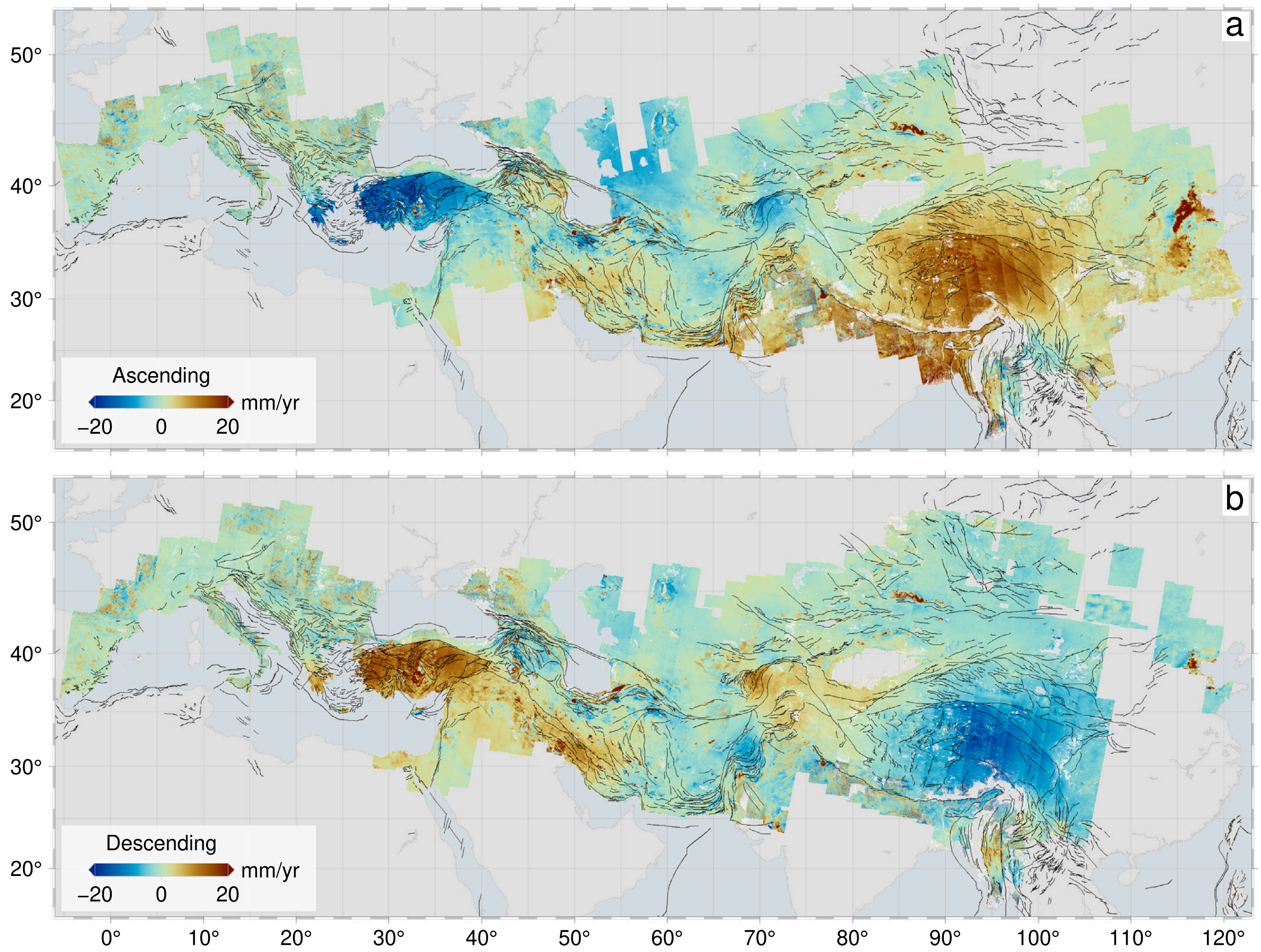

Fig. 6. Mosaic of referenced line of sight average velocities for the Alpine Himalayan Belt on (a) ascending and (b) descending orbital heading directions, with positive values indicating motion away from the satellite. Active fault traces (black lines) are from Styron and Pagani (2020). (For interpretation of the references to colour in this figure legend, the reader is referred to the web version of this article.)

and strain rates for each of the major tectonic region is given in the Supplementary Information (Section 3), where we focused in on the regions deforming as a response of the Arabia collision zone of Turkey (Figure S1), Iran and Makran (Figures S2 & S3) before moving onto those responding to the India collision in the Pamirs (Figure S4), Tian Shan (Figure S5) and across the Tibetan Plateau (Figures S6 & S7). We finish here by showing signals across the AHB associated with creeping faults, postseismic deformation following major earthquakes, and land subsidence due to water extraction.

5.1. *Surface velocities*

The Eurasia-fixed ascending and descending LOS velocities (Fig. 6) offer a comprehensive view of surface motions across the entire AHB. The most notable feature is the pronounced gradient in velocity across the major fault systems, such as the North and East Anatolian Faults (Figure S1), Main Pamir (Figure S4), Altyn Tagh (Figure S6), Haiyuan, Kunlun, and Xianshuihe Faults (Figure S7). Additional features include localized regions where there is apparent motion away from the satellite in both ascending and descending geometries. This consistent motion in both directions suggests subsidence in these areas, likely due to human activities such as water extraction, as observed in regions such as Türkiye, Iran, and the North China Plain (Section 5.3.3).

The northward velocity field (Fig. 7(a)), largely constrained by the GNSS observations (Fig. 3), reveals the well-recognised north-south shortening as a result of the ongoing plate collisions. The overall gradient in the N-S velocity field at the India collision point is approximately 40 mm/yr over a distance of ∼3000 km, with around 20 mm/yr of shortening observed across the Himalayas (Fig. 8(a)), except where there is a much sharper gradient across the Chaman Fault. These gradients reflect the intense compressional forces and shear resulting from the ongoing collision between the Indian and Eurasian plates, driving the tectonic deformation in the region. The decomposed E-W velocity field (Fig. 7(b)) reveals large-scale motion across the region, with Anatolia experiencing westward motion at a rate of 20–25 mm/yr relative to Eurasia, and Tibet moving at a similar rate eastwards, with rapid rotations around the eastern Himalayan syntaxis. A localized eastward velocity gradient is observed across the major faults, as shown by a ∼8000 km profile crossing the North Anatolian, Main Pamir Thrust, Altyn Tagh, and Xiaojiang Fault systems (Fig. 8(c)). The vertical velocity field (Fig. 7(c)) is likely dominated by non-tectonic processes such as groundwater depletion and permafrost and is also noisier and harder to interpret. Values larger than ±10 mm/yr are unlikely to be tectonically related. The ∼4500 km profile (Fig. 8(e)) reveals vertical deformation across the region, with uplift north of the Makran, subsidence around the western syntaxis, Karakoram-Altyn Tagh uplift, subsidence in Qilian

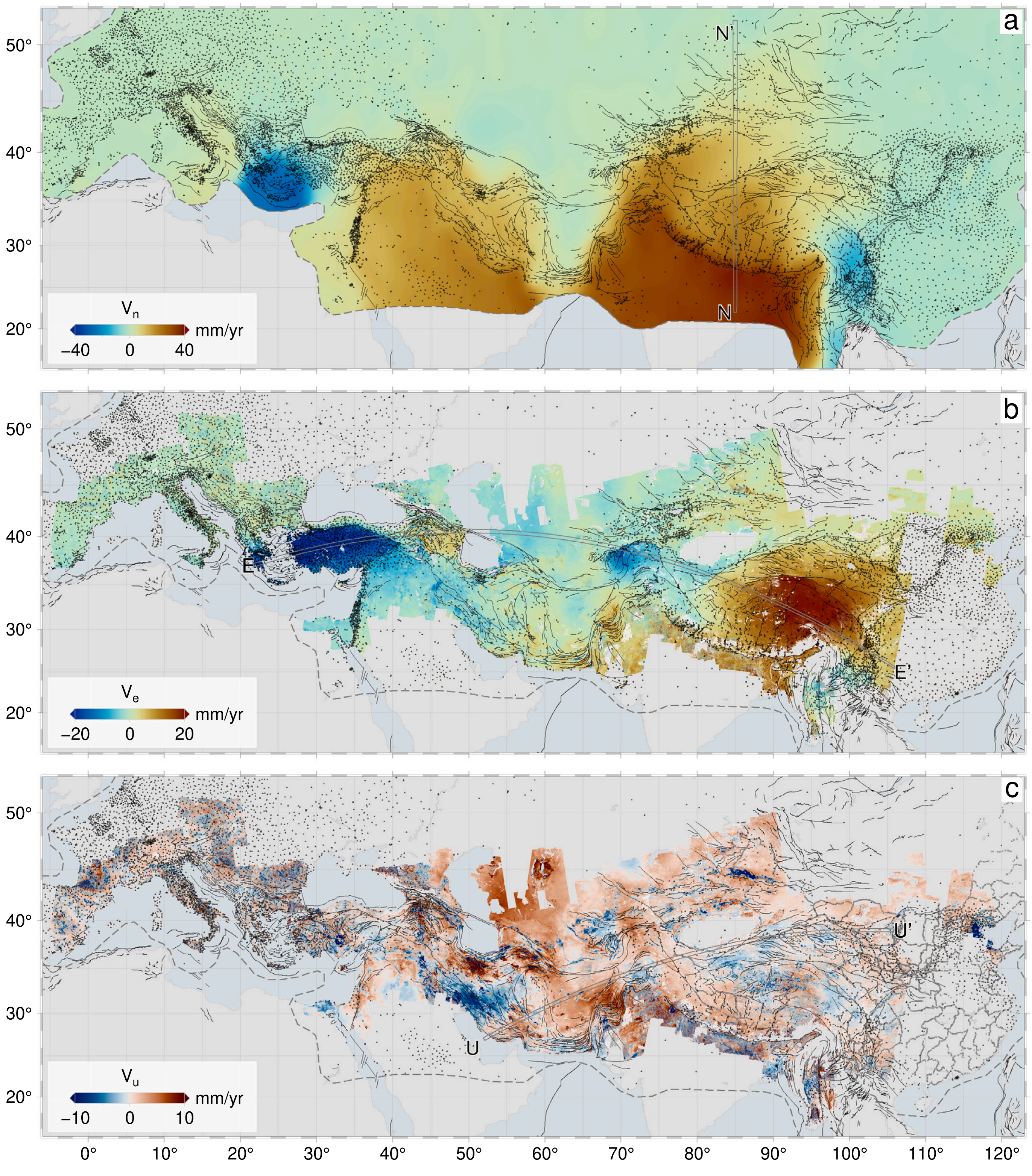

Fig. 7. Three components of surface velocity: (a) North, (b) East, and (c) Vertical. GNSS sites are denoted by circles for 2D velocities, triangles for 3D velocities and coloured squares for levelling results. The dashed outline shows the extent of the mesh used to align the individual line-of-sight velocities. Gray polygons indicate the extent of the profiles (20 km bins) presented in Fig. 8. (For interpretation of the references to colour in this figure legend, the reader is referred to the web version of this article.)

Shan due to permafrost, and uplift associated with plateau growth in the northeast.

The comparison between InSAR-derived velocities and GNSS data (Fig. 3) for the entire AHB shows an RMS of 2.4 mm/yr for eastward velocity (Ve) and 2.4 mm/yr for vertical velocity (Vu), with RMS values of 3.1 mm/yr for GNSS Vu and 1.8 mm/yr for levelling (Figure SB23). For individual regions, the RMS values are 2.5 mm/yr for Ve and 3.3 mm/yr for Vu in Europe (Figure SB24), 2.9 mm/yr for Ve and

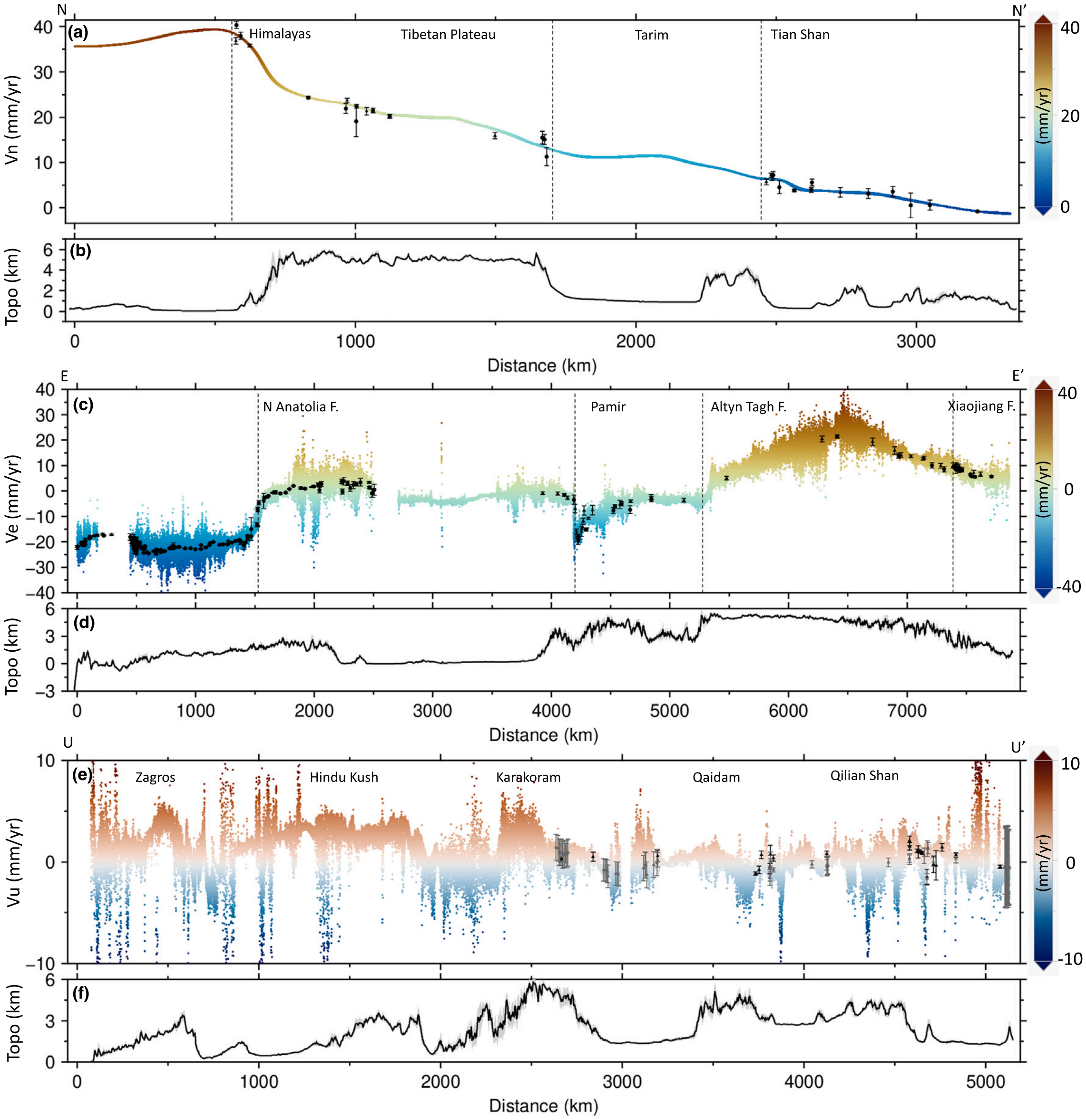

Fig. 8. Profiles across the velocity fields of the Alpine Himalayan Belt with locations of mapped active faults from Styron and Pagani (2020) marked by dashed black lines. (a) Northward component of velocity along longitudinal line 85°E, with GNSS data and topography marked on. (b) Eastward component of velocity from Greece to southeastern Tibet along the Great Circle almost 8000 km long (20 % of the Earth's circumference). (c) Vertical component through Afghanistan to northeastern Tibet. The locations of the profiles are shown in Fig. 7. InSAR data (coloured dots) are binned into 20 km wide profiles, while GNSS (black bars) and levelling (grey bars) data are binned into 40 km wide swaths. (For interpretation of the references to colour in this figure legend, the reader is referred to the web version of this article.)

3.5 mm/yr for Vu in Anatolia (Figure SB25), 1.5 mm/yr for Ve and 1.7 mm/yr for Vu in the Pamir and Tian Shan (Figure SB26), and 2.3 mm/yr for Ve and 1.8 mm/yr for Vu in Tibet (Figure SB27). These values suggest that, while InSAR captures surface motion with reasonable accuracy, there are still noticeable discrepancies, particularly in the vertical velocity component. The higher RMS value for vertical velocity may be attributed to factors such as atmospheric noise, vegetation, phase bias, or other non-tectonic influences that affect InSAR data. The formal uncertainties from the velocity decomposition of < 1 mm/yr for many areas (Figure SB15), which are propagated from the line-of-sight uncertainties of similar magnitude, do not fully capture the level of noise. The uncertainty estimates from the overlapping frame analysis (Fig. 5) of ~2.5–3.0 mm/yr and from the longer wavelength referencing from VELMAP (Figure SB21) of 2–3 mm/yr should be considered more realistic.

5.2. Strain rates

Our strain rate fields of the AHB (Fig. 9) show two styles of deformation, with focused strain concentrated along major fault systems (Fig. 9(a)–(b)) and more diffuse strain observed away from these large faults (Fig. 9(c)). The major concentrations of strain rate lie along the centre of Greece, on the North and East Anatolian Faults of Türkiye (Figure S1), across the Caucasus, along the Dead Sea Fault, the Makran and Sulaiman Ranges (Figure S3), the Pamirs (Figure S4), across the parts of the Himalayas we can image, and the major strike-slip faults of Tibet (Figures S6 & S7). Distributed strain occurs in regions such as Iran (Figure S2), and the interiors of western Anatolia and across the Tian Shan (Figure S5), as well as parts of the Tibetan Plateau away from the major faults. Whilst there is noise in these derivative fields, it is possible to discern low straining areas < 20 nstr/yr in western Europe, Northern

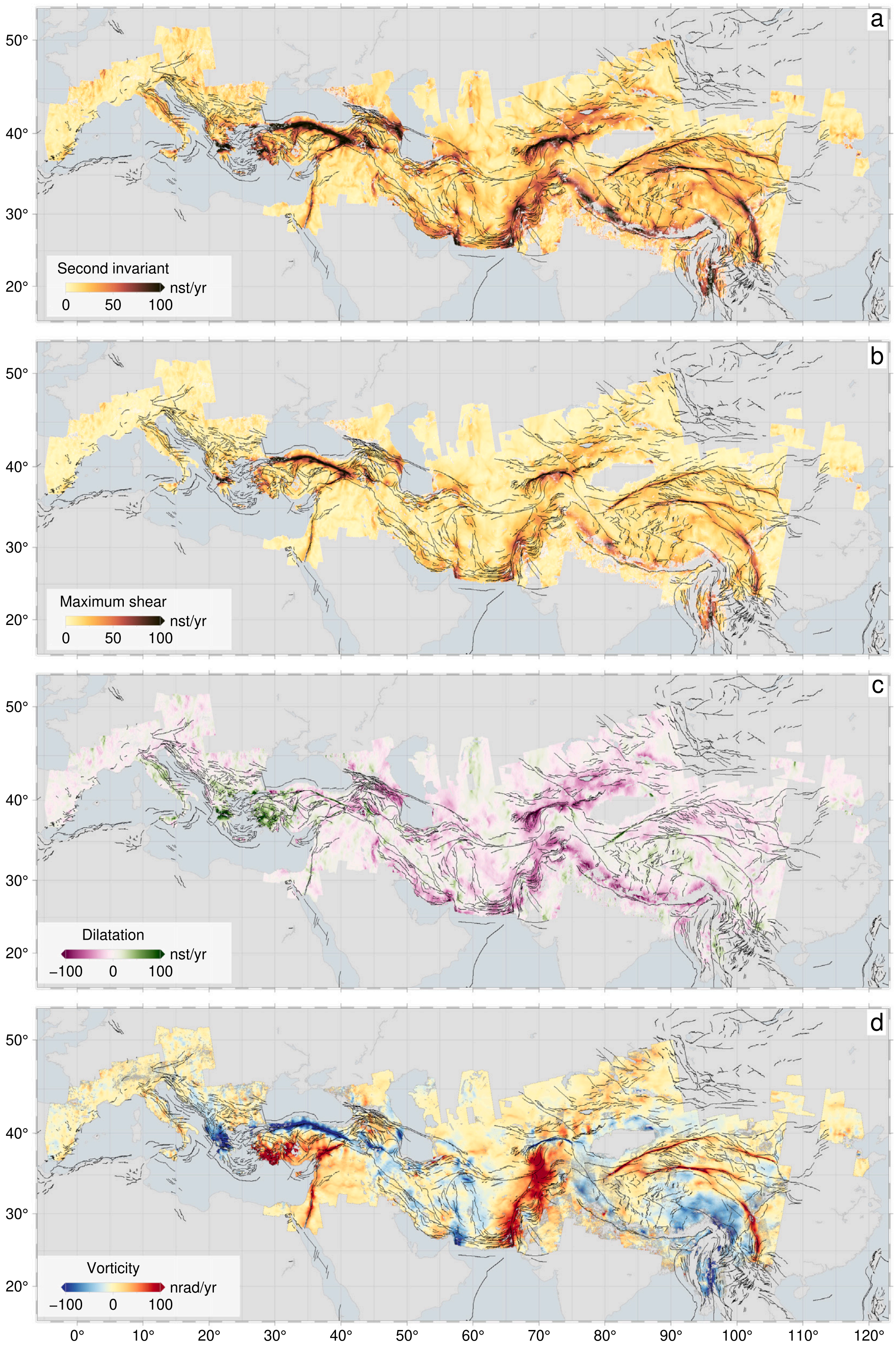

Fig. 9. Measures of horizontal strain rates for the Alpine Himalayan Belt with mapped active faults from Styron and Pagani (2020) overlaid (black lines). (a) Second invariant of strain rate (nstr/yr), (b) Maximum shear strain rate (nstr/yr), (c) Horizontal Dilatation rate (nstr/yr), where positive indicates extension and negative contraction, and (d) Vorticity (nrad/yr), with positive values indicating anti-clockwise rotation. (For interpretation of the references to colour in this figure legend, the reader is referred to the web version of this article.)

Arabia, Central Iran, Afghanistan and much of the region between the Kopeh Dagh of Iran and the Pamirs, as well as North and East of the Tian Shan.

The horizontal dilatation strain rate field (Fig. 9(c)) is particularly noisy, but viewed broadly, positive dilatation, indicating areal increase, supports known extension in Italy, through Greece and Western Türkiye (Figure S1), as well as across the bulk of the southern and central Tibetan Plateau and around the Eastern Syntaxis in Eastern Tibet. Negative dilatation associated with areal decrease and compression is pronounced across the converging regions of the Caucasus, Zagros mountains, Makran, Sulaiman ranges, Pamirs, Tian Shan, Himalayas, and Qilian Shan.

The rotation rates observed in the vorticity (Fig. 9(d)) predominately reflect the horizontal motion caused by strain accumulation along the major faults, with the direction of rotation depending on the fault's sense of slip (Fig. 9(d)). Left-lateral strike-slip faults are associated with anticlockwise rotation (e.g., East Anatolia, Chaman, Altyn Tagh, Haiyuan, Kunlun, and Xianshuihe Faults), while right-lateral strike-slip faults correspond to clockwise rotation (e.g., North Anatolian and Main Pamir Thrust Faults). These are likely not long-term rotations but reflect elastic interseismic strain accumulation around these faults. The vorticity also captures the long-term clockwise motion of Greece and south-east Tibet around the Eastern Syntaxis. The overall anticlockwise rotation of Anatolia, Northern Arabia, and the Sulaiman Ranges to Hindu Kush is also shown by the broad areas of positive rates of vorticity.

Comparison between GNSS-derived strain rate fields and those from the combined InSAR and GNSS solution shows that InSAR adds finer-scale details, typically localizing more strain onto the large fault systems such as the North Anatolian Fault and those across the Tibetan Plateau (Figures SB32 and SB29). However, in regions of low strain (< 20 nstr/yr), the InSAR can add noise, particularly where coherence is poor. The InSAR strains also contain the contributions from postseismic deformation following past major earthquakes that mostly predate our time series. This postseismic impact is most clearly identified in the difference of the two maximum strain rate fields (Figure SB32) around Kokoxili on the Tibetan Plateau and the Baluchistan earthquake in the Eastern Makran.

5.3. Further deformation

In addition to the large-scale horizontal velocities associated with long-wavelength continental deformation and the strain of interseismic accumulation across major faults, we also observe sharp velocity gradients and high strain rates associated with individual creeping segments of strike-slip faults and also the elevated strains over regions with past earthquakes. We also observe the largest signals in the vertical associated with non-tectonic signals due to water subsidence across the belt and present a number of such examples, as well as the influence of permafrost on surface velocities across the Tibetan Plateau.

We have separated out these sources of deformation based upon visual inspection of the wavelength and magnitude of the signals, the dominance of horizontal motion, and whether they are associated with recent large earthquakes, or previously identified creeping faults. Conversely, those signals associated with subsidence due to water extraction are dominated by vertical deformation, are larger in magnitude (> 10 mm/yr), vary seasonally in the timeseries and are highly correlated with vegetated areas in arid regions close to population centres. We have not examined motion associated with events such as steady landsliding as our coarse velocity fields at 1 km would not be able to delineate short wavelength signals.

5.3.1. Creeping faults

Earthquakes are not the only mechanism by which the crust releases its elastic strain. Many previous studies (Avouac, 2015; Harris, 2017; Jolivet and Frank, 2020) have shown that the elastic strain accumulated in the shallow crust can be released aseismically without producing huge seismic waves or causing sudden movement of the shallow crust. Compared to most active faults, which are fully locked from the surface down to the seismogenic depth during the interseismic period (Reid, 1911), creeping faults are those that are not fully locked; instead, slow, aseismic slip occurs in the periods between earthquakes. Creeping faults are typically not well identified using GNSS datasets as the GNSS velocities are normally too sparse to distinguish shallow creeping and shallow locking depth and instead this is usually best captured with creepmeters (Bilham et al., 2016). High-resolution InSAR velocities can capture the near-fault deformation pattern over wider areas to better identify whether a fault is creeping. Across the Alpine Himalayan Belt, previous InSAR studies have identified several creeping faults, including parts of the North Anatolian fault (e.g., Cakir et al., 2005; Hussain et al., 2016; Jolivet et al., 2023), Chaman fault (e.g., Fattahi and Amelung, 2016; Barnhart, 2017; Dalaison et al., 2021), Haiyuan fault (e.g., Jolivet et al., 2013), Xianshuihe fault (e.g., Qiao and Zhou, 2021) and Gozha Co fault (e.g., Huang et al., 2023).

By studying our velocity field and strain rates around some of these creeping faults, we observed obvious steps in our east velocity field and high shear strain rates running along them (Fig. 10). The pattern of velocity steps and maximum shear strain rates indicates the spatial extent, creeping rates, and creeping depth. Taking velocity profiles perpendicular to the creeping section (Fig. 10(c),(g),(k),(o)), we can better understand the creeping rates and whether the fault is still partly locked (e.g., Hussain et al., 2016; Qiao and Zhou, 2021). The velocity profile across the North Anatolian creeping section shows that the tectonic loading rate (or the slip rate of the fault below the locking depth) on the fault is about 20 mm/yr, which is consistent with previous studies on this section (e.g., Jolivet et al., 2023). The localised offset on the fault (associated with shallow creep) is less than the tectonic loading rate, suggesting the fault is still partly locked, which is supported by previous studies (e.g., Hussain et al., 2016; Jolivet et al., 2023).

When compared with the North Anatolian creeping section, creep on the Chaman fault is much more evident with a larger spatial extent along the fault (Fig. 10(e)). Our east velocity profile across 31.7°N (Fig. 10(g)) shows that the east component of the tectonic loading rate is about 3 mm/yr, from which we can estimate a fault-parallel loading rate of ∼ 7 mm/yr based on a strike of N25°E, consistent with the 6.6 ± 1.2 mm/yr estimated by Fattahi and Amelung (2016) and 7 ± 2 mm/yr from Dalaison et al. (2021).

Compared with other creeping faults, the spatial extent of the creeping section on the Haiyuan fault in northeastern Tibet is much smaller (Fig. 10(i)). As the strike of the Haiyuan fault is nearly east-west, our velocity profile indicates that the overall tectonic rates of the Haiyuan fault should be near 4 mm/yr, which is consistent with previous studies (Huang et al., 2022). The velocity offset immediately across the fault suggests a creep rate that is slightly smaller than the loading rate in the location of our profile, suggesting a creep rate of ∼ 3 mm/yr, similar to Jolivet et al. (2023).

The Xianshuihe fault in Eastern Tibet also shows a clear step in the east velocity field (Fig. 10(m)) and high maximum shear strain rates between 30°N and 32°N. The east velocity profiles indicate a loading rate of ∼ 12 mm/yr, assuming a strike of ∼60°, which is close to the 11.5 ± 1.5 mm/yr estimated by Qiao and Zhou (2021). The offset in the east velocity appears comparable with the far-field loading rate in our data indicating that the fault is fully creeping.

Our InSAR time series over the Alpine-Himalayan Belt not only provides a way to study the rate of creep but also allows for the investigation of its potential temporal variations. Fig. 10(q) shows a displacement time series for the Chaman Fault for a pixel referenced to another pixel on the other side of the fault (two red points in Fig. 10(e)); because the points are close to the fault, the displacement time series captures how the creep rate is changing temporally. The example time series suggests that creeping on the Chaman Fault is fairly steady in time (∼ 3.8 mm/yr), with any variations from steady-state hard to distinguish from noise.

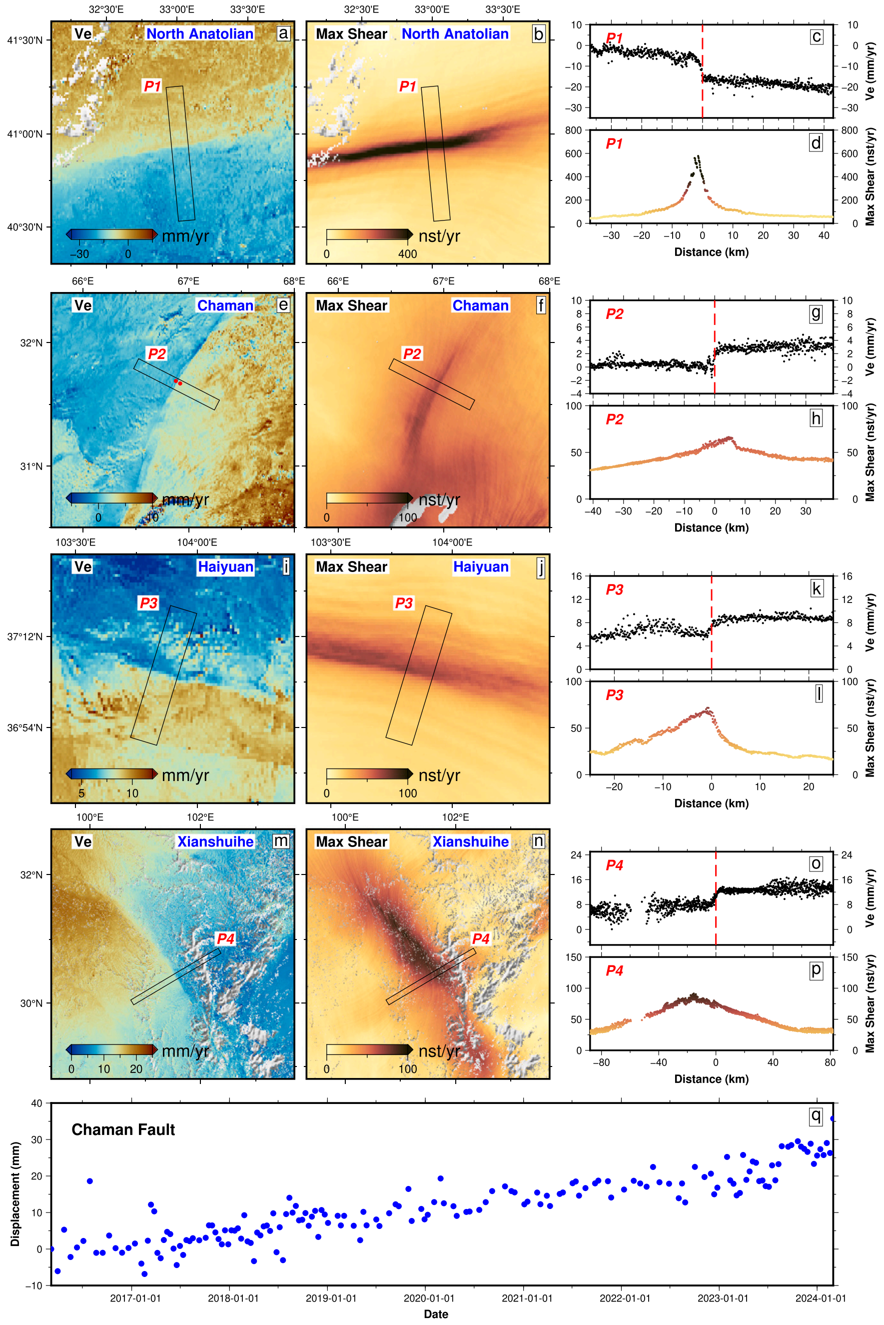

Fig. 10. Examples of creeping fault signals observed in timeseries. Location of regions shown in Figure SB16. (a,e,i,m) East velocities around the North Anatolian fault, the Chaman fault, the Haiyuan fault and the Xianshuihe fault. (b,f,j,n) Maximum shear strain rates around these active faults. (c,d,g,h,k,l,o,p) The velocity and maximum shear strain rate profiles across these faults. The location of the profiles are shown in the left two columns. The width of the profiles are all 10 km. (q) A displacement time series of a pixel (referenced to a pixel at the other side of the fault) based on LiCS frame 042A_05933_131313, and the location of these two pixels are shown by red points in (e). (For interpretation of the references to colour in this figure legend, the reader is referred to the web version of this article.)

Although a systematic study of creeping faults is beyond the scope of this paper, our results have shown that our derived velocity field and time series can be used for further investigation and comparison of creeping faults within the Alpine-Himalayan Belt. Nevertheless, we can conclude that creep is relatively rare on continental faults.

5.3.2. Postseismic deformation

During our InSAR data processing, we removed the impact of the coseismic signals that occurred during the acquisition timeframe by adding gaps or truncating the data (Table SA4). However, we did not attempt to correct for postseismic deformation resulting from earthquakes that occurred before the Sentinel-1 observation period nor which occurred within the observation window (although we did truncate time series before some earthquakes that occurred late in the observation window; Table SA4). Some significant postseismic deformation signals are present in our velocity and strain rate data (Fig. 11).

Postseismic deformation has been attributed to three primary processes: viscoelastic relaxation, poroelastic rebound, and afterslip (e.g., Ryder et al., 2007, 2011; Wright et al., 2013; McCormack et al., 2020; Zhao et al., 2021). Mapping how deformation varies in space and time

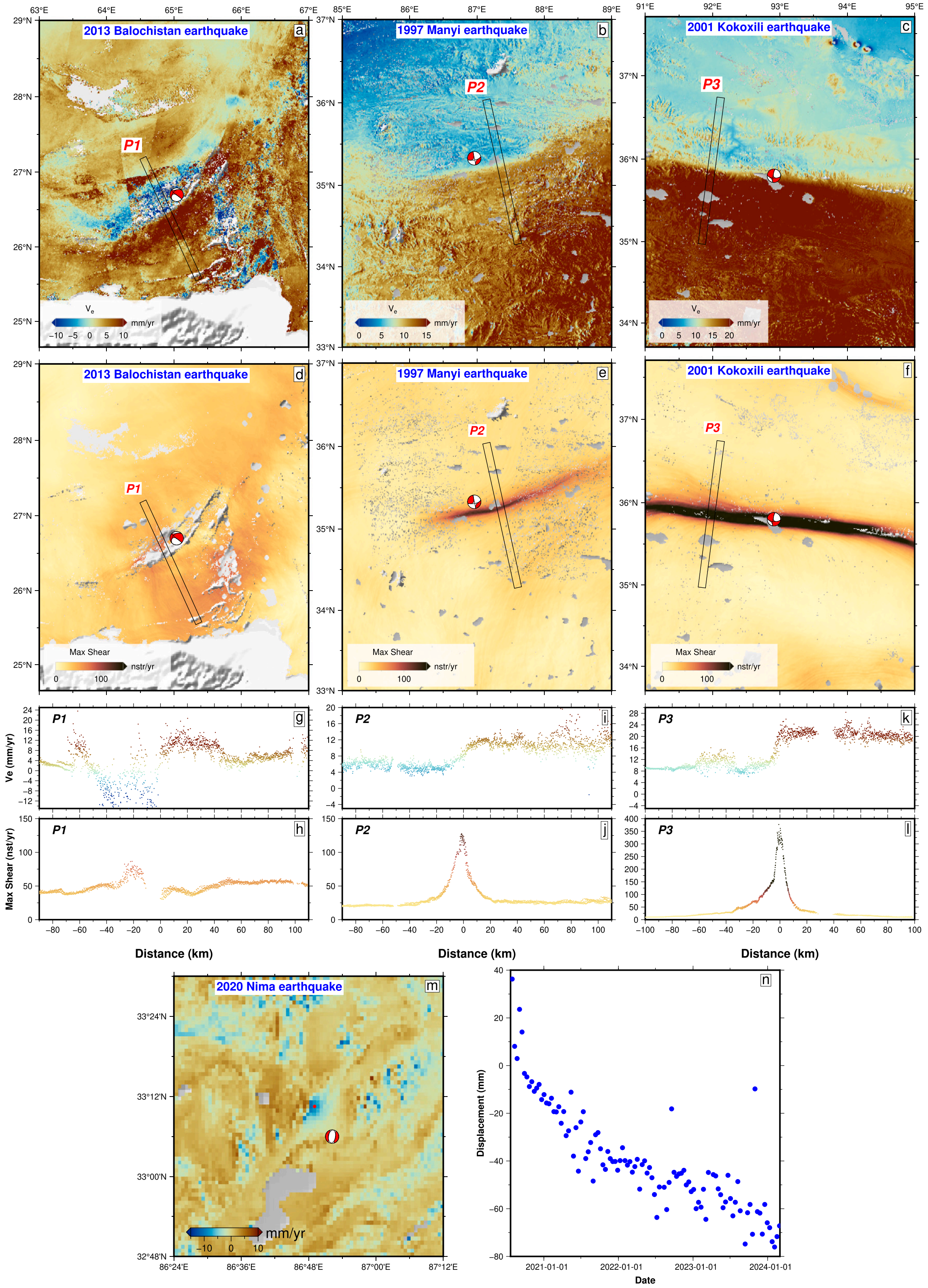

Fig. 11. Examples of postseismic signals observed in timeseries. Location of regions shown in Figure SB16. (a,b,c) East velocities around the epicenter of the 2013 M_w 7.7 Balochistan earthquake, the 1997 M_w 7.5 Manyi Earthquake and the 2001 M_w 7.8 Kokoxili Earthquake. (d,e,f) Maximum shear strain rates around the epicenter of these earthquakes. (g–l) East velocity and maximum shear strain rate profiles across the postseismic deformation zones. The locations of the profiles are shown in (a–f). (m) LOS velocities around the 2020 Nima earthquake in the LiCS frame 012A_05642_131313. (n) The postseismic LOS displacement time series for the 2020 Nima earthquake based on the LiCS frame 012A_05642_131313. The location of the pixel is shown by red point in (m). The red focal mechanisms for the earthquakes in (a–f) and (m) are from Global Centroid Moment Tensor Catalog (Dziewonski et al., 1981; Ekström et al., 2012). (For interpretation of the references to colour in this figure legend, the reader is referred to the web version of this article.)

following large earthquakes provides an opportunity for understanding the relative contributions of these mechanisms, and can act as a probe to determine lithospheric rheology and investigate the friction properties of faults (e.g., Barbot et al., 2009; Wright, 2016; Ingleby and Wright, 2017; Weiss et al., 2019). Ultimately, understanding postseismic deformation is required if we are to use short-term geodetic data to say anything meaningful about long-term hazard. Due to the variation in earthquake size, earthquake type, and structure of the Earth, the surface deformation pattern of the postseismic phase and its duration can vary significantly between events, although the largest velocities typically decay following a $1/t$ law (Ingleby and Wright, 2017).

Fig. 11 shows several examples of signals due to postseismic deformation that we observe in our velocity field. From Fig. 11(a) we can see that there is measurable and distributed postseismic deformation due to the 2013 M_w 7.7 Balochistan earthquake (Avouac et al., 2014) during our acquisition time (2016–2024). Previous research showed that the earthquake had a large strike-slip component (Avouac et al., 2014), which is consistent with the ~ 20 mm/yr offset we observe in the east velocity field (Fig. 11(g)). The elevated shear strain rate of over 75 nst/yr around the fault (Fig. 11(h)) suggests that the postseismic deformation on this fault is still dominated by strike-slip movement. The postseismic deformation associated with this fault is thought to be controlled mainly by widespread aseismic slip rather than viscoelastic relaxation (Lv et al., 2022), which is consistent with the deformation pattern we observed.

The 1997 M_w 7.5 Manyi earthquake was two to three decades before this dataset coverage, but the postseismic deformation related to it is still notable in the velocity field (Fig. 11(b)). Previous studies based on the InSAR time series just after the earthquake suggest that both afterslip and viscoelastic relaxation can be plausible mechanisms for the postseismic deformation related to this earthquake (Ryder et al., 2007). Our velocity fields suggest the postseismic deformation related to this earthquake does not completely vanish even decades later. We consider the ~ 7 mm/yr sharp step in the east velocity field (Fig. 11(i) to include postseismic deformation rather than being purely interseismic based on a previous study that shows the relative motion accommodated on this fault is only 3 ± 2 mm/yr before the earthquake (Bell et al., 2011).

Postseismic deformation related to the 2001 M_w 7.8 Kokoxili Earthquake is also particularly obvious and pronounced in our velocity field (Fig. 11(c)). This earthquake occurred on the Kunlun fault, and its postseismic deformation generates high maximum shear strain rates of over 150 nst/yr along the fault (Fig. 11(f),(l)). Previous studies suggest the possible mechanism for the postseismic deformation of this earthquake to be viscoelastic relaxation and afterslip (e.g., Ryder et al., 2011; Wen et al., 2012), but separation of these two contributing sources is not well resolved. Moreover, the viscoelastic parameters for the deep crust given from previous studies show large variation (Lv and Shao, 2022). This variation not only comes from different models used in these studies, but also lies in the uncertainties and limitations of the observations themselves. Our derived velocity field, strain rates and time series can provide more constraints on such parameters in future studies.

Postseismic deformation of moderate earthquakes can also sometimes cause deformation that is observable in our velocity field, especially in the line-of-sight velocity results. Fig. 11(m) shows the impact of the postseismic deformation of the 2020 M_w 6.3 Nima Earthquake (Hong et al., 2023) on our line-of-sight velocities. From the time series, the temporal decay in postseismic velocity is clear (Fig. 11(n)).

We chose not to attempt to correct for postseismic signals to obtain “steady-state” velocities, as is often done during GNSS processing (Herring et al., 2016). However, a challenge is knowing what postseismic mechanism to correct for and which earthquakes to include, as we clearly document deformation from events such as the Manyi earthquake, which occurred 30 years prior to the end of our data coverage (Fig. 11(i). By not correcting for the postseismic signals we see in our data, we provide an opportunity for the community to use the deformation data to build improved models for the events we observe, rather than applying our prejudices on the functional form for the time series corrections.

5.3.3. Non-tectonic vertical signals

Sources that contribute to current measurements of vertical motions include those of tectonic, hydrologic, anthropogenic, and cryospheric signals. Those that are tectonic are associated with mapped active faults and the locations of recent earthquakes. Cryospheric signals are associate with glaciated areas and can be hard to separate out from tectonic uplift in these mountainous regions. However, the bulk of the significant vertical rates we are imaging are land subsidence, predominately due to water extraction.

In the vertical velocities, we observe non-tectonic deformation with distinct spatial patterns from tectonic deformation. For the most part, these incidences are large areas of rapid subsidence (faster than 10 mm/yr over areas larger than 4 km^2) located in valleys (Gambolati and Teatini, 2015; Herrera-García et al., 2021) associated with agriculture.

We observe this land surface subsidence in the Po Plain (Bonì et al., 2017), Po Delta (Da Lio and Tosi, 2019), and Tavoliere delle Puglie (Scardino et al., 2022) regions of Italy; several regions of Western and Central Türkiye (including the Konya Basin and the Küçük Menderes River Basin, Üstün et al., 2015; Yalvaç et al., 2023); Georgia and Azerbaijan; extensively across Iran (Motagh et al., 2008; Goorabi et al., 2020; Mirzadeh et al., 2021; Haghshenas Haghighi and Motagh, 2024); Afghanistan (Meldebekova et al., 2020; Kakar et al., 2025); Pakistan (Khan et al., 2022; Ahmad et al., 2019); and in the Junggar Basin (Wang et al., 2022a) and Beijing regions of China (Zhu et al., 2015; Hu et al., 2019; Chen et al., 2016; Ao et al., 2024).

Previous work has observed the correlation of subsidence rates in the Alpine Himalayan Belt with groundwater depletion, particularly across Iran (Motagh et al., 2008); Kabul, Afghanistan (Meldebekova et al., 2020; Kakar et al., 2025); and Beijing (Chen et al., 2016). However, more recent work derives a more complex picture of land subsidence across, for example, China (Ao et al., 2024), where the mass of cities, groundwater depletion, and hydrocarbon extraction all contribute to rapid land surface subsidence.

In this study, we find over ~227,000 km^2 is subsiding faster than 10 mm/yr in regions larger than 4 km^2. We choose this area threshold to discount isolated, noisy pixels. We choose this velocity threshold to discount apparently slowly subsiding regions which may instead represent non-deforming noise sources including phase bias (e.g., Ansari et al., 2021; Maghsoudi et al., 2022). Including the whole AHB, the largest region of continuous subsidence is in Eastern China, covering ~51,000 km^2 (Fig. 12(b)). This region stretches from Beijing in the north, south through Tianjin, finishing in Puyang (Fig. 12(b)). This region alone is similar to or larger than the total extent of land subsidence across the whole of Iran (Haghshenas Haghighi and Motagh, 2024; Payne et al., 2025). In northern China, there is a vast region of subsidence in the Junggar Basin, north of the Tian Shan, covering ~13,000 km^2 (Fig. 12(a)). This figure is similar to the 16,146 km^2 subsidence extent for this region reported by Wang et al. (2022a). Across the whole Tian Shan region, rapid subsidence covers ~18,000 km^2. Other subsidence regions of significant geographic extent include two regions around the Konya Basin, Türkiye, which total ~7000 km^2 in extent (Fig. 12(c)).

We find a total area of ~1800 km^2 in which subsidence exceeds 100 mm/yr. The vast majority of these rapidly subsiding regions are located in Iran (1580 km^2, 88.5 %), but also in Türkiye (123 km^2; near Ödemiş and in the Konya Basin), Pakistan (63 km^2; near Qila Saifullah and Quetta), western Azerbaijan (5 km^2), and in small areas of the Tian Shan (12 km^2).

For analysis of rapid subsidence in Eastern China (longitudes > 111°E), there are limited Sentinel-1 acquisitions in the descending direction, meaning velocity decomposition to retrieve vertical surface motion

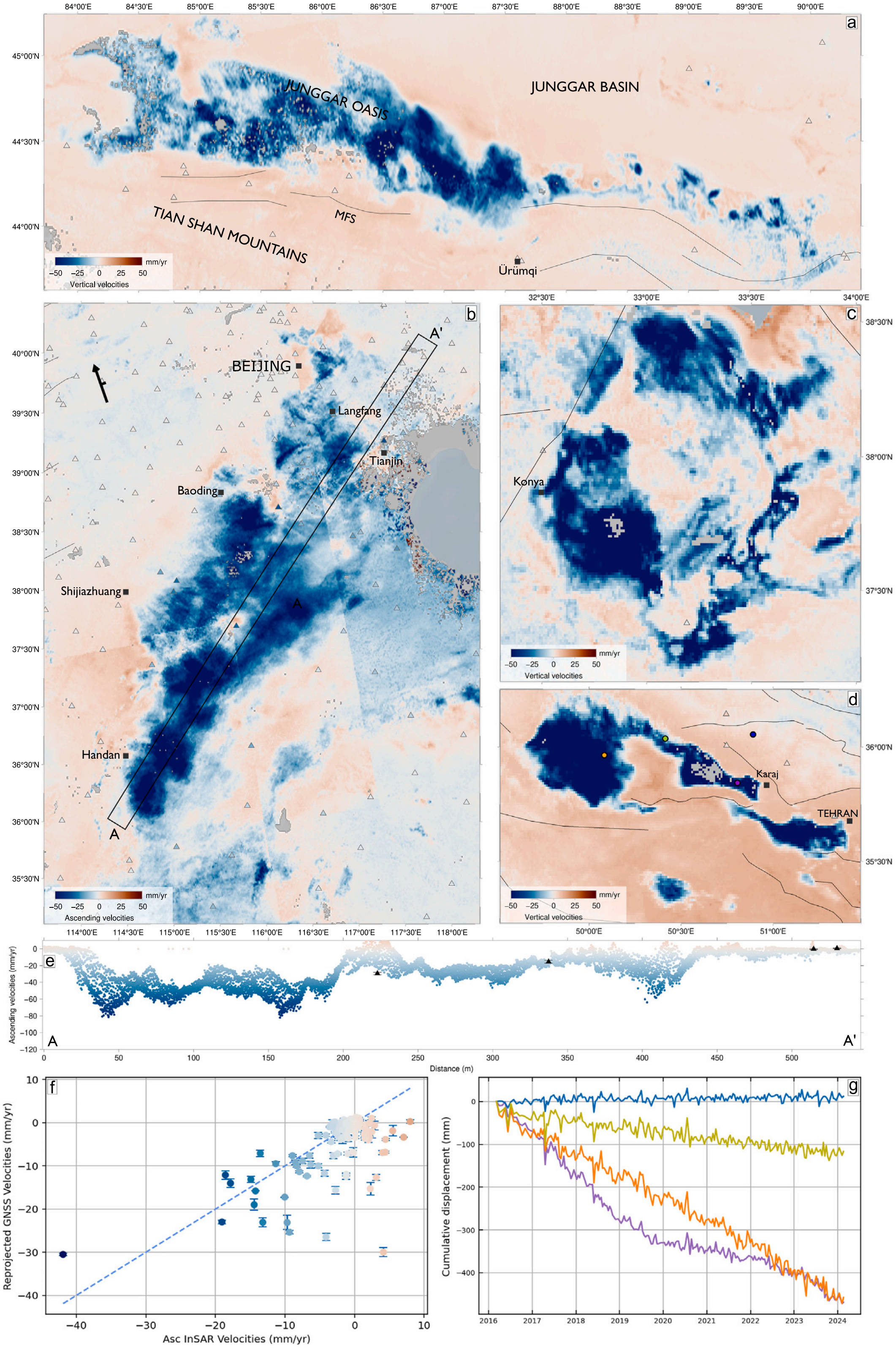

Fig. 12. Case examples of rapid vertical subsidence signals associated (according to previous literature or hypothesised association) with groundwater depletion. Location of regions shown in Figure SB16. (a) Tianshan North Slope, China (Yi et al., 2025). (b) The largest continuous subsidence region in this study in Eastern China. Profiled velocities A–A' are in e) (e.g., Ao et al., 2024). (c) Konya Basin, Türkiye (e.g., Üstün et al., 2015). (d) Rapid subsidence near Tehran and Karaj in northern Iran (Haghshenas Haghighi and Motagh, 2024; Payne et al., 2025). (e) Ascending velocities in swath A–A' in b), Eastern China. Triangles = 3D GNSS, circles = 2D GNSS (both this study). (f) Comparison of ascending InSAR velocities from b) at locations of GNSS sites to GNSS velocities reprojected into Sentinel-1 ascending line-of-sight direction. (g) Line-of-sight cumulative displacement time series in the descending direction for frame 035D_05397_131013 at locations in d). Faults from (Styron and Pagani, 2020).

is not possible through our methodology across large sections of the main subsidence regions here (Figs. 6 and 7). Instead, we use only ascending acquisitions and resulting surface velocities in the ascending direction to estimate that ∼100 km^2 is subsiding faster than 10 mm/yr in Eastern China. We therefore assume for this geographic region that 100 % of the recorded ascending direction is vertical. We reproject our GNSS data (Fig. 3) in this region into the ascending direction to compare to these ascending InSAR velocities (Fig. 12(b),(e)). We find reasonable agreement between these velocities ($r^2 = 0.63$), with the strongest disagreement between rapidly subsiding GNSS stations (20–30 mm/yr) and more apparently stable InSAR velocities. This discrepancy may be due to the GNSS instruments that recorded these more rapid velocities being mounted on monuments, for example, buildings, that are subsiding rapidly on a local spatial extent. Conversely, these InSAR results are posted to 1 km pixel widths, thus averaging to some extent deformation in the ascending direction across the pixel. Consequently, rapid subsidence of individual buildings or monuments would not be visible in our InSAR velocities. This discrepancy is additionally highlighted by uncertainties in both GNSS and InSAR velocities. For example, the GNSS site in Fig. 12(e) at around 225 m along the profile has large uncertainties (±10 mm/yr). The spatial pattern of displacement varies significantly within this subsidence region, with the pattern of subsidence appearing like smaller, joined-up subsidence bowls (Fig. 12(b), (e)). This pattern suggests that perhaps the depth of aquifer sediments controls subsidence magnitude. Previously, more local work in this region does find that faulting has some control on the subsidence pattern in Beijing (Hu et al., 2019), but future work should investigate these spatial controls on a more regional scale.

Away from Beijing, the largest region of subsidence in the AHB is in the southern Junggar Basin – the Junggar Oasis – in China (Fig. 12(a)). Previous work attributes this subsidence to over-exploitation of groundwater in this arid/semi-arid agricultural region (Wang et al., 2022a). Our results suggest maximum rates of subsidence in this oasis region reach ∼100 mm/yr, comparable to maximum rates estimated by Wang et al. (2022a) using Sentinel-1 over 2015–2020. In terms of spatial structure, the subsidence in this region appears to be bounded along part of its southern margin by the Manasi Fault system (Li et al., 2021b). Similar to the subsidence region south of Beijing, subsidence here is apparent as several smaller, joined-up subsidence bowls, perhaps suggesting a sedimentological rather than structural control on subsidence rate.

Land subsidence in Iran has been investigated thoroughly in previous work (Haghshenas Haghighi and Motagh, 2024; Payne et al., 2025), with the spatial pattern of several subsidence regions controlled by bedrock faults. However, there is a great need to investigate more thoroughly land subsidence drivers and controls on spatial patterns of subsidence in these other critical regions of the Alpine-Himalayan Belt.

On a larger scale, another process that induces land surface subsidence is the thawing of permafrost under a warming climate. Comparing the spatial patterns of our vertical velocities and the model prediction of permafrost presence (Fig. 13) reveals a spatial correlation between subsidence and regions with permafrost zonation index (PZI) greater than 0.5, indicating a high likelihood of permafrost presence (Gruber, 2012). In particular, the correlation is best observed in the Qilian Shan and the interior of the Tibetan Plateau, across almost the entire Qiangtang region, consistent with the result of Lemrabet et al. (2023).

At least 5 mm/yr of subsidence is measured across most of the permafrost zone, as averaged over 40 km wide profiles A–A’ and B–B’. Up to 10 mm/yr of subsidence rates are measured on the low-relief valley slopes of the Qilian Shan, similar to results obtained by Daout et al. (2021). Up to 20 mm/yr of subsidence is captured within the Kokoxili region in the central Tibetan Plateau, consistent with values of Chen et al. (2022); Wang et al. (2022c); Lu et al. (2023). This is also where the permafrost zonation index indicates a transition from PZI = 1 in northern Qiangtang, where permafrost presence occurs under all conditions, to PZI<0.5 in the southern Tibetan Plateau, where permafrost is only expected under very favorable conditions. We observe this characteristic across the whole region, where permafrost at the border of stability is the most susceptible to thawing and inducing the fastest subsidence. The co-location of sharp transitions in vertical velocity, topography, and permafrost zonation index at ∼300 km on Profile B–B’ (Fig. 13) is the best testament of this effect.

Our subsidence rates might be susceptible to the potential of underestimation due to unwrapping errors in long-temporal-baseline interferograms from C-band InSAR (Fan et al., 2025) and the potential of overestimation from phase biases due to multi-looking of especially in short-temporal-baseline interferograms (Ansari et al., 2021). Despite uncertainties in the absolute subsidence rates measured by InSAR (Liu et al., 2025), we reveal a big picture of subsidence patterns over the most extensive high-altitude permafrost zone on Earth, highlighting the value of InSAR in improving our understanding of high-mountain permafrost dynamics.

We have not tried to distinguish the vertical rates associated with the ice unloading due to mass loss of glaciers in the Himalayas and the Tian Shan for instance. The rates would contribute to the overall tectonic uplift from crustal shortening (as observed elsewhere in InSAR results for example in New Zealand (Liu et al., 2024; McGrath et al., 2025)), but the noise in our vertical signals make it difficult currently to separate out the two relative contributions. In-depth analysis and modelling is required to separate out Glacial Isostatic Adjustment (GIA) contributions and the impacts of hydrology to the vertical signal we measure.

Other interesting signals in the vertical velocity field include subsidence around the Siling Co and Longyangxia Reservoir, uplift on the Qarhan (Chaerhan) Playa in the Qaidam Basin and on various salt plains along the Hexi Corridor (northeast of Qilian Shan) and around the Tarim Basin, as well as localised subsidence on farmlands and mining and gas extraction sites (Fig. 13).

6. Discussion

6.1. Validation of velocity & strain rate fields

The European Ground Motion Service (EGMS) provides detailed geodetic measurements across Europe and surrounding regions at a resolution of 100 m derived by tying PS InSAR results to a GNSS reference frame (Costantini et al., 2021). Both EGMS and our InSAR show similar eastward velocity patterns (Figure SB30), which is not a surprise given that both are tied to GNSS. Most of Europe exhibits stable velocities with deformation rates of less than ±2 mm/yr. However, in regions like Greece and Anatolia, a significant westward motion is observed at a rate of approximately 20 mm/yr. A comparison between EGMS velocities and our GNSS compilation (Fig. 3) shows an RMS of 1.1 mm/yr for the eastward velocity and 1.5 mm/yr for the vertical velocity (Figure SB31). When comparing our InSAR-derived velocities with GNSS data in the European region, the RMS values are higher, with 2.5 mm/yr for eastward velocity and 3.3 mm/yr for vertical velocity (Figure SB24). Further work on some of our line-of-sight velocities should improve our noise levels, but some of this difference likely also reflects the difference in spatial resolution of the two processing strategies. We also note, however, that the EGMS time series can be misleading in terms of earthquakes – these create displacement steps in the EGMS time series that are then heavily smoothed, creating the dangerous false impression of pre-cursory deformation anomalies.

The Global Strain Rate Model (GSRM v.2.1) by Kreemer et al. (2014) and our GNSS-derived strain rates generally depict the same broad deformation patterns, with strain distributed over larger areas (Fig. 9, SB28, SB29 and SB32). In regions with relatively sparse GNSS measurements, such as the Makran and Sulaiman Ranges, Pamirs, and major strike-slip faults of Tibet (Fig. 3), the GNSS-derived strain rate models appear patchy and blurred due to limited data resolution, leading to less precise shear strain rate estimations and reduced clarity in deformation patterns. In contrast, our InSAR-resolution velocities provide higher spatial

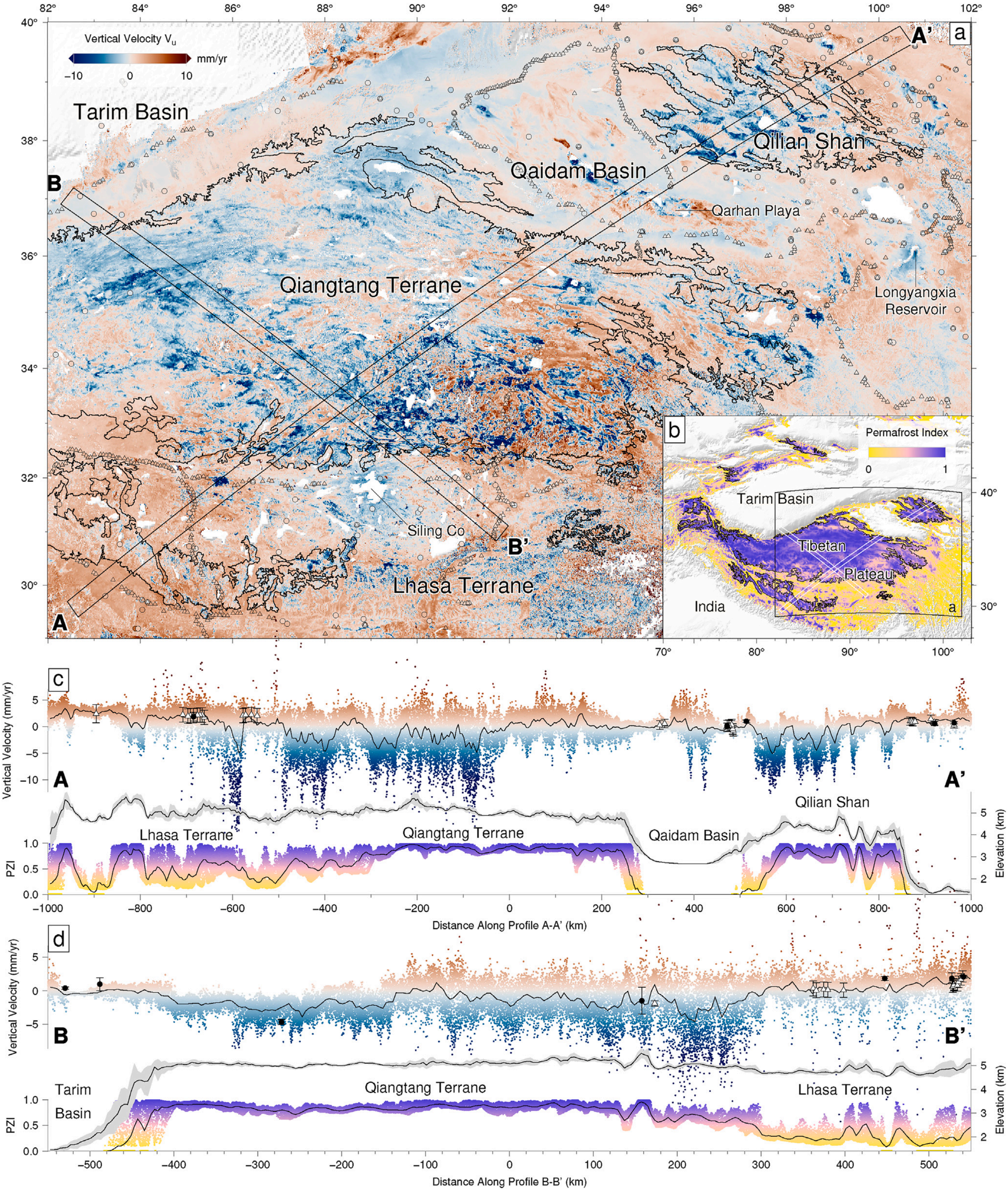

Fig. 13. (a) Vertical velocity field with 3D GNSS stations shown in circles, levelling measurements in triangles, and contour line representing Permafrost Zonation Index of 0.5, above which there is a high likelihood of permafrost presence (Gruber, 2012). (b) Permafrost Zonation Index from Gruber (2012) with contours and profiles as in (a). (c,d) Profiles of vertical velocity, the Permafrost Zonation Index and topography. 3D GNSS and levelling vertical velocity measurements are shown as black circles and white triangles with error bars. (For interpretation of the references to colour in this figure legend, the reader is referred to the web version of this article.)

resolution, localizing more strain onto these structures and capturing finer-scale variations. It is also important to note, however, that our InSAR results also include contributions from postseismic deformation following major earthquakes (Section 5.3.2; Figure SB32).

The GNSS-derived dilatation rate field exhibits smoother and more consistent trends. In contrast, extracting a clean dilatation field from InSAR is more challenging, as it often contains short-wavelength noise. Despite these differences, all models capture similar large-scale deformation patterns, including extension in Italy, Greece, western Türkiye, and central Tibet, and contraction across the Caucasus, Zagros Mountains, Makran, Sulaiman Ranges, Pamirs, Tian Shan, Himalayas, and Qilian Shan.

6.2. Sources of deformation

By observing continental deformation at relatively high spatial resolution at a trans-continental scale, our work reveals important insights into the variety of deformation styles that we see in the continents. Broadly speaking, our work confirms the emerging view that continental deformation occurs in two modes – strain is focused around major fault structures but is more distributed elsewhere (e.g., Wang and Barbot, 2023; Fang et al., 2024a,b). We see this most clearly by contrasting the elevated shear strains we observe around major strike-slip faults in Anatolia (Figure S1) and Tibet (Figures S6 & S7) with the more diffuse shear across regions such as the Iranian Plateau (Figure S2). Because we have uniform InSAR coverage across the entire region, this contrast in deformation style is much clearer than in the previous best strain map on this scale, the Global Strain Rate Model (Figure SB28). We see that the locations of past seismicity from the ISC-GEM catalogue of earthquakes (Storchak et al., 2013, 2015; Di Giacomo et al., 2018) aligns well with our strain rate field (Fig. 14). Regions of current (120 year) aseismicity, such as northern Afghanistan and Turkmenistan, northern Arabia and north of the Tian Shan align with regions of very low strain rates in our data. Regions of notable high strain without recent seismicity are the northern Chaman Fault Zone up to the Eastern Syntaxis, and the Altyn Tagh Fault in northern Tibet. Zones of more distributed deformation across the Tian Shan and Makran have perhaps less recent seismicity than we might expect. Whilst the regions of concentrated strain have previously identified faults along them, many regions with active faults already mapped do not have significant strain rates across them in our results (Fig. 14). This highlights the need to consider seismic potential even in relatively low straining areas.

It is clear that some of the focused strain we see today is long-lived postseismic deformation from past earthquakes (Section 5.3.2), which would need to be taken into account in any assessment of interseismic deformation. This transient deformation can last decades - for example, we still see elevated postseismic strain rates on the Manyi Fault in Tibet, which ruptured in 1997. However, it is worth noting that major faults such as the Altyn Tagh Fault, which have experienced long periods without earthquakes, still exhibit significant strain concentrations. Hussain et al. (2018) showed that the strain rate on the North Anatolian Fault is independent of time since the last earthquake, once a decadal postseismic period has ended. Ingleby and Wright (2017) showed that postseismic transients are measurable for up to 100 years, and that the largest postseismic velocities decay following a $1/t$ law (where t is the time since the last earthquake). Our results support the conclusion that, at least for the majority of major faults, rapid postseismic strain-rate transients decay to a steady-state interseismic rate (Meade et al., 2013), rather than varying throughout the earthquake cycle (Wang et al., 2021). One potential exception is the Karakoram Fault in western Tibet – it remains unclear whether the lack of a strain concentration on this fault is due to the low slip rate (Wright et al., 2004a) or because it is late in the earthquake cycle.

The major faults where we see strain concentrations are those that have accrued large geologic displacements. One hypothesis is that repeated earthquakes and significant displacements facilitate strain localisation, through mechanisms such as shear heating, grain size reduction, fabric development, and fluid infiltration. To explain the geodetic observations on major faults requires a weak component of the system (a low viscosity zone or weak fault) capable of producing rapid postseismic transients; this must be embedded within a relatively stronger substrate (relaxation time equal to or larger than the inter-event time) in order to give focused interseismic strain (Yamasaki et al., 2014; Elliott et al., 2016; Wright, 2016). Fang et al. (2024a) estimate a depth-averaged viscosity of 10^{22} Pa s for the lithosphere away from Tibetan faults, which would be consistent with this model.

Accruing significant (10s km) long-term displacements is only possible for long faults that remain in a favourable orientation. They are likely to be weak structures that cross the entire lithosphere (Vauchez et al., 2012). Smaller faults may behave differently, perhaps responding more passively to the overall regional strains, as proposed by Bourne et al. (1998). The interseismic strains associated with slow/small faults are still challenging for satellite geodetic approaches, but we expect future improvements in viewing geometries and coherence (Section 6) to help address whether small faults behave differently to the major structures.

The geodetic data are also capable of observing shallow interseismic creep on some fault structures. This seems to be a relatively rare phenomenon – most faults in the continents are locked and capable of major earthquakes. Even for those faults that do exhibit shallow creep, most are creeping at rates significantly lower than the long-term fault slip rate. Aseismic shallow fault creep is not a significant mechanism for releasing elastic strain accumulation in continental interiors.

Geodetic data are now being increasingly used as inputs to seismic hazard models. One approach is to use the data to help constrain fault-based block models (e.g., Evans, 2022; Styron, 2022). In this approach, the "blocks" each behave as independent microplates; the continuous velocity fields we produce by combining GNSS and InSAR data ensure that there are sufficient data within each block to constrain the free parameters (coordinates of the pole of rotation and rotation rate). A major challenge with this approach is that each block has to be completely isolated by faults, even if such structures do not exist. Alternatively, Johnson et al. (2024) recently proposed a direct strain rate inversion approach; inverting strain rates directly removes the need to isolate "blocks" as the strain rates are independent of rotations. Fang et al. (2024b) showed that to match the observed strain in south-east Tibet required the addition of distributed strain sources, as strain on the mapped faults alone was insufficient. This approach relies on high-resolution strain rate data of the type we provide. Strain rate data can also be used directly to estimate moment deficit rates and hence seismicity rates (e.g., Bird et al., 2010, 2015). Our strain rates are significantly sharper than those derived from the Global Strain Rate Model and we would anticipate that they could be used to make a higher-resolution forecast of seismicity rates.

We note that deformation data are just one component of information required for managing and understanding seismic hazard and risk, alongside seismology, active fault mapping and geomorphology, historical earthquakes, and palaeoseismology (Abdrakhmatov et al., 2024). However, Earth observation data and satellite geodesy feed into many aspects of the Disaster Risk Management cycle (Figure SB33). The Continental Strain Rate Fields from InSAR combined with GNSS are now emerging as potentially useful inputs into the preparedness of regions before earthquakes by highlighting the regions straining and providing constraints on models of seismic hazard.

6.3. Challenges & future improvements

Working at such a large spatial scale and aiming for millimetre per year accuracy in surface velocities has a number of challenges. The atmospheric noise contributions can be modelled and corrected to a significant degree, and mitigated against through time series analysis to better estimate average velocities. However, there are still some residual effects that could be improved by better and/or higher resolution

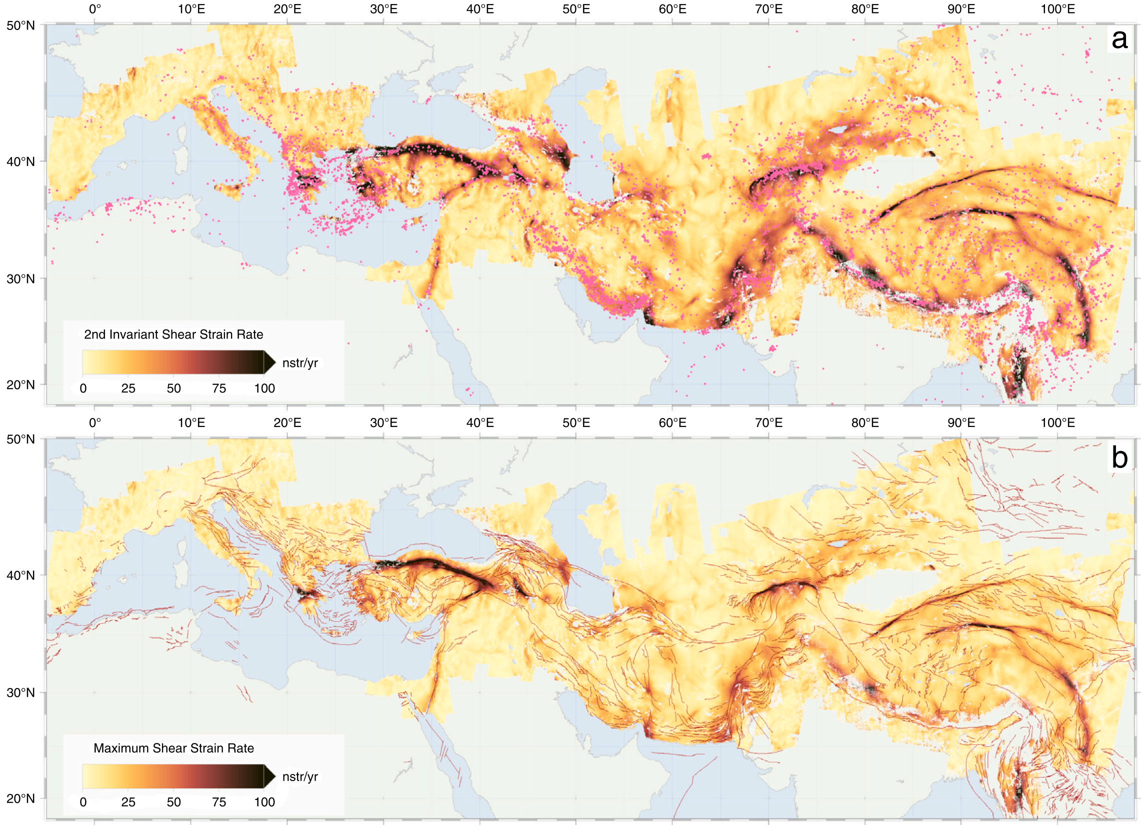

Fig. 14. (a) Earthquakes from the ISC-GEM catalogue (Storchak et al., 2013, 2015; Di Giacomo et al., 2018) in pink overlaid on the 2nd invariant of the strain rate tensor. The earthquakes are from 1904 onwards, and selected for magnitudes (M> 5) at shallow depths (< 35 km). (b) Major active faults (red) from Styron and Pagani (2020) overlaid on maximum shear strain rate. (For interpretation of the references to colour in this figure legend, the reader is referred to the web version of this article.)

tropospheric corrections (e.g., Yun et al., 2015), as the tropospheric correction does not always improve the noise in individual interferograms. Additional refinements to ionospheric corrections which take account of the seasonal and latitudinal variations in the vertical layering of the ionosphere would improve on our current simplifying assumption of a constant 85 % of the total electron content being below the satellite.

The use of InSAR to estimate velocities does introduce finer resolution than that derived from the GNSS in most regions, but it does also introduce noise at short wavelengths in some locations. The InSAR data add the most information in areas which are highly coherent and where there is little existing GNSS coverage, such as across Iran and Central Asia, and within the Tibetan plateau (Fig. 3). GNSS site velocities are typically more representative of the displacement of the Earth's surface as they are often anchored in bedrock; InSAR is susceptible to the effects of vegetation, loss of coherence (Figure SB9) and phase biases (Ansari et al., 2021), as well as measuring other at, or near, surface displacements not representative of the deeper crustal tectonic motions. Identification of more representative pixels in the InSAR-derived velocity fields will help reduce the noise (as well as using longer time series to better estimate average velocities). Additionally, it may be possible to roll out corrections for the phase bias from using short period interferograms from individual frames to the whole AHB scale (Maghsoudi et al., 2022). In most cases, however, non-tectonic deformation and phase bias map to the vertical component; horizontal velocities at large scale can only be caused by tectonics.

The short wavelength variability in the surface velocities makes estimation of strain rates challenging. As strain rates are gradients in the velocity, this exacerbates any noise present. This means we have necessarily smoothed our velocities prior to strain-rate calculation to average out some of this dispersion. Future methods could better adapt the filtering approach to account for levels of noise and thus capture the sharpness of velocity gradients expected. In addition, we do not have the north-south component of velocity in the InSAR, relying on the smoother GNSS-derived velocity field. This limitation could be improved in part by using the azimuth (predominantly north-south) motion from burst overlap interferometry (Li et al., 2021a). Of the various strain rates calculated, it has been particularly difficult to capture the dilatation rate sufficiently to make meaningful novel interpretations. This was also found using InSAR applied to the San Andreas Fault (Xu et al., 2021).

Our strain rates show that we are capturing the scars of old earthquakes in the postseismic deformation that is ongoing years and decades after these events. Whilst they are very much part of the velocity and strain rate field, we could choose to account for the postseismic contributions of earthquakes directly in velocity fields, as is done in the GNSS community (Herring et al., 2016; Sobrero et al., 2020), and separate their effects out from the even longer-term deformation. However, doing this in a systematic fashion without biasing the results by our prejudices is challenging – we have chosen to keep postseismic transients in our time series but provide the data that will allow others to make those corrections.

Whilst we are primarily concerned with capturing continental deformation at the scale of the whole AHB, the regions of greatest topography, in particular the Himalayas, are important as locations for major earthquakes. However, it has been very hard to reliably measure the velocities for the highest relief mountains of the Alps, Caucasus, and Himalayas with C-band SAR due to limited coherence at these wavelengths (Figure SB9). This is due to a mixture of environmental impacts including vegetation up to the tree line, and the impact of snow cover at high levels. There is also the challenge of the extreme overall relief, leading to layover and shadowing for radar viewing geometries, which is difficult for unwrapping phase; high relief also results in large gradients in tropospheric delays. It has also been challenging to capture deformation south of the Himalayas in northern India too due to extensive areas of agriculture, and vertical displacement signals due to groundwater extraction.

The Sentinel-1 satellite radar data were processed continuously during the life span of the LiCS research project (over a 10–year timespan), using the JASMIN high performance computing facility (this involved continued development of the workflow routines, testing and smaller regional studies prior to a unified large scale effort culminating in the past 3 years focus). The total number of epochs for all ascending and descending frames was about 222,000 dates, which approximated a similar number of SLC files each of about 4–7GB in size (total volume 1PB) needed for generating all 1.2 million interferograms. The processing steps generated intermediate files of even greater volume, and the process is disk storage limited (as we only have access to hundreds of TerraBytes of disk space for the processing storage). This lack of larger data storage meant it was necessary to 1) proceed on a frame-by-frame basis rather than in parallel, and 2) multilook our data and downsample to 100 m to store over one million interferograms. To perform our subsequent analysis, it was again necessary to further downsample our average velocities to 1 km to make the time series inversion with LiCSBAS perform in reasonable time frames. We estimate at least 5 core-hours of processing time were spent per each epoch used starting from the original Sentinel-1 SLC download until generation of the final time series, totalling at least 1 million core-hours for the whole processed dataset. For curation of the interferogram dataset, we use the storage at the UK's Centre for Environmental Data Analysis (CEDA) in their long-term tape archive.

We expect we can also make general improvements by 1) widening the coverage further across the wider AHB into slower deforming areas, 2) lengthening the time series with more recent data from after March 2024, and 3) producing time series at higher spatial resolution than the current 1 km. There is relatively easy potential for 100 m as our catalogue of interferograms has been produced at that resolution, just not the time series and subsequent analysis for this study. By opening up the data set to the community, we give others the opportunity to apply different processing and correction algorithms to our very large observational data set.

6.4. Recommendations

Our results here show that whilst there are concentrations of strain associated with major faults and past earthquakes, an important fraction of the continental deformation occurs over long distances in a smooth, distributed fashion resulting in small strain rates. Ongoing acquisitions to lengthen the Sentinel-1 time series using Sentinel-1 C and 1D will be crucial for lowering the threshold for capturing small strain. However, as highlighted with issues of maintaining coherence with C-band, it is important that there are no large data gaps in acquisitions as they break the time series, reducing the accuracy of the average velocities we derive.

Although we have benefited from an exceptionally large data set, some areas lack complete coverage in both ascending and descending viewing geometries, which prevents the retrieval of two components of the velocity field at InSAR resolution. We recommend that acquisitions in both look directions (i.e., including descending) are prioritised over eastern China around the Ordos. Additionally, the region that experienced amongst the largest continental earthquakes in the past century, the M8 Tsetserleg-Bulnay Strike-Slip Earthquake in 1905 in Mongolia (Choi et al., 2018), has a much less complete archive of data, and also should be targeted in the ongoing mission.

The open access data policy from the Copernicus ESA programme for Sentinels has not only been a great benefit in accomplishing a project at this scale, but a necessity. Systematic, regular acquisitions at broad scales are the only way to extract small strain rate signals over long wavelengths typical across the continents, and we recommend that such an approach be continued and adopted by other data providers.

6.5. Outlook for future satellite missions

The current Sentinel-1 mission is set to continue into the next decade (Miranda et al., 2023) with the recent successful launches of S1C and S1D. S1A will be deorbited once S1D becomes fully operational, but until that time, we anticipate the formation of interferograms between images acquired by S1A and S1C/D being possible, as has already been demonstrated (Figure SB34). The degradation of the S1A orbit will cause the two satellites to have larger baselines between them than is ideal for deformation measurements, leading to somewhat poorer coherence. Modelling of the degradation indicates that this will not become a significant issue before its end of life, although baselines of 700 m can be expected at higher latitudes (Pinheiro, 2024).

Over the next decade, several planned ESA missions will lead to improvements in our ability to measure tectonic strain over large areas. The next generation of Sentinel-1 satellites (Sentinel-1 NG) will also have a repeat interval of 12 days but a wider swath and higher duty cycle, meaning that each patch of ground can be imaged more frequently on average.

The Copernicus expansion mission Rose-L will operate at L-band (Davidson and Furnell, 2021; Petrolati et al., 2023) in the same orbit as Sentinel-1 NG, expanding coherent InSAR coverage in vegetated areas. The longer wavelength will also be advantageous for measuring high-magnitude signals during earthquakes, which may be aliased in Sentinel-1 data.

The joint NASA and ISRO NISAR mission (Kellogg et al., 2020) launched in mid-2025 and will also acquire L-band with global coverage (Rosen and Kumar, 2021). As well as offering increased coverage in vegetated areas, the left-looking geometry of NISAR will allow for 3-D decomposition when combined with Sentinel-1 data.

The 10th ESA Earth Explorer Mission, Harmony, will consist of two receive-only SAR systems operating in constellation with Sentinel-1D. When combined with the data from Sentinel-1, this will enable the retrieval of a full 3-D deformation field (Prats et al., 2023). As an Earth Explorer mission designed for scientific research rather than an operational mission, it will not be possible to measure 3-D data globally, but Harmony could serve as a proof of concept for future operational missions.

The continuation of Sentinel-1 and future missions will also offer the potential to generate very long time series, by combining data from ERS, ENVISAT, Sentinel-1, Sentinel-1NG, ROSE-L and other missions. This will allow measurement of processes that vary over the long term such as time-varying slip, as was demonstrated for the Haiyuan Fault by combining 20 years of ERS and ENVISAT data (Jolivet et al., 2013). Ice loss in permafrost across the northeastern Tibetan Plateau was measured over nearly two decades from combining ENVISAT and Sentinel-1 (Daout et al., 2020). Subsidence and uplift due to water extraction/replenishment in the Beijing Plain was measured spanning three decades from 1992 to 2023 by combining data from ERS, ENVISAT, Radarsat-2 and Sentinel-1 (Fu et al., 2025). The ability to measure changes in the Earth's surface environment over wide areas for decadal timescales will offer new insights into crustal and land surface processes.

7. Conclusion and outlook

We have compiled, aligned and quality controlled over 73,000 GNSS velocities collated from 171 recent studies into a Eurasia-fixed reference frame yielding over 21,000 consistent point velocities. We have produced the first transcontinental velocity and strain rate field for the Alpine Himalayan belt (20 million km^2), at a spatial sampling of 1 km and with levels of uncertainties in the horizontal ~2–3 mm/yr and we are able to measure strain rates down to $\sim$ 10 nstr/yr, or better in some very coherent regions. We have achieved this by processing large volumes of Sentinel-1 data (222,000 epochs), applying a number of atmospheric corrections to reduce noise and combining it with the GNSS reference velocity field.

We have found that horizontal velocities are dominated by tectonic processes. Our results show that whilst the horizontal strain rates are concentrated on major strike-slip faults of Anatolia and the Tibetan Plateau and major convergence zones of the Himalayas and Pamirs, the bulk of the Alpine Himalayan orogeny is undergoing diffuse deformation at relatively low strain rates. Significant regions of distributed deformation are found across Western Anatolia, Iran, the Makran, the whole of the Tian Shan and all of the Tibetan Plateau. We observe large-scale anticlockwise rotations of northern Arabia and Anatolia, as well as along the Chaman Fault zone from the Makran through to the Hindu Kush and Eastern Syntaxis. We observe major broad clockwise rotations around the Western Syntaxis of the Himalayas. Regions of elevated strain are also found to be associated with creeping faults and postseismic deformation from recent major earthquakes. The results agree well with previously derived strain rate fields with GNSS only, but the InSAR provides greater detail on short wavelengths for regions that lack very high densities of GNSS.

We find that the vertical rates are dominated by near-surface processes such as ground subsidence due to water extraction from aquifers, and permafrost changes at high elevations, except in regions of rapid convergence such as the Pamirs and Himalayas where we observe tectonic uplift.

Improvements we can look forward to include, in the short term, lower uncertainties from increased data with the growing archive with Sentinel-1 C/D, and higher-resolution time-series processing better than the 1 km provided here. In the medium term, better coverage from recently launched L-Band missions, will enable strain to be measured in areas with denser vegetation and higher relief, such as the Himalayas. NISAR's left-looking instrument, combined with the right-looking Sentinel-1, will provide some ability to recover full 3-component velocities.

Finally, one hundred years after Argand (1922)'s observations and tectonic map of the deformation of Eurasia, we look forward to the community developing, testing and applying new and improved algorithms to our open access data, and to the resulting improved understanding of continental tectonics.

CRediT authorship contribution statement

J.R. Elliott: Writing – review & editing, Writing – original draft, Visualization, Validation, Supervision, Resources, Project administration, Funding acquisition, Data curation, Conceptualization. **J. Fang:** Writing – original draft, Visualization, Validation, Methodology, Investigation, Formal analysis, Data curation. **M. Lazecký:** Writing – original draft, Visualization, Validation, Software, Methodology, Investigation, Formal analysis, Data curation. **Y. Maghsoudi:** Writing – original draft, Visualization, Validation, Investigation, Formal analysis, Data curation. **Q. Ou:** Writing – original draft, Visualization, Investigation, Formal analysis, Data curation. **J.A. Payne:** Writing – original draft, Visualization, Investigation, Formal analysis, Data curation. **C. Rollins:** Writing – original draft, Visualization, Validation, Methodology, Investigation, Formal analysis, Data curation. **D. Wang:** Writing – original draft, Visualization, Validation, Investigation, Formal analysis, Data curation. **A. Hooper:** Writing – review & editing, Supervision, Resources, Project administration, Funding acquisition, Conceptualization. **T. J. Wright:** Writing – review & editing, Supervision, Resources, Project administration, Funding acquisition, Conceptualization.

Declaration of generative AI and AI-assisted technologies in the writing process

During the preparation of this work, the authors used ChatGPT for checking of grammar and for coding some algorithms. After using this tool, we reviewed and edited the content and take full responsibility for the content of the publication.

Funding information

Research of this scale and scope would not have been possible without the systematic acquisitions and openness of the Sentinel-1 Archive by the ESA Copernicus Programme, for which we are very grateful. We also acknowledge that the compilation of over 170 GNSS studies to form the velocity field here is only possible by the openness of that community to tabulate and share their velocities. This research is supported by the UK Research and Innovation (UKRI) Natural Environment Research Council (NERC) through the Centre for the Observation and Modelling of Earthquakes, Volcanoes and Tectonics (COMET, http://comet.nerc.ac.uk). This work is also supported by NERC through the Looking into the Continents from Space (LiCS) large grant (NE/K010867/1). JRE acknowledges the Royal Society for their support through a University Research Fellowship (URF/R/211006 & UF150282) and grant (RF/ERE/210143). We acknowledge additional support from the European Plate Observing System (EPOS, https://www.epos-eu.org/). Some of the figures were generated using GMT versions 5 & 6 (Wessel et al., 2019) and pyGMT (Tian et al., 2025). Scientific colourmaps are from Crameri et al. (2020).

Declaration of competing interest

The authors declare the following financial interests/personal relationships which may be considered as potential competing interests:

John Elliott, Tim Wright, and Andy Hooper report financial support was provided by UK Research and Innovation. John Elliott reports financial support was provided by The Royal Society. If there are other authors, they declare that they have no known competing financial interests or personal relationships that could have appeared to influence the work reported in this paper.

Acknowledgement

We gratefully acknowledge Barry Parsons for his early conceptualisation and leadership of the LiCS project. Barry's inspiration of the project and his motivation throughout have been important in fostering our community. We also thank Greg Houseman and Philip England for their discussions and thoughts on continental deformation. We are grateful to Nicolás Castro-Perdomo for his guidance on GNSS data sources and combination techniques. We thank Susanna Ebmeier, Scott Watson, Muhammet Nergizci, Richard Rigby, Yu Morishita, Chen Yu, Andrew Watson, Jack McGrath, Hua Wang, Jonathan Weiss, Pablo Gonzalez, Karsten Spaans, Richard Walters, Emma Hatton and previous LiCS staff, for their various contributions to this project over the many years of its development.

Appendix A. Supplementary data

Supplementary data to this article can be found online at doi:10.1016/j.rse.2026.115320.

Data availability

We thank the European Space Agency (ESA) for the open data policy on the Sentinel-1 mission. The InSAR data are copyrighted by ESA and are provided through the Copernicus Open Access Hub (https://scihub.copernicus.eu/). The Sentinel-1 InSAR data are also freely distributed by the Alaska Satellite Facility (https://asf.alaska.edu/). The GNSS compilation of 2D and 3D data in Eurasia and ITRF14 reference frames for this study are available here: https://github.com/earjcr1/AHB_GPS. The software *VELMAP* for referencing together InSAR line of sight data with GNSS is archived in Wang and Wright (2025) and continually maintained at https://github.com/eejf-leeds/velmap. The InSAR data were processed using LiCSAR System; time series inversion was performed using modified LiCSBAS, release version 1.17 archived in Lazecky et al.

(2025) (from https://github.com/comet-licsar/LiCSBAS). The data files generated here are available in a zenodo data repository for download at doi:10.5281/zenodo.17966454. The full time series of InSAR data are available from the CEDA Archive (https://catalogue.ceda.ac.uk/uuid/5c8a8297aed24118b23440f6742b860e/).

References

Abdrakhmatov, K., Arrowsmith, R., Elliott, J., Grutzner, C., Mukambayev, A., Rizza, M., Shnizai, Z., Walker, R., Weldon, R., Wilkinson, R., 2024. Urgent need for greater earthquake resilience in continental Asia. Nat. Geosci. 17, 818–819. https://doi.org/10.1038/s41561-024-01531-0

Abdrakhmatov, K.Y., Aldazhanov, S.A., Hager, B.H., Hamburger, M.W., Herring, T.A., Kalabaev, K.B., Makarov, V.I., Molnar, P., Panasyuk, S.V., Prilepin, M.T., Reilinger, R.E., Sadybakasov, I.S., Souter, B.J., Trapeznikov, Y.A., Tsurkov, V.Y., Zubovich, A.V., 1996. Relatively recent construction of the Tien Shan inferred from GPS measurements of present-day crustal deformation rates. Nature 384, 450–453. https://doi.org/10.1038/384450a0

Ader, T., Avouac, J.P., Liu-Zeng, J., Lyon-Caen, H., Bollinger, L., Galetzka, J., Genrich, J., Thomas, M., Chanard, K., Sapkota, S.N., Rajaure, S., Shrestha, P., Ding, L., Flouzat, M., 2012. Convergence rate across the Nepal Himalaya and interseismic coupling on the main Himalayan thrust: implications for seismic hazard. J. Geophys. Res.: Solid Earth 117, https://doi.org/10.1029/2011JB009071

Ahmad, W., Choi, M., Kim, S., Kim, D., 2019. Detection of land subsidence and its relationship with land cover types using ESA Sentinel satellite data: a case study of Quetta Valley, Pakistan. Int. J. Remote Sens. 40, 9572–9603. https://doi.org/10.1080/01431161.2019.1633704

Altamimi, Z., Métivier, L., Rebischung, P., Rouby, H., Collilieux, X., 2017. ITRF2014 plate motion model. Geophys. J. Int. 209, 1906–1912. https://doi.org/10.1093/gji/ggx136

Ansari, H., De Zan, F., Parizzi, A., 2021. Study of systematic bias in measuring surface deformation with SAR interferometry. IEEE Trans. Geosci. Remote Sens. 59, 1285–1301. https://doi.org/10.1109/TGRS.2020.3003421

Ao, Z., Hu, X., Tao, S., Hu, X., Wang, G., Li, M., Wang, F., Hu, L., Liang, X., Xiao, J., Yusup, A., Qi, W., Ran, Q., Fang, J., Chang, J., Zeng, Z., Fu, Y., Xue, B., Wang, P., Zhao, K., Li, L., Li, W., Li, Y., Jiang, M., Yang, Y., Shen, H., Zhao, X., Shi, Y., Wu, B., Yan, Z., Wang, M., Su, Y., Hu, T., Ma, Q., Bai, H., Wang, L., Yang, Z., Feng, Y., Zhang, D., Huang, E., Pan, J., Ye, H., Yang, C., Qin, Y., He, C., Guo, Y., Cheng, K., Ren, Y., Yang, H., Zheng, C., Zhu, J., Wang, S., Ji, C., Zhu, B., Liu, H., Tang, Z., Wang, Z., Zhao, S., Tang, Y., Xing, H., Guo, Q., Liu, Y., Fang, J., 2024. A national-scale assessment of land subsidence in China's major cities. Science 384, 301–306. https://doi.org/10.1126/science.adl4366

Argand, E., 1922. La tectonique de l'Asie. Conférence faite á Bruxelles, le 10 août 1922. In: Congrès géologique international (XIIIe session)- Belgique 1922. pp. 171–372.

Attema, E., Duchossois, G., Kohlhammer, G., 1998. ERS-1/2 SAR land applications: overview and main results. In: IGARSS '98. Sensing and Managing the Environment. 1998 IEEE International Geoscience and Remote Sensing. Symposium Proceedings. (Cat. No.98CH36174), vol. 4. pp. 1796–1798, https://doi.org/10.1109/IGARSS.1998.703655

Avouac, J.P., 2015. From geodetic imaging of seismic and aseismic fault slip to dynamic modeling of the seismic cycle. Annu. Rev. Earth Planet. Sci. 43, 233–271. https://doi.org/10.1146/annurev-earth-060614-105302

Avouac, J.P., Ayoub, F., Wei, S., Ampuero, J.P., Meng, L., Leprince, S., Jolivet, R., Duputel, Z., Helmberger, D., 2014. The 2013, Mw 7.7 Balochistan earthquake, energetic strike-slip reactivation of a thrust fault. Earth Planet. Sci. Lett. 391, 128–134. https://doi.org/10.1016/j.epsl.2014.01.036

Barbot, S., Fialko, Y., Bock, Y., 2009. Postseismic deformation due to the M 6.0 2004 parkfield earthquake: stress-driven creep on a fault with spatially variable rate-and-state friction parameters. J. Geophys. Res.: Solid Earth 114, https://doi.org/10.1029/2008JB005748

Barnhart, W.D., 2017. Fault creep rates of the Chaman fault (Afghanistan and Pakistan) inferred from InSAR. J. Geophys. Res.: Solid Earth 122, 372–386. https://doi.org/10.1002/2016JB013656

Beavan, J., Wallace, L.M., Palmer, N., Denys, P., Ellis, S., Fournier, N., Hreinsdottir, S., Pearson, C., Denham, M., 2016. New Zealand GPS velocity field: 1995–2013. N. Z. J. Geol. Geophys. 59, 5–14. https://doi.org/10.1080/00288306.2015.1112817

Bekaert, D., Arena, N., Bato, M.G., Buzzanga, B., Govorcin, M., Havazli, E., Hogenson, K., Hua, H., Johnston, A., Karim, M., Kennedy, J.H., Lu, Z., Marshak, C.Z., Meyer, F., Owen, S., Sangha, S., Short, G., Wang, J., Zinke, R., 2023. The Aria-S1-Gunw: the ARIA sentinel-1 geocoded unwrapped phase product for open insar science and disaster response. In: IGARSS 2023 - 2023 IEEE International Geoscience and Remote Sensing Symposium, pp. 2850–2853, https://doi.org/10.1109/IGARSS52108.2023.10282671

Bekaert, D.P.S., Walters, R.J., Wright, T.J., Hooper, A.J., Parker, D.J., 2015. Statistical comparison of InSAR tropospheric correction techniques. Remote Sens. Environ. 170, 40–47. https://doi.org/10.1016/j.rse.2015.08.035

Bell, M.A., Elliott, J.R., Parsons, B.E., 2011. Interseismic strain accumulation across the Manyi fault (Tibet) prior to the 1997 M_w 7.6 earthquake. Geophys. Res. Lett. 38, https://doi.org/10.1029/2011GL049762

Bilham, R., 2019. Himalayan earthquakes: a review of historical seismicity and early 21st century slip potential. Geol. Soc. Lond. Spec. Publ. 483, 423–482. https://doi.org/10.1144/SP483.16

Bilham, R., Ozener, H., Mencin, D., Dogru, A., Ergintav, S., Cakir, Z., Aytun, A., Aktug, B., Yilmaz, O., Johnson, W., Mattioli, G., 2016. Surface creep on the north Anatolian fault at Ismetpasa, Turkey, 1944–2016. J. Geophys. Res.: Solid Earth 121, 7409–7431. https://doi.org/10.1002/2016JB013394

Bilitza, D., Altadill, D., Truhlik, V., Shubin, V., Galkin, I., Reinisch, B., Huang, X., 2017. International reference ionosphere 2016: from ionospheric climate to real-time weather predictions. Space Weather 15, 418–429. https://doi.org/10.1002/2016SW001593

Bird, P., 2003. An updated digital model of plate boundaries. Geochem. Geophys. Geosyst. 4, https://doi.org/10.1029/2001GC000252

Bird, P., Jackson, D.D., Kagan, Y.Y., Kreemer, C., Stein, R.S., 2015. GEAR1: a global earthquake activity rate model constructed from geodetic strain rates and smoothed seismicity. Bull. Seismol. Soc. Am. 105, 2538–2554. https://doi.org/10.1785/0120150058

Bird, P., Kreemer, C., Holt, W.E., 2010. A long-term forecast of shallow seismicity based on the global strain rate map. Seismol. Res. Lett. 81, 184–194. https://doi.org/10.1785/gssrl.81.2.184

Blewitt, G., Lavallée, D., 2002. Effect of annual signals on geodetic velocity. J. Geophys. Res.: Solid Earth 107, B72145. https://doi.org/10.1029/2001JB000570

Bonì, R., Meisina, C., Cigna, F., Herrera, G., Notti, D., Bricker, S., McCormack, H., Tomás, R., Béjar-Pizarro, M., Mulas, J., Ezquerro, P., 2017. Exploitation of satellite A-DInSAR time series for detection, characterization and modelling of land subsidence. Geosciences 7, 25. https://doi.org/10.3390/geosciences7020025

Bos, M.S., Fernandes, R.M.S., Williams, S.D.P., Bastos, L., 2008. Fast error analysis of continuous GPS observations. J. Geod. 82, 157–166. https://doi.org/10.1007/s00190-007-0165-x

Bourne, S.J., England, P.C., Parsons, B., 1998. The motion of crustal blocks driven by flow of the lower lithosphere and implications for slip rates of continental strike-slip faults. Nature 391, 655–659. https://doi.org/10.1038/35556

Bürgmann, R., Rosen, P.A., Fielding, E.J., 2000. Synthetic aperture radar interferometry to measure earth's surface topography and its deformation. Annu. Rev. Earth Planet. Sci. 28, 169–209. https://doi.org/10.1146/annurev.earth.28.1.169

Cakir, Z., Akoglu, A.M., Belabbes, S., Ergintav, S., Meghraoui, M., 2005. Creeping along the Ismetpasa section of the north Anatolian fault (Western Turkey): rate and extent from InSAR. Earth Planet. Sci. Lett. 238, 225–234. https://doi.org/10.1016/j.epsl.2005.06.044

Calais, E., Vergnolle, M., San'kov, V., Lukhnev, A., Miroshnitchenko, A., Amarjargal, S., Déverchère, J., 2003. GPS measurements of crustal deformation in the Baikal-Mongolia area (1994–2002): implications for current kinematics of Asia. J. Geophys. Res.: Solid Earth 108, https://doi.org/10.1029/2002JB002373

Castro-Perdomo, N., Viltres, R., Masson, F., Klinger, Y., Liu, S., Dhahry, M., Ulrich, P., Bernard, J.D., Matrau, R., Alothman, A., et al., 2022. Interseismic deformation in the Gulf of Aqaba from GPS measurements. Geophys. J. Int. 228, 477–492. https://doi.org/10.1093/gji/ggab353

Chen, C., Zebker, H., 2002. Phase unwrapping for large SAR interferograms: statistical segmentation and generalized network models. IEEE Trans. Geosci. Remote Sens. 40, 1709–1719. https://doi.org/10.1109/TGRS.2002.802453

Chen, J., Wu, T., Zou, D., Liu, L., Wu, X., Gong, W., Zhu, X., Li, R., Hao, J., Hu, G., Pang, Q., Zhang, J., Yang, S., 2022. Magnitudes and patterns of large-scale permafrost ground deformation revealed by Sentinel-1 InSAR on the central Qinghai-Tibet plateau. Remote Sens. Environ. 268, 112778. https://doi.org/10.1016/j.rse.2021.112778

Chen, M., Tomás, R., Li, Z., Motagh, M., Li, T., Hu, L., Gong, H., Li, X., Yu, J., Gong, X., 2016. Imaging land subsidence induced by groundwater extraction in Beijing (China) using satellite radar interferometry. Remote Sens. 8, 468. https://doi.org/10.3390/rs8060468

Choi, J.H., Klinger, Y., Ferry, M., Ritz, J.F., Kurtz, R., Rizza, M., Bollinger, L., Davaasambuu, B., Tsend-Ayush, N., Demberel, S., 2018. Geologic inheritance and earthquake rupture processes: the 1905 M $\geq$ 8 Tsetserleg-Bulnay strike-slip earthquake sequence, Mongolia. J. Geophys. Res.: Solid Earth 123, 1925–1953. https://doi.org/10.1002/2017JB013962

Costantini, M., Minati, F., Trillo, F., Ferretti, A., Novali, F., Passera, E., Dehls, J., Larsen, Y., Marinkovic, P., Eineder, M., Brcic, R., Siegmund, R., Kotzerke, P., Probeck, M., Kenyeres, A., Proietti, S., Solari, L., Andersen, H.S., 2021. European ground motion service (EGMS). In: 2021 IEEE International Geoscience and Remote Sensing Symposium IGARSS, pp. 3293–3296, https://doi.org/10.1109/IGARSS47720.2021.9553562

Crameri, F., Shephard, G.E., Heron, P.J., 2020. The misuse of colour in science communication. Nat. Commun. 11, 5444. 10.1038/s41467-020-19160-7

Da Lio, C., Tosi, L., 2019. Vulnerability to relative sea-level rise in the Po river delta (Italy). Estuar. Coast. Shelf Sci. 228, 106379. https://doi.org/10.1016/j.ecss.2019.106379

Dalaison, M., Jolivet, R., van Rijsingen, E.M., Michel, S., 2021. The interplay between seismic and aseismic slip along the Chaman fault illuminated by InSAR. J. Geophys. Res.: Solid Earth 126, e2021JB021935. https://doi.org/10.1029/2021JB021935

Daout, S., Dini, B., Haeberli, W., Doin, M.P., Parsons, B., 2020. Ice loss in the Northeastern Tibetan plateau permafrost as seen by 16 yr of ESA SAR missions. Earth Planet. Sci. Lett. 545, 116404. https://doi.org/10.1016/j.epsl.2020.116404

Daout, S., Parsons, B., Walker, R., 2021. Post-earthquake fold growth imaged in the Qaidam basin, China, with interferometric synthetic aperture radar. J. Geophys. Res.: Solid Earth 126, e2020JB021241. https://doi.org/10.1029/2020JB021241

Davidson, M.W.J., Furnell, R., 2021. ROSE-L: Copernicus L-band Sar mission. In: 2021 IEEE International Geoscience and Remote Sensing Symposium IGARSS, pp. 872–873, https://doi.org/10.1109/IGARSS47720.2021.9554018

De Zan, F., Gomba, G., 2018. Vegetation and soil moisture inversion from SAR closure phases: first experiments and results. Remote Sens. Environ. 217, 562–572. https://doi.org/10.1016/j.rse.2018.08.034

De Zan, F., Parizzi, A., Prats-Iraola, P., López-Dekker, P., 2014. A SAR interferometric model for soil moisture. IEEE Trans. Geosci. Remote Sens. 52, 418–425. https://doi.org/10.1109/TGRS.2013.2241069

De Zan, F., Zonno, M., López-Dekker, P., 2015. Phase inconsistencies and multiple scattering in SAR interferometry. IEEE Trans. Geosci. Remote Sens. 53, 6608–6616. https://doi.org/10.1109/TGRS.2015.2444431

Dehls, J.F., Larsen, Y., Marinkovic, P., Lauknes, T.R., Stødle, D., Moldestad, D.A., 2019. INSAR.no: a national insar deformation mapping/monitoring service in Norway – from concept to operations. In: IGARSS 2019 - 2019 IEEE International Geoscience and Remote Sensing Symposium, pp. 5461–5464, https://doi.org/10.1109/IGARSS.2019.8898614

Desnos, Y.L., Buck, C., Guijarro, J., Levrini, G., Suchail, J.L., Torres, R., Laur, H., Closa, J., Rosich, B., 2000. The ENVISAT advanced synthetic aperture radar system. In: IGARSS 2000. IEEE 2000 International Geoscience and Remote Sensing Symposium. Taking the Pulse of the Planet: the Role of Remote Sensing in Managing the Environment. Proceedings (Cat. No.00CH37120), vol. 3. pp. 1171–1173, https://doi.org/10.1109/IGARSS.2000.858057

Di Giacomo, D., Engdahl, E.R., Storchak, D.A., 2018. The ISC-GEM earthquake catalogue (1904–2014): status after the extension project. Earth Syst. Sci. Data 10, 1877–1899. https://doi.org/10.5194/essd-10-1877-2018

DiCaprio, C.J., Simons, M., 2008. Importance of ocean tidal load corrections for differential InSAR. Geophys. Res. Lett. 35, https://doi.org/10.1029/2008GL035806

Doin, M.P., Lodge, F., Guillaso, S., Jolivet, R., Lasserre, C., Ducret, G., Grandin, R., Pathier, E., Pinel, V., 2011. Presentation of the small baselin NSBAS processing chain on a case example: the Etna deformation monitoring from 2003 to 2010 using Envisat data. In: Fringe Symposium, pp. 1–7.

Drouin, V., Sigmundsson, F., 2019. Countrywide observations of plate spreading and glacial isostatic adjustment in Iceland inferred by Sentinel-1 radar interferometry, 2015–2018. Geophys. Res. Lett. 46, 8046–8055. https://doi.org/10.1029/2019GL082629

Dziewonski, A.M., Chou, T.A., Woodhouse, J.H., 1981. Determination of earthquake source parameters from waveform data for studies of global and regional seismicity. J. Geophys. Res.: Solid Earth 86, 2825–2852. https://doi.org/10.1029/JB086iB04p02825

Efron, B., Tibshirani, R., 1986. Bootstrap methods for standard errors, confidence intervals, and other measures of statistical accuracy. Stat. Sci. 1, 54–75. https://doi.org/10.1214/ss/1177013815

Ekström, G., Nettles, M., Dziewoński, A.M., 2012. The global CMT project 2004–2010: centroid-moment tensors for 13,017 earthquakes. Phys. Earth Planet. Inter. 200–201, 1–9. https://doi.org/10.1016/j.pepi.2012.04.002

Elliott, J., Walters, R., Wright, T., 2016. The role of space-based observation in understanding and responding to active tectonics and earthquakes. Nature Commun. 7, 13844. https://doi.org/10.1038/ncomms13844

England, P., Jackson, J., 1989. Active deformation of the continents. Annu. Rev. Earth Planet. Sci. 17, 197–226. https://doi.org/10.1146/annurev.ea.17.050189.001213

England, P., Jackson, J., 2011. Uncharted seismic risk. Nat. Geosci. 4, 348–349. https://doi.org/10.1038/ngeo1168

England, P., Molnar, P., 1997. Active deformation of Asia: from kinematics to dynamics. Science 278, 647–650. https://doi.org/10.1126/science.278.5338.647

Evans, E.L., 2022. A dense block model representing western continental United States deformation for the 2023 update to the national seismic hazard model. Seismol. Res. Lett. 93, 3024–3036. https://doi.org/10.1785/0220220141

Fan, C., Liu, L., Zhao, Z., Mu, C., 2025. Pronounced underestimation of surface deformation due to unwrapping errors over Tibetan plateau permafrost by Sentinel-1 InSAR: identification and correction. J. Geophys. Res.: Earth Surf. 130, e2024JF007854. https://doi.org/10.1029/2024JF007854

Fang, J., Houseman, G.A., Wright, T.J., Evans, L.A., Craig, T.J., Elliott, J.R., Hooper, A., 2024a. The dynamics of the India-Eurasia collision: faulted viscous continuum models constrained by High-Resolution Sentinel-1 InSAR and GNSS velocities. J. Geophys. Res.: Solid Earth 129, e2023JB028571. https://doi.org/10.1029/2023JB028571

Fang, J., Wright, T.J., Johnson, K.M., Ou, Q., Styron, R., Craig, T.J., Elliott, J.R., Hooper, A., Zheng, G., 2024b. Strain partitioning in the southeastern Tibetan plateau from kinematic modeling of high-resolution sentinel-1 InSAR and GNSS. Geophys. Res. Lett. 51, e2024GL111199. https://doi.org/10.1029/2024GL111199

Farr, T.G., Rosen, P.A., Caro, E., Crippen, R., Duren, R., Hensley, S., Kobrick, M., Paller, M., Rodriguez, E., Roth, L., Seal, D., Shaffer, S., Shimada, J., Umland, J., Werner, M., Oskin, M., Burbank, D., Alsdorf, D., 2007. The shuttle radar topography mission. Rev. Geophys. 45, https://doi.org/10.1029/2005RG000183

Fattahi, H., Amelung, F., 2016. InSAR observations of strain accumulation and fault creep along the Chaman fault system, Pakistan and Afghanistan. Geophys. Res. Lett. 43, 8399–8406. https://doi.org/10.1002/2016GL070121

Feigl, K.L., Agnew, D.C., Bock, Y., Dong, D., Donnellan, A., Hager, B.H., Herring, T.A., Jackson, D.D., Jordan, T.H., King, R.W., Larsen, S., Larson, K.M., Murray, M.H., Shen, Z., Webb, F.H., 1993. Space geodetic measurement of crustal deformation in central and southern California, 1984–1992. J. Geophys. Res.: Solid Earth 98, 21677–21712. https://doi.org/10.1029/93JB02405

Feigl, K.L., Thatcher, W., 2006. Geodetic observations of post-seismic transients in the context of the earthquake deformation cycle. C. R. Géosci. 338, 1012–1028. https://doi.org/10.1016/j.crte.2006.06.006

Fernández, J., Peter, H., Fernández, C., Berzosa, J., Fernández, M., Bao, L., Muñoz, M.Á., Lara, S., Terradillos, E., Féménias, P., Nogueira, C., 2024. The copernicus POD service. Adv. Space Res. 74, 2615–2648. https://doi.org/10.1016/j.asr.2024.02.056

Festa, D., Bonano, M., Casagli, N., Confuorto, P., De Luca, C., Del Soldato, M., Lanari, R., Lu, P., Manunta, M., Manzo, M., Onorato, G., Raspini, F., Zinno, I., Casu, F., 2022. Nation-wide mapping and classification of ground deformation phenomena through the spatial clustering of p-SBAS InSAR measurements: Italy case study. ISPRS J. Photogramm. Remote Sens. 189, 1–22. https://doi.org/10.1016/j.isprsjprs.2022.04.022

Field, E.H., Biasi, G.P., Bird, P., Dawson, T.E., Felzer, K.R., Jackson, D.D., Johnson, K.M., Jordan, T.H., Madden, C., Michael, A.J., Milner, K.R., Page, M.T., Parsons, T., Powers, P.M., Shaw, B.E., Thatcher, W.R., Weldon II, R.J., Zeng, Y., 2015. Long-term time-dependent probabilities for the third uniform California earthquake rupture forecast (UCERF3). Bull. Seismol. Soc. Am. 105, 511–543. https://doi.org/10.1785/0120140093

Flesch, L.M., Haines, A.J., Holt, W.E., 2001. Dynamics of the India-Eurasia collision zone. J. Geophys. Res.: Solid Earth 106, 16435–16460. https://doi.org/10.1029/2001JB000208

Fu, Y., Wang, J., Zhang, Y., Yang, H., Li, L., Ren, Z., 2025. Spatiotemporal evolution characteristics of ground deformation in the Beijing plain from 1992 to 2023 derived from a novel multi-sensor InSAR fusion method. Remote Sens. Environ. 319, 114635. https://doi.org/10.1016/j.rse.2025.114635

Funning, G.J., Garcia, A., 2019. A systematic study of earthquake detectability using Sentinel-1 interferometric wide-swath data. Geophys. J. Int. 216, 332–349. https://doi.org/10.1093/gji/ggy426

Gabriel, A.K., Goldstein, R.M., Zebker, H.A., 1989. Mapping small elevation changes over large areas: differential radar interferometry. J. Geophys. Res.: Solid Earth 94, 9183–9191. https://doi.org/10.1029/JB094iB07p09183

Gambolati, G., Teatini, P., 2015. Geomechanics of subsurface water withdrawal and injection: groundwater geomechanics. Water Resour. Res. 51, 3922–3955. https://doi.org/10.1002/2014WR016841

Geary, R.C., 1935. The ratio of the mean deviation to the standard deviation as a test of normality. Biometrika 27, 310–332.

Geudtner, D., Torres, R., Snoeij, P., Davidson, M., Rommen, B., 2014. Sentinel-1 system capabilities and applications. In: 2014 IEEE Geoscience and Remote Sensing Symposium, pp. 1457–1460, https://doi.org/10.1109/IGARSS.2014.6946711

Goldstein, R.M., Werner, C.L., 1998. Radar interferogram filtering for geophysical applications. Geophys. Res. Lett. 25, 4035–4038. https://doi.org/10.1029/1998GL900033

Gomba, G., De Zan, F., Brcic, R., Eineder, M., 2024. Mapping worldwide ground deformation in high-strain areas with SAR PS/DS interferometry and sentinel-1 imagery. In: EGU Conference Abstracts, pp. 8645, https://doi.org/10.5194/egusphere-egu24-8645

Goorabi, A., Karimi, M., Yamani, M., Perissin, D., 2020. Land subsidence in isfahan metropolitan and its relationship with geological and geomorphological settings revealed by Sentinel-1A InSAR observations. J. Arid Environ. 181, 104238. https://doi.org/10.1016/j.jaridenv.2020.104238

Grafarend, E., 1984. Variance-covariance components estimation, theoretical results and geodetic applications. In: 16th European Meeting of Statisticians.

Grandin, R., Doin, M.P., Bollinger, L., Pinel-Puysségur, B., Ducret, G., Jolivet, R., Sapkota, S.N., 2012. Long-term growth of the Himalaya inferred from interseismic InSAR measurement. Geology 40, 1059–1062. https://doi.org/10.1130/G33154.1

Gruber, S., 2012. Derivation and analysis of a high-resolution estimate of global permafrost zonation. Cryosphere 6, 221–233. https://doi.org/10.5194/tc-6-221-2012

Guns, K., Sandwell, D., Xu, X., Bock, Y., Yong, L.W., Smith-Konter, B., 2024. Seismic moment accumulation rate from geodesy: constraining Kostrov thickness in southern California. J. Geophys. Res.: Solid Earth 129, e2023JB027939. https://doi.org/10.1029/2023JB027939

Haghshenas Haghighi, M., Motagh, M., 2024. Uncovering the impacts of depleting aquifers: a remote sensing analysis of land subsidence in Iran. Sci. Adv. 10, eadk3039. https://doi.org/10.1126/sciadv.adk3039

Harris, R.A., 2017. Large earthquakes and creeping faults. Rev. Geophys. 55, 169–198. https://doi.org/10.1002/2016RG000539

Hathaway, D.H., 2015. The solar cycle. Living Rev. Sol. Phys. 12, 4. https://doi.org/10.1007/lrsp-2015-4

Hearn, E.H., 2003. What can GPS data tell us about the dynamics of post-seismic deformation? Geophys. J. Int. 155, 753–777. https://doi.org/10.1111/j.1365-246X.2003.02030.x

Herrera-García, G., Ezquerro, P., Tomás, R., Béjar-Pizarro, M., López-Vinielles, J., Rossi, M., Mateos, R.M., Carreón-Freyre, D., Lambert, J., Teatini, P., Cabral-Cano, E., Erkens, G., Galloway, D., Hung, W.C., Kakar, N., Sneed, M., Tosi, L., Wang, H., Ye, S., 2021. Mapping the global threat of land subsidence. Science 371, 34–36. https://doi.org/10.1126/science.abb8549

Herring, T.A., Melbourne, T.I., Murray, M.H., Floyd, M.A., Szeliga, W.M., King, R.W., Phillips, D.A., Puskas, C.M., Santillan, M., Wang, L., 2016. Plate boundary observatory and related networks: GPS data analysis methods and geodetic products. Rev. Geophys. 54, 759–808. https://doi.org/10.1002/2016RG000529

Hetland, E.A., Musé, P., Simons, M., Lin, Y.N., Agram, P.S., DiCaprio, C.J., 2012. Multiscale InSAR time series (MInTS) analysis of surface deformation. J. Geophys. Res.: Solid Earth 117. https://doi.org/10.1029/2011JB008731

Hilley, G.E., Johnson, K., Wang, M., Shen, Z.K., Bürgmann, R., 2009. Earthquake-cycle deformation and fault slip rates in Northern Tibet. Geology 37, 31–34. https://doi.org/10.1130/G25157A.1

Hong, S., Liu, M., Zhou, X., Meng, G., Dong, Y., 2023. Afterslip on conjugate faults of the 2020 Mw 6.3 Nima earthquake in the central Tibetan plateau: evidence from InSAR measurements. Bull. Seismol. Soc. Am. 113, 2026–2040. https://doi.org/10.1785/0120220247

Hooper, A., Segall, P., Zebker, H., 2007. Persistent scatterer interferometric synthetic aperture radar for crustal deformation analysis, with application to volcán Alcedo, Galápagos. J. Geophys. Res.: Solid Earth 112, https://doi.org/10.1029/2006JB004763

Hooper, A., Zebker, H., Segall, P., Kampes, B., 2004. A new method for measuring deformation on volcanoes and other natural terrains using InSAR persistent scatterers. Geophys. Res. Lett. 31. https://doi.org/10.1029/2004GL021737

Houseman, G., England, P., 1986. Finite strain calculations of continental deformation: 1. method and general results for convergent zones. J. Geophys. Res.: Solid Earth 91, 3651–3663. https://doi.org/10.1029/JB091iB03p03651

Hu, J., Li, Z.W., Ding, X.L., Zhu, J.J., Zhang, L., Sun, Q., 2014. Resolving three-dimensional surface displacements from InSAR measurements: a review. Earth-Sci. Rev. 133, 1–17. https://doi.org/10.1016/j.earscirev.2014.02.005

Hu, L., Dai, K., Xing, C., Li, Z., Tomás, R., Clark, B., Shi, X., Chen, M., Zhang, R., Qiu, Q., Lu, Y., 2019. Land subsidence in Beijing and its relationship with geological faults revealed by Sentinel-1 InSAR observations. Int. J. Appl. Earth Obs. Geoinf. 82, 101886. https://doi.org/10.1016/j.jag.2019.05.019

Huang, Z., Zhou, Y., Qiao, X., Zhang, P., Cheng, X., 2022. Kinematics of the 1000 km Haiyuan fault system in northeastern Tibet from high-resolution Sentinel-1 InSAR velocities: fault architecture, slip rates, and partitioning. Earth Planet. Sci. Lett. 583, 117450. https://doi.org/10.1016/j.epsl.2022.117450

Huang, Z., Zhou, Y., Zhang, P., 2023. Newly discovered shallow creep along the gozha Co fault in northwestern Tibet: spatial extent, rate and temporal evolution. Earth Planet. Sci. Lett. 621, 118388. https://doi.org/10.1016/j.epsl.2023.118388

Hussain, E., Hooper, A., Wright, T.J., Walters, R.J., Bekaert, D.P.S., 2016. Interseismic strain accumulation across the central north Anatolian fault from iteratively unwrapped InSAR measurements. J. Geophys. Res.: Solid Earth 121, 9000–9019. https://doi.org/10.1002/2016JB013108

Hussain, E., Wright, T.J., Walters, R.J., Bekaert, D.P.S., Lloyd, R., Hooper, A., 2018. Constant strain accumulation rate between major earthquakes on the north Anatolian fault. Nature Commun. 9, 1392. https://doi.org/10.1038/s41467-018-03739-2

Ingleby, T., Wright, T.J., 2017. Omori-like decay of postseismic velocities following continental earthquakes. Geophys. Res. Lett. 44, 3119–3130. https://doi.org/10.1002/2017GL072865

Jackson, J., McKenzie, D., 1984. Active tectonics of the Alpine—Himalayan belt between western Turkey and Pakistan. Geophys. J. Int. 77, 185–264. https://doi.org/10.1111/j.1365-246X.1984.tb01931.x

Jiang, J., Lohman, R.B., 2021. Coherence-guided InSAR deformation analysis in the presence of ongoing land surface changes in the Imperial Valley, California. Remote Sens. Environ. 253, 112160. https://doi.org/10.1016/j.rse.2020.112160

Johnson, K.M., Wallace, L.M., Maurer, J., Hamling, I., Williams, C., Rollins, C., Gerstenberger, M., Van Dissen, R., 2024. Inverting geodetic strain rates for slip deficit rate in complex deforming zones: an application to the New Zealand plate boundary. J. Geophys. Res.: Solid Earth 129, e2023JB027565. https://doi.org/10.1029/2023JB027565

Jolivet, R., Agram, P.S., Lin, N.Y., Simons, M., Doin, M.P., Peltzer, G., Li, Z., 2014. Improving InSAR geodesy using global atmospheric models. J. Geophys. Res.: Solid Earth 119, 2324–2341. https://doi.org/10.1002/2013JB010588

Jolivet, R., Frank, W.B., 2020. The transient and intermittent nature of slow slip. AGU Advances 1, e2019AV000126. https://doi.org/10.1029/2019AV000126

Jolivet, R., Grandin, R., Lasserre, C., Doin, M.P., Peltzer, G., 2011. Systematic InSAR tropospheric phase delay corrections from global meteorological reanalysis data. Geophys. Res. Lett. 38, https://doi.org/10.1029/2011GL048757

Jolivet, R., Jara, J., Dalaison, M., Rouet-Leduc, B., Özdemir, A., Dogan, U., Çakir, Z., Ergintav, S., Dubernet, P., 2023. Daily to Centennial behavior of aseismic slip along the central section of the north Anatolian fault. J. Geophys. Res.: Solid Earth 128, e2022JB026018. https://doi.org/10.1029/2022JB026018

Jolivet, R., Lasserre, C., Doin, M.P., Peltzer, G., Avouac, J.P., Sun, J., Dailu, R., 2013. Spatio-temporal evolution of aseismic slip along the Haiyuan fault, China: implications for fault frictional properties. Earth Planet. Sci. Lett. 377–378, 23–33. https://doi.org/10.1016/j.epsl.2013.07.020

Kääb, A., Mouginot, J., Prats-Iraola, P., Rignot, E., Rabus, B., Benedikter, A., Rott, H., Nagler, T., Rommen, B., Lopez-Dekker, P., 2024. Potential of the Bi-Static SAR satellite companion mission harmony for land-ice observations. Remote Sens. 16, 2918. https://doi.org/10.3390/rs16162918

Kakar, N., Metzger, S., Schöne, T., Motagh, M., Waizy, H., Nasrat, N.A., Lazecký, M., Amelung, F., Bookhagen, B., 2025. Interferometric radar satellite and in-situ well time-series reveal groundwater extraction rate changes in urban and rural Afghanistan. Water Resour. Res. 61, e2023WR036626. https://doi.org/10.1029/2023WR036626

Kellndorfer, J., Cartus, O., Lavalle, M., Magnard, C., Milillo, P., Oveisgharan, S., Osmanoglu, B., Rosen, P.A., Wegmüller, U., 2022. Global seasonal Sentinel-1 interferometric coherence and backscatter data set. Sci. Data 9, 73. https://doi.org/10.1038/s41597-022-01189-6

Kellogg, K., Hoffman, P., Standley, S., Shaffer, S., Rosen, P., Edelstein, W., Dunn, C., Baker, C., Barela, P., Shen, Y., Guerrero, A.M., Xaypraseuth, P., Sagi, V.R., Sreekantha, C.V., Harinath, N., Kumar, R., Bhan, R., Sarma, C.V.H.S., 2020. NASA-ISRO synthetic aperture radar (NISAR) mission. In: 2020 IEEE Aerospace Conference, pp. 1–21, https://doi.org/10.1109/AERO47225.2020.9172638

Khan, J., Ren, X., Hussain, M.A., Jan, M.Q., 2022. Monitoring land subsidence using PS-InSAR technique in Rawalpindi and Islamabad, Pakistan. Remote Sens. 14, 3722. https://doi.org/10.3390/rs14153722

Khorrami, F., Vernant, P., Masson, F., Nilfouroushan, F., Mousavi, Z., Nankali, H., Saadat, S.A., Walpersdorf, A., Hosseini, S., Tavakoli, P., et al., 2019. An up-to-date crustal deformation map of Iran using integrated campaign-mode and permanent GPS velocities. Geophys. J. Int. 217, 832–843. https://doi.org/10.1093/gji/ggz045

Kreemer, C., Blewitt, G., Klein, E.C., 2014. A geodetic plate motion and global strain rate model. Geochem. Geophys. Geosyst. 15, 3849–3889. https://doi.org/10.1002/2014GC005407

Kreemer, C., Holt, W.E., Haines, A.J., 2003. An integrated global model of present-day plate motions and plate boundary deformation. Geophys. J. Int. 154, 8–34. https://doi.org/10.1046/j.1365-246X.2003.01917.x

Lazecky, M., Fang, J., Hooper, A., Wright, T., 2022. Improved phase unwrapping algorithm based on standard methods. In: IGARSS 2022 - 2022 IEEE International Geoscience and Remote Sensing Symposium, pp. 743–746, https://doi.org/10.1109/IGARSS46834.2022.9884337

Lazecký, M., Hooper, A.J., Piromthong, P., 2023. InSAR-derived horizontal velocities in a global reference frame. Geophys. Res. Lett. 50, e2022GL101173. https://doi.org/10.1029/2022GL101173

Lazecky, M., Morishita, Y., Shen, L., Espín, P., Ou, Q., Hooper, A., McGrath, J., Fang, J., Wang, D., Nergizci, M., Gao, Y., Watson, A., Wright, T., Elliott, J., 2025. LiCSAR Extra & LiCSBAS. Zenodo. https://doi.org/10.5281/zenodo.17734804

Lazecký, M., Ou, Q., Shen, L., McGrath, J., Payne, J., Espín, P., Hooper, A., Wright, T., 2024. Strategies for improving and correcting unwrapped interferograms implemented in LiCSBAS. Proc. Comput. Sci. 239, 2408–2412. https://doi.org/10.1016/j.procs.2024.06.435

Lazecký, M., Spaans, K., González, P.J., Maghsoudi, Y., Morishita, Y., Albino, F., Elliott, J., Greenall, N., Hatton, E., Hooper, A., Juncu, D., McDougall, A., Walters, R.J., Watson, C.S., Weiss, J.R., Wright, T.J., 2020. LiCSAR: an automatic InSAR tool for measuring and monitoring tectonic and volcanic activity. Remote Sens. 12, 2430. https://doi.org/10.3390/rs12152430

Lemrabet, L., Doin, M.P., Lasserre, C., Durand, P., 2023. Referencing of continental-scale InSAR-derived velocity fields: case study of the eastern Tibetan plateau. J. Geophys. Res.: Solid Earth 128, e2022JB026251. https://doi.org/10.1029/2022JB026251

Li, S., Xu, W., Li, Z., 2022. Review of the SBAS InSAR time-series algorithms, applications, and challenges. Geod. Geodyn. 13, 114–126. https://doi.org/10.1016/j.geog.2021.09.007

Li, X., Jónsson, S., Cao, Y., 2021a. Interseismic deformation from Sentinel-1 burst-overlap interferometry: application to the southern Dead Sea fault. Geophys. Res. Lett. 48, e2021GL093481. https://doi.org/10.1029/2021GL093481

Li, Y., Liu, M., Hao, M., Zhu, L., Cui, D., Wang, Q., 2021b. Active crustal deformation in the Tian Shan region, Central Asia. Tectonophysics 811, 228868. https://doi.org/10.1016/j.tecto.2021.228868

Li, Z., Muller, J.P., Cross, P., Fielding, E.J., 2005. Interferometric synthetic aperture radar (InSAR) atmospheric correction: GPS, moderate resolution imaging spectroradiometer (MODIS), and InSAR integration. J. Geophys. Res.: Solid Earth 110. https://doi.org/10.1029/2004JB003446

Liang, C., Agram, P., Simons, M., Fielding, E.J., 2019. Ionospheric correction of InSAR time series analysis of C-band Sentinel-1 TOPS data. IEEE Trans. Geosci. Remote Sens. 57, 6755–6773. https://doi.org/10.1109/TGRS.2019.2908494

Liu, C., Gao, Y., Tian, S., Dong, X., 2018. Rortex—a new vortex vector definition and vorticity tensor and vector decompositions. Phys. Fluids 30, 035103. https://doi.org/10.1063/1.5023001

Liu, M., Stein, S., 2016. Mid-continental earthquakes: spatiotemporal occurrences, causes, and hazards. Earth-Sci. Rev. 162, 364–386. https://doi.org/10.1016/j.earscirev.2016.09.016

Liu, S., Moulin, A., Jónsson, S., 2024. Unloading uplift caused by surface processes in New Zealand's southern Alps. Geophys. Res. Lett. 51, e2024GL109019. https://doi.org/10.1029/2024GL109019

Liu, S., Zhao, L., Wang, L., Liu, L., Zou, D., Hu, G., Sun, Z., Zhang, Y., Chen, W., Wang, X., Wang, M., Zhou, H., Qiao, Y., 2025. Ground surface deformation in permafrost region on the Qinghai-Tibet plateau: a review. Earth-Sci. Rev. 265, 105109. https://doi.org/10.1016/j.earscirev.2025.105109

Lohman, R.B., Bürgi, P.M., 2023. Soil moisture effects on InSAR - a correction approach and example from a hyper-arid region. Remote Sens. Environ. 297, 113766. https://doi.org/10.1016/j.rse.2023.113766

Lohman, R.B., Simons, M., 2005. Some thoughts on the use of InSAR data to constrain models of surface deformation: noise structure and data downsampling. Geochem. Geophys. Geosyst. https://doi.org/10.1029/2004GC000841

Lu, P., Han, J., Yi, Y., Hao, T., Zhou, F., Meng, X., Zhang, Y., Li, R., 2023. MT-InSAR unveils dynamic permafrost disturbances in Hoh Xil (Kekexili) on the Tibetan plateau hinterland. IEEE Trans. Geosci. Remote Sens. 61, 1–16. https://doi.org/10.1109/TGRS.2023.3253937

Lv, X., Amelung, F., Shao, Y., 2022. Widespread aseismic slip along the makran megathrust triggered by the 2013 Mw 7.7 Balochistan earthquake. Geophys. Res. Lett. 49, e2021GL097411. https://doi.org/10.1029/2021GL097411

Lv, X., Shao, Y., 2022. Rheology of the northern Tibetan plateau lithosphere inferred from the post-seismic deformation resulting from the 2001 Mw 7.8 Kokoxili earthquake. Remote Sens. 14, 1207. https://doi.org/10.3390/rs14051207

Maghsoudi, Y., Hooper, A.J., Wright, T.J., Lazecky, M., Ansari, H., 2022. Characterizing and correcting phase biases in short-term, multilooked interferograms. Remote Sens. Environ. 275, 113022. https://doi.org/10.1016/j.rse.2022.113022

McCormack, K., Hesse, M.A., Dixon, T., Malservisi, R., 2020. Modeling the contribution of poroelastic deformation to postseismic geodetic signals. Geophys. Res. Lett. 47, e2020GL086945. https://doi.org/10.1029/2020GL086945

McGrath, J.D., Elliott, J.R., Watson, A.R., Wright, T.J., Piazolo, S., Hamling, I.J., 2025. Linking geodetically resolved uplift to long-term orogenic exhumation in the southern alps, New Zealand. J. Geophys. Res.: Solid Earth 130, e2024JB030625. https://doi.org/10.1029/2024JB030625

McKenzie, D., 1972. Active tectonics of the Mediterranean region. Geophys. J. Int. 30, 109–185. https://doi.org/10.1111/j.1365-246X.1972.tb02351.x

McKenzie, D., 2025. The past and future geography of the eastern Mediterranean constructed from GNSS observations. Earth Planet. Sci. Lett. 658, 119313. https://doi.org/10.1016/j.epsl.2025.119313

Meade, B.J., Klinger, Y., Hetland, E.A., 2013. Inference of multiple earthquake-cycle relaxation timescales from irregular geodetic sampling of interseismic deformation. Bull. Seismol. Soc. Am. 103, 2824–2835. https://doi.org/10.1785/0120130006

Meldebekova, G., Yu, C., Li, Z., Song, C., 2020. Quantifying ground subsidence associated with aquifer overexploitation using space-borne radar interferometry in Kabul, Afghanistan. Remote Sens. 12, 2461. https://doi.org/10.3390/rs12152461

Meyer, F.J., Hogenson, K., Kennedy, J.H., Lewandowski, A.F., Albright, R.W., Short, G., Flores-Anderson, A.I., Rosen, P.A., 2025. Facilitating the golden age of synthetic aperture radar: new tools, services, and training to make synthetic aperture radar data more accessible. IEEE Geosci. Remote Sens. Mag. 2–13. https://doi.org/10.1109/MGRS.2025.3526588

Miranda, N., Meadows, P., Piantanida, R., Recchia, A., Small, D., Schubert, A., Vincent, P., Geudtner, D., Navas-Traver, I., Vega, F.C., 2017. The Sentinel-1 constellation mission performance. In: 2017 IEEE International Geoscience and Remote Sensing Symposium (IGARSS), pp. 5541–5544, https://doi.org/10.1109/IGARSS.2017.8128259

Miranda, N., Torres, R., Geudtner, D., Pinheiro, M., Potin, P., Gratadour, J.B., O'Connell, A., Bibby, D., Navas-Traver, I., Cossu, M., 2023. Sentinel-1 first generation status, past and future. In: IGARSS 2023 - 2023 IEEE International Geoscience and Remote Sensing Symposium, pp. 4560–4563, https://doi.org/10.1109/IGARSS52108.2023.10281990

Mirzadeh, S.M.J., Jin, S., Parizi, E., Chaussard, E., Bürgmann, R., Delgado Blasco, J.M., Amani, M., Bao, H., Mirzadeh, S.H., 2021. Characterization of irreversible land subsidence in the Yazd-Ardakan plain, Iran from 2003 to 2020 InSAR time series. J. Geophys. Res.: Solid Earth 126, e2021JB022258. https://doi.org/10.1029/2021JB022258

Molnar, P., Tapponnier, P., 1975. Cenozoic tectonics of Asia: effects of a continental collision. Science 189, 419–426. https://doi.org/10.1126/science.189.4201.419

Molnar, P., Tapponnier, P., 1978. Active tectonics of Tibet. J. Geophys. Res.: Solid Earth 83, 5361–5375. https://doi.org/10.1029/JB083iB11p05361

Morishita, Y., 2021. Nationwide urban ground deformation monitoring in Japan using Sentinel-1 LiCSAR products and LiCSBAS. Prog. Earth Planet. Sci. 8, 6. https://doi.org/10.1186/s40645-020-00402-7

Morishita, Y., Lazecky, M., Wright, T., Weiss, J., Elliott, J., Hooper, A., 2020. LiCSBAS: an open-source InSAR time series analysis package integrated with the LiCSAR automated Sentinel-1 InSAR processor. Remote Sens. 12, 424. https://doi.org/10.3390/rs12030424

Motagh, M., Walter, T.R., Sharifi, M.A., Fielding, E., Schenk, A., Anderssohn, J., Zschau, J., 2008. Land subsidence in Iran caused by widespread water reservoir overexploitation. Geophys. Res. Lett. 35, https://doi.org/10.1029/2008GL033814

Murray, K.D., Bekaert, D.P.S., Lohman, R.B., 2019. Tropospheric corrections for InSAR: statistical assessments and applications to the central United States and Mexico. Remote Sens. Environ. 232, 111326. https://doi.org/10.1016/j.rse.2019.111326

Nocquet, J.M., Calais, E., 2003. Crustal velocity field of western Europe from permanent GPS array solutions, 1996–2001. Geophys. J. Int. 154, 72–88. https://doi.org/10.1046/j.1365-246X.2003.01935.x

Ou, Q., Daout, S., Weiss, J.R., Shen, L., Lazecký, M., Wright, T.J., Parsons, B.E., 2022. Large-scale interseismic strain mapping of the NE Tibetan plateau from Sentinel-1 interferometry. J. Geophys. Res.: Solid Earth 127, e2022JB024176. https://doi.org/10.1029/2022JB024176

Palano, M., Imprescia, P., Agnon, A., Gresta, S., 2018. An improved evaluation of the seismic/geodetic deformation-rate ratio for the Zagros fold-and-thrust collisional belt. Geophys. J. Int. 213, 194–209. https://doi.org/10.1093/gji/ggx524

Payne, J.A., Watson, A., Maghsoudi, Y., Ebmeier, S., Rigby, R., Lazecký, M., Thomas, M., Elliott, J., 2025. Widespread extent of irrecoverable aquifer depletion revealed by country-wide analysis of land surface subsidence hazard in Iran. J. Geophys. Res.: Solid Earth 130, e2024JB030367. https://doi.org/10.1029/2024JB030367

Peltzer, G., Crampé, F., Hensley, S., Rosen, P., 2001. Transient strain accumulation and fault interaction in the eastern California shear zone. Geology 29, 975–978. https://doi.org/10.1130/0091-7613(2001)029\TU\textless0975:TSAAFI\TU\textgreater2.0.CO;2

Petrolati, D., Gebert, N., Geudtner, D., Bollian, T., Osborne, S., Cesa, M., Simonini, A., Davidson, M., Iannini, L., Cosimo, G.D., 2023. An overview of the copernicus Rose-L SAR instrument. In: IGARSS 2023 - 2023 IEEE International Geoscience and Remote Sensing Symposium, pp. 4310–4313, https://doi.org/10.1109/IGARSS52108.2023.10281670

Piña-Valdés, J., Socquet, A., Beauval, C., Doin, M.P., D'Agostino, N., Shen, Z.K., 2022. 3D GNSS velocity field sheds light on the deformation mechanisms in Europe: effects of the vertical crustal motion on the distribution of seismicity. J. Geophys. Res.: Solid Earth 127, e2021JB023451. https://doi.org/10.1029/2021JB023451

Pinheiro, M., 2024. Increase of Sentinel-1a Orbital Tube: Impact on Interferometry TN - Technical Note. ESA. Esri, Italy.

Pintori, F., Serpelloni, E., Gualandi, A., 2022. Common-mode signals and vertical velocities in the greater Alpine area from GNSS data. Solid Earth 13, 1541–1567. https://doi.org/10.5194/se-13-1541-2022

Potin, P., Rosich, B., Grimont, P., Miranda, N., Shurmer, I., O'Connell, A., Torres, R., Krassenburg, M., 2016. Sentinel-1 mission status. In: Proceedings of EUSAR 2016: 11th European Conference on Synthetic Aperture Radar, pp. 1–6.

Prats, P., Pulella, A., Benedikter, A., Hooper, A., Biggs, J., Kääb, A., Rabus, B., Nagler, T., Rott, H., Pappas, O., et al., 2023. Performance analysis of the harmony mission for land applications: results from the phase a study. In: FRINGE Online Abstracts. pp. 1–4.

Prats-Iraola, P., Rodriguez-Cassola, M., De Zan, F., Scheiber, R., López-Dekker, P., Barat, I., Geudtner, D., 2015. Role of the orbital tube in interferometric spaceborne SAR missions. In: IEEE Geoscience and Remote Sensing Letters, vol. 12. pp. 1486–1490, https://doi.org/10.1109/LGRS.2015.2409885

Qiao, X., Zhou, Y., 2021. Geodetic imaging of shallow creep along the Xianshuihe fault and its frictional properties. Earth Planet. Sci. Lett. 567, 117001. https://doi.org/10.1016/j.epsl.2021.117001

Reid, H.F., 1911. The elastic-rebound theory of earthquakes. Bull. Dep. Geol. Univ. Calif. 6, 413–444.

Reilinger, R., McClusky, S., Vernant, P., Lawrence, S., Ergintav, S., Cakmak, R., Ozener, H., Kadirov, F., Guliev, I., Stepanyan, R., Nadariya, M., Hahubia, G., Mahmoud, S., Sakr, K., ArRajehi, A., Paradissis, D., Al-Aydrus, A., Prilepin, M., Guseva, T., Evren, E., Dmitrotsa, A., Filikov, S.V., Gomez, F., Al-Ghazzi, R., Karam, G., 2006. GPS constraints on continental deformation in the Africa-Arabia-Eurasia continental collision zone and implications for the dynamics of plate interactions. J. Geophys. Res.: Solid Earth. https://doi.org/10.1029/2005JB004051

Reilinger, R.E., McClusky, S.C., Oral, M.B., King, R.W., Toksoz, M.N., Barka, A.A., Kinik, I., Lenk, O., Sanli, I., 1997. Global positioning system measurements of present-day crustal movements in the Arabia-Africa-Eurasia plate collision zone. J. Geophys. Res.: Solid Earth 102, 9983–9999. https://doi.org/10.1029/96JB03736

Rizzoli, P., Martone, M., Gonzalez, C., Wecklich, C., Borla Tridon, D., Bräutigam, B., Bachmann, M., Schulze, D., Fritz, T., Huber, M., Wessel, B., Krieger, G., Zink, M., Moreira, A., 2017. Generation and performance assessment of the global TanDEM-X digital elevation model. ISPRS J. Photogramm. Remote Sens. 132, 119–139. https://doi.org/10.1016/j.isprsjprs.2017.08.008

Roma-Dollase, D., Hernández-Pajares, M., Krankowski, A., Kotulak, K., Ghoddousi-Fard, R., Yuan, Y., Li, Z., Zhang, H., Shi, C., Wang, C., Feltens, J., Vergados, P., Komjathy, A., Schaer, S., García-Rigo, A., Gómez-Cama, J.M., 2018. Consistency of seven different GNSS global ionospheric mapping techniques during one solar cycle. J. Geod. 92, 691–706. https://doi.org/10.1007/s00190-017-1088-9

Rosen, P.A., Gurrola, E., Sacco, G.F., Zebker, H., 2012. The InSAR scientific computing environment. In: EUSAR 2012; 9th European Conference on Synthetic Aperture Radar, pp. 730–733.

Rosen, P.A., Kumar, R., 2021. NASA-ISRO SAR (NISAR) mission status. In: 2021 IEEE Radar Conference (RadarConf21), pp. 1–6, https://doi.org/10.1109/RadarConf2147009.2021.9455211

Rui, X., Stamps, D.S., 2019. A geodetic strain rate and tectonic velocity model for China. Geochem. Geophys. Geosyst. 20, 1280–1297. https://doi.org/10.1029/2018GC007806

Ryder, I., Bürgmann, R., Pollitz, F., 2011. Lower crustal relaxation beneath the Tibetan plateau and Qaidam basin following the 2001 Kokoxili earthquake. Geophys. J. Int. 187, 613–630. https://doi.org/10.1111/j.1365-246X.2011.05179.x

Ryder, I., Parsons, B., Wright, T.J., Funning, G.J., 2007. Post-seismic motion following the 1997 Manyi (Tibet) earthquake: InSAR observations and modelling. Geophys. J. Int. 169, 1009–1027. https://doi.org/10.1111/j.1365-246X.2006.03312.x

Salvi, S., Stramondo, S., Funning, G.J., Ferretti, A., Sarti, F., Mouratidis, A., 2012. The Sentinel-1 mission for the improvement of the scientific understanding and the operational monitoring of the seismic cycle. Remote Sens. Environ. 120, 164–174. https://doi.org/10.1016/j.rse.2011.09.029

Sandwell, D., Mellors, R., Tong, X., Wei, M., Wessel, P., 2011. Open radar interferometry software for mapping surface deformation. Eos Trans. Am. Geophys. Union 92, 234. https://doi.org/10.1029/2011EO280002

Sandwell, D.T., Wessel, P., 2016. Interpolation of 2-D vector data using constraints from elasticity. Geophys. Res. Lett. 43, 10,703–10,709. https://doi.org/10.1002/2016GL070340

Savage, J.C., Gan, W., Svarc, J.L., 2001. Strain accumulation and rotation in the eastern California shear zone. J. Geophys. Res.: Solid Earth 106, 21995–22007. https://doi.org/10.1029/2000JB000127

Savage, J.C., Prescott, W.H., 1978. Asthenosphere readjustment and the earthquake cycle. J. Geophys. Res.: Solid Earth 83, 3369–3376. https://doi.org/10.1029/JB083iB07p03369

Scardino, G., Anzidei, M., Petio, P., Serpelloni, E., De Santis, V., Rizzo, A., Liso, S.I., Zingaro, M., Capolongo, D., Vecchio, A., Refice, A., Scicchitano, G., 2022. The impact of future sea-level rise on low-lying subsiding coasts: a case study of Tavoliere delle Puglie (southern Italy). Remote Sens. 14, 4936. https://doi.org/10.3390/rs14194936

Serpelloni, E., Cavaliere, A., Martelli, L., Pintori, F., Anderlini, L., Borghi, A., Randazzo, D., Bruni, S., Devoti, R., Perfetti, P., et al., 2022. Surface velocities and strain-rates in the Euro-Mediterranean region from massive GPS data processing. Front. Earth Sci. 10, 907897. https://doi.org/10.3389/feart.2022.907897

Serpelloni, E., Faccenna, C., Spada, G., Dong, D., Williams, S.D., 2013. Vertical GPS ground motion rates in the Euro-Mediterranean region: new evidence of velocity gradients at different spatial scales along the Nubia-Eurasia plate boundary. J. Geophys. Res.: Solid Earth 118, 6003–6024. https://doi.org/10.1002/2013JB010102

Shen, L., Hooper, A., Elliott, J.R., Wright, T.J., 2024a. Variability in interseismic strain accumulation rate and style along the Altyn Tagh fault. Nature Commun. 15, 6876. https://doi.org/10.1038/s41467-024-51116-z

Shen, L., Steckler, M., Lindsey, E., Oryan, B., Chong, J.H., 2024b. Large-Scale Geodetic Deformation Measurements of the Indo-Burma Subduction Zone from Multi-Sensor InSAR and GNSS: Implications for Strain Partitioning and Earthquake Hazard Technical Report EGU24-11641. Copernicus Meetings, https://doi.org/10.5194/egusphere-egu24-11641

Sobrero, F.S., Bevis, M., Gómez, D.D., Wang, F., 2020. Logarithmic and exponential transients in GNSS trajectory models as indicators of dominant processes in postseismic deformation. J. Geod. 94, 84. https://doi.org/10.1007/s00190-020-01413-4

Socquet, A., Janex, G., 2019. GNSS position and velocity solutions calculated in the framework of the EPOS initiative with GAMIT-GLOBK. CNRS, OSUG, ISTERRE. https://doi.org/10.17178/GNSS.products.EPOS.2019

Stamps, D.S., Kreemer, C., 2024. Open access GNSS data for studies of the lithosphere. Geochem. Geophys. Geosyst. 25, e2024GC011567. https://doi.org/10.1029/2024GC011567

Steffen, R., Steffen, H., Kenyeres, A., Nilsson, T., Lidberg, M., 2025. EuVeM2022—a European three-dimensional GNSS velocity model based on least-squares collocation. Geophys. J. Int. 241, 437–453. https://doi.org/10.1093/gji/ggaf052

Stephenson, O.L., Liu, Y.K., Yunjun, Z., Simons, M., Rosen, P., Xu, X., 2022. The impact of plate motions on long-wavelength InSAR-derived velocity fields. Geophys. Res. Lett. 49, e2022GL099835. https://doi.org/10.1029/2022GL099835

Stevens, V.L., Avouac, J.P., 2021. On the relationship between strain rate and seismicity in the India–Asia collision zone: implications for probabilistic seismic hazard. Geophys. J. Int. 226, 220–245. https://doi.org/10.1093/gji/ggab098

Storchak, D.A., Di Giacomo, D., Bondár, I., Engdahl, E.R., Harris, J., Lee, W.H.K., Villaseñor, A., Bormann, P., 2013. Public release of the ISC–GEM global instrumental earthquake catalogue (1900–2009). Seismol. Res. Lett. 84, 810–815. https://doi.org/10.1785/0220130034

Storchak, D.A., Di Giacomo, D., Engdahl, E.R., Harris, J., Bondár, I., Lee, W.H.K., Bormann, P., Villaseñor, A., 2015. The ISC-GEM global instrumental earthquake catalogue (1900–2009): introduction. Phys. Earth Planet. Inter. 239, 48–63. https://doi.org/10.1016/j.pepi.2014.06.009

Styron, R., 2022. Contemporary slip rates of all active faults in the Indo-Asian collision zone. ESS Open Arch. https://doi.org/10.1002/essoar.10512747.1

Styron, R., Pagani, M., 2020. The GEM global active faults database. Earthq. Spectra. 36, 160–180. https://doi.org/10.1177/8755293020944182

Thatcher, W., 2007. Microplate model for the present-day deformation of Tibet. J. Geophys. Res.: Solid Earth 112, https://doi.org/10.1029/2005JB004244

Thatcher, W., 2009. How the continents deform: the evidence from tectonic geodesy. Annu. Rev. Earth Planet. Sci. 37, 237–262. https://doi.org/10.1146/annurev.earth.031208.100035

Tian, D., Uieda, L., Leong, W.J., Fröhlich, Y., Schlitzer, W., Grund, M., Jones, M., Toney, L., Yao, J., Tong, J.H., Magen, Y., Materna, K., Belem, A., Newton, T., Anant, A., Ziebarth, M., Quinn, J., Wessel, P., 2025. PyGMT: a Python interface for the generic mapping tools. Zenodo. https://doi.org/10.5281/zenodo.14868324

Tong, X., Sandwell, D.T., Smith-Konter, B., 2013. High-resolution interseismic velocity data along the San Andreas Fault from GPS and InSAR. J. Geophys. Res.: Solid Earth 118, 369–389. https://doi.org/10.1029/2012JB009442

Torres, R., Geudtner, D., Davidson, M., Bibby, D., Navas-Traver, I., Garcia Hernandez, A.I., Laduree, G., Poupaert, J., Bollian, T., Graham, S., 2024. Sentinel-1 Next Generation: Enhanced C-Band Data Continuity, In: EUSAR 2024; 15th European Conference on Synthetic Aperture Radar, pp. 1–4.

Torres, R., Navas-Traver, I., Bibby, D., Lokas, S., Snoeij, P., Rommen, B., Osborne, S., Ceba-Vega, F., Potin, P., Geudtner, D., 2017. Sentinel-1 SAR system and mission. In: 2017 IEEE Radar Conference (RadarConf), pp. 1582–1585, https://doi.org/10.1109/RADAR.2017.7944460

Torres, R., Snoeij, P., Geudtner, D., Bibby, D., Davidson, M., Attema, E., Potin, P., Rommen, B., Floury, N., Brown, M., Traver, I.N., Deghaye, P., Duesmann, B., Rosich, B., Miranda, N., Bruno, C., L'Abbate, M., Croci, R., Pietropaolo, A., Huchler, M., Rostan, F., 2012. GMES sentinel-1 mission. Remote Sens. Environ. 120, 9–24. https://doi.org/10.1016/j.rse.2011.05.028

Üstün, A., Tuşat, E., YalvaÇ, S., Özkan, İ., Eren, Y., Özdemir, A., Bildirici, İ.Ö., Üstüntaş, T., Kırtıloğlu, O.S., Mesutoğlu, M., Doğanalp, S., Canaslan, F., Abbak, R.A., Avşar, N.B., Şimşek, F.F., 2015. Land subsidence in Konya closed basin and its spatio-temporal detection by GPS and DInSAR. Environ. Earth Sci. 73, 6691–6703. https://doi.org/10.1007/s12665-014-3890-5

Vauchez, A., Tommasi, A., Mainprice, D., 2012. Faults (shear zones) in the earth's mantle. Tectonophysics 558–559, 1–27. https://doi.org/10.1016/j.tecto.2012.06.006

Vergnolle, M., Calais, E., Dong, L., 2007. Dynamics of continental deformation in Asia. J. Geophys. Res.: Solid Earth 112, https://doi.org/10.1029/2006JB004807

Wang, D., Elliott, J.R., Zheng, G., Wright, T.J., Watson, A.R., McGrath, J.D., 2024. Deciphering interseismic strain accumulation and its termination on the central-eastern Altyn tagh fault from high-resolution velocity fields. Earth Planet. Sci. Lett. 644, 118919. https://doi.org/10.1016/j.epsl.2024.118919

Wang, H., Wright, T.J., 2012. Satellite geodetic imaging reveals internal deformation of western Tibet. Geophys. Res. Lett. 39, https://doi.org/10.1029/2012GL051222

Wang, H., Wright, T.J., 2025. velmap (v1.1). Zenodo. https://doi.org/10.5281/zenodo.17713962

Wang, K., Zhu, Y., Nissen, E., Shen, Z.K., 2021. On the relevance of geodetic deformation rates to earthquake potential. Geophys. Res. Lett. 48, e2021GL093231. https://doi.org/10.1029/2021GL093231

Wang, L., Barbot, S., 2023. Three-dimensional kinematics of the India–Eurasia collision. Commun. Earth Environ. 4, 1–12. https://doi.org/10.1038/s43247-023-00815-4

Wang, L., Zhao, L., Zhou, H., Liu, S., Du, E., Zou, D., Liu, G., Xiao, Y., Hu, G., Wang, C., Sun, Z., Li, Z., Qiao, Y., Wu, T., Li, C., Li, X., 2022a. Contribution of ground ice melting to the expansion of Selin Co (lake) on the Tibetan plateau. Cryosphere 16, 2745–2767. https://doi.org/10.5194/tc-16-2745-2022

Wang, L.W., Garthwaite, M., Du, Z., Deane, A., McCubbine, J., Wheeler, M., O'Hehir, A., Davies, B., 2022b. InSAR analysis ready data. In: IGARSS 2022 - 2022 IEEE International Geoscience and Remote Sensing Symposium, pp. 2920–2923, https://doi.org/10.1109/IGARSS46834.2022.9884464

Wang, M., Shen, Z.K., 2020. Present-day crustal deformation of continental China derived from GPS and its tectonic implications. J. Geophys. Res.: Solid Earth 125, e2019JB018774. https://doi.org/10.1029/2019JB018774

Wang, Q., Zhang, P.Z., Freymueller, J.T., Bilham, R., Larson, K.M., Lai, X., You, X., Niu, Z., Wu, J., Li, Y., Liu, J., Yang, Z., Chen, Q., 2001. Present-day crustal deformation in China constrained by global positioning system measurements. Science 294, 574–577. https://doi.org/10.1126/science.1063647

Wang, W., Zhao, B., Wang, Q., Yang, S., 2012. Noise analysis of continuous GPS coordinate time series for CMONOC. Adv. Space Res. 49, 943–956.

Wang, Y., Feng, G., Li, Z., Xu, W., Wang, H., Hu, J., Liu, S., He, L., 2022c. Estimating the long-term deformation and permanent loss of aquifer in the southern Junggar basin, China, using InSAR. J. Hydrol. 614, 128604. https://doi.org/10.1016/j.jhydrol.2022.128604

Ward, S.N., 1998. On the consistency of earthquake moment rates, geological fault data, and space geodetic strain: the United States. Geophys. J. Int. 134, 172–186. https://doi.org/10.1046/j.1365-246x.1998.00556.x

Wasmeier, P., 2025. Geodetic transformations (matlab central file exchange). https://mathworks.com/matlabcentral/fileexchange/9696-geodetic-transformations. (Accessed: 12 12 2025).

Watson, A.R., Elliott, J.R., Lazecký, M., Maghsoudi, Y., McGrath, J.D., Walters, R.J., 2024. An InSAR-GNSS velocity field for Iran. Geophys. Res. Lett. 51, e2024GL108440. https://doi.org/10.1029/2024GL108440

Weiss, J.R., Qiu, Q., Barbot, S., Wright, T.J., Foster, J.H., Saunders, A., Brooks, B.A., Bevis, M., Kendrick, E., Ericksen, T.L., Avery, J., SmalleyJr, R., Cimbaro, S.R., Lenzano, L.E., Barón, J., Báez, J.C., Echalar, A., 2019. Illuminating subduction zone rheological properties in the wake of a giant earthquake. Sci. Adv. https://doi.org/10.1126/sciadv.aax6720

Weiss, J.R., Walters, R.J., Morishita, Y., Wright, T.J., Lazecky, M., Wang, H., Hussain, E., Hooper, A.J., Elliott, J.R., Rollins, C., Yu, C., González, P.J., Spaans, K., Li, Z., Parsons, B., 2020. High-resolution surface velocities and strain for Anatolia from Sentinel-1 InSAR and GNSS data. Geophys. Res. Lett. 47, e2020GL087376. https://doi.org/10.1029/2020GL087376

Wen, Y., Li, Z., Xu, C., Ryder, I., Bürgmann, R., 2012. Postseismic motion after the 2001 MW 7.8 Kokoxili earthquake in Tibet observed by InSAR time series. J. Geophys. Res.: Solid Earth 117. https://doi.org/10.1029/2011JB009043

Wessel, P., Luis, J.F., Uieda, L., Scharroo, R., Wobbe, F., Smith, W.H.F., Tian, D., 2019. The generic mapping tools version 6. Geochem. Geophys. Geosyst. 20, 5556–5564. https://doi.org/10.1029/2019GC008515

Williams, S.D., Bock, Y., Fang, P., Jamason, P., Nikolaidis, R.M., Prawirodirdjo, L., Miller, M., Johnson, D.J., 2004. Error analysis of continuous GPS position time series. J. Geophys. Res.: Solid Earth 109. https://doi.org/10.1029/2003JB002741

Williams, S.D.P., 2003. The effect of coloured noise on the uncertainties of rates estimated from geodetic time series. J. Geod. 76, 483–494. https://doi.org/10.1007/s00190-002-0283-4

Wright, T., Parsons, B., Fielding, E., 2001. Measurement of interseismic strain accumulation across the north Anatolian fault by satellite radar interferometry. Geophys. Res. Lett. 28, 2117–2120. https://doi.org/10.1029/2000GL012850

Wright, T.J., 2002. Remote monitoring of the earthquake cycle using satellite radar interferometry. Philos. Trans. R. Soc. Lond. Ser. A Math. Phys. Eng. Sci. 360, 2873–2888. https://doi.org/10.1098/rsta.2002.1094

Wright, T.J., 2016. The earthquake deformation cycle. Astron. Geophys. 57, .4.20–.4.26. https://doi.org/10.1093/astrogeo/atw148

Wright, T.J., Elliott, J.R., Wang, H., Ryder, I., 2013. Earthquake cycle deformation and the Moho: implications for the rheology of continental lithosphere. Tectonophysics 609, 504–523. https://doi.org/10.1016/j.tecto.2013.07.029

Wright, T.J., Houseman, G.A., Fang, J., Maghsoudi, Y., Hooper, A.J., Elliott, J.R., Lazecký, M., Ou, Q., Parsons, B.E., Rollins, C., Shen, L., Wang, H., Wang, D., 2026. High-Resolution Geodetic Velocities Reveal Role of Weak Faults in Deformation of Tibetan Plateau. Science 391, 499–503. https://doi.org/10.1126/science.adi3552

Wright, T.J., Parsons, B., England, P.C., Fielding, E.J., 2004a. InSAR observations of low slip rates on the major faults of western Tibet. Science 305, 236–239. https://doi.org/10.1126/science.1096388

Wright, T.J., Parsons, B.E., Lu, Z., 2004b. Toward mapping surface deformation in three dimensions using InSAR. Geophys. Res. Lett. 31. https://doi.org/10.1029/2003GL018827

Wu, P.C., Wei, M.M., D'Hondt, S., 2022. Subsidence in coastal cities throughout the world observed by InSAR. Geophys. Res. Lett. 49, e2022GL098477. https://doi.org/10.1029/2022GL098477

Wu, Z., Xiao, R., Jiang, M., Ferreira, V.G., 2024. Characterizing the spatial structure and aliasing effect of ocean tide loading on InSAR measurements. Remote Sens. Environ. 311, 114297. https://doi.org/10.1016/j.rse.2024.114297

Xu, X., Sandwell, D.T., 2020. Toward absolute phase change recovery with InSAR: correcting for earth tides and phase unwrapping ambiguities. IEEE Trans. Geosci. Remote Sens. 58, 726–733. https://doi.org/10.1109/TGRS.2019.2940207

Xu, X., Sandwell, D.T., Klein, E., Bock, Y., 2021. Integrated Sentinel-1 InSAR and GNSS time-series along the San Andreas fault system. J. Geophys. Res.: Solid Earth e2021JB022579. https://doi.org/10.1029/2021JB022579

Yagüe-Martínez, N., Prats-Iraola, P., Rodríguez González, F., Brcic, R., Shau, R., Geudtner, D., Eineder, M., Bamler, R., 2016. Interferometric processing of Sentinel-1 TOPS data. IEEE Trans. Geosci. Remote Sens. 54, 2220–2234. https://doi.org/10.1109/TGRS.2015.2497902

Yalvaç, S., Alemdağ, S., Zeybek, H.İ., Yalvaç, M., 2023. Excessive groundwater withdrawal and resultant land subsidence in the Küçük Menderes river basin, Turkey as estimated from InSAR-SBAS and GNSS measurements. Adv. Space Res. 72, 4282–4297. https://doi.org/10.1016/j.asr.2023.08.001

Yamasaki, T., Wright, T.J., Houseman, G.A., 2014. Weak ductile shear zone beneath a major strike-slip fault: inferences from earthquake cycle model constrained by geodetic observations of the western north Anatolian fault zone. J. Geophys. Res.: Solid Earth 119, 3678–3699. https://doi.org/10.1002/2013JB010347

Yi, X., Wang, L., Ci, H., Wang, R., Yang, H., Yan, Z., 2025. Monitoring of land subsidence and analysis of impact factors in the Tianshan north slope urban agglomeration. Land 14, 202. https://doi.org/10.3390/land14010202

Yin, A., 2010. Cenozoic tectonic evolution of Asia: a preliminary synthesis. Tectonophysics 488, 293–325. https://doi.org/10.1016/j.tecto.2009.06.002

Yu, C., Li, Z., Penna, N.T., 2018a. Interferometric synthetic aperture radar atmospheric correction using a GPS-based iterative tropospheric decomposition model. Remote Sens. Environ. 204, 109–121. https://doi.org/10.1016/j.rse.2017.10.038

Yu, C., Li, Z., Penna, N.T., Crippa, P., 2018b. Generic atmospheric correction model for interferometric synthetic aperture radar observations. J. Geophys. Res.: Solid Earth 123, 9202–9222. https://doi.org/10.1029/2017JB015305

Yun, Y., Zeng, Q., Green, B.W., Zhang, F., 2015. Mitigating atmospheric effects in InSAR measurements through high-resolution data assimilation and numerical simulations with a weather prediction model. Int. J. Remote Sens. 36, 2129–2147. https://doi.org/10.1080/01431161.2015.1034894

Yunjun, Z., Fattahi, H., Pi, X., Rosen, P., Simons, M., Agram, P., Aoki, Y., 2022. Range geolocation accuracy of C-/L-band SAR and its implications for operational stack coregistration. IEEE Trans. Geosci. Remote Sens. 60, 1–19. https://doi.org/10.1109/TGRS.2022.3168509

Zeng, Y., Shen, Z.K., 2016. A fault-based model for crustal deformation, fault slip rates, and off-fault strain rate in California. Bull. Seismol. Soc. Am. 106, 766–784. https://doi.org/10.1785/0120140250

Zhang, G., Xu, Z., Chen, Z., Wang, S., Liu, Y., Gong, X., 2024. Analyzing surface deformation throughout China's territory using multi-temporal InSAR processing of Sentinel-1 radar data. Remote Sens. Environ. 305, 114105. https://doi.org/10.1016/j.rse.2024.114105

Zhao, D., Qu, C., Bürgmann, R., Gong, W., Shan, X., 2021. Relaxation of Tibetan lower crust and afterslip driven by the 2001 Mw7.8 Kokoxili, China, earthquake constrained by a decade of geodetic measurements. J. Geophys. Res.: Solid Earth 126, e2020JB021314. https://doi.org/10.1029/2020JB021314

Zhu, L., Gong, H., Li, X., Wang, R., Chen, B., Dai, Z., Teatini, P., 2015. Land subsidence due to groundwater withdrawal in the northern Beijing plain, China. Eng. Geol. 193, 243–255. https://doi.org/10.1016/j.enggeo.2015.04.020